

UNIVERSIDADE DE SÃO PAULO  
INSTITUTO DE FÍSICA DE SÃO CARLOS

PEDRO ERNESTO SCHIAVINATTI TAVARES

**Excitations in Bose-Einstein condensates:  
collective modes, quantum turbulence and  
matter wave statistics**

São Carlos

2016



**PEDRO ERNESTO SCHIAVINATTI TAVARES**

**Excitations in Bose-Einstein condensates: collective  
modes, quantum turbulence and matter wave  
statistics**

Thesis presented to the Graduate Program in  
Physics at the Instituto de Física de São Carlos,  
Universidade de São Paulo to obtain the degree  
of Doctor of Science.

Concentration area: Basic Physics

Advisor:

Prof. Dr. Vanderlei S. Bagnato

Corrected Version

(Original version available on the Program Unit)

São Carlos

2016

AUTHORIZE THE REPRODUCTION AND DISSEMINATION OF TOTAL OR PARTIAL COPIES OF THIS THESIS, BY CONVENCIONAL OR ELECTRONIC MEDIA FOR STUDY OR RESEARCH PURPOSE, SINCE IT IS REFERENCED.

Cataloguing data reviewed by the Library and Information Service  
of the IFSC, with information provided by the author

Tavares, Pedro Ernesto Schiavinatti  
Excitations in Bose-Einstein condensates:  
collective modes, quantum turbulence and matter wave  
statistics / Pedro Ernesto Schiavinatti Tavares;  
advisor Vanderlei Salvador Bagnato - reviewed  
version -- São Carlos 2016.  
134 p.

Thesis (Doctorate - Graduate Program in Basic  
Physics) -- Instituto de Física de São Carlos,  
Universidade de São Paulo - Brasil , 2016.

1. Bose-Eisntein condensation. 2. Collective  
modes. 3. Quantum turbulence. 4. Matter wave  
statistics. I. Bagnato, Vanderlei Salvador, advisor.  
II. Title.

*With love, to  
my parents (José e Vera),  
my brother (Leonardo),  
and my love (Patrícia).*



# Acknowledgements

The process of writing a thesis and doing a doctorate program are long, arduous and, sometimes, exciting. For certainly, it is not done singlehandedly (actually, from my experience, is impossible without professional or personal help). Therefore, many people were fundamental during these years.

First, I thank God for giving me strength during my Ph.D. work and during all my life. And, I would like to express my deep gratitude to:

My parents (José R. Tavares and Vera Lúcia S. Tavares), my brother (Leonardo S. Tavares) and my sister-in-law (Ana Gabriela A. Lima) . For the deep love that we share, for deposit a lot of confidence, and since being “far”, they always can comfort me and feel them close. Further, of course, being the builders of the whole basis of my formation, where much supported me. I love you a lot!

My fiancée (Patrícia F. Rossi), the woman of my life (forever!). For all moments that we passed together (more than 12 years, now) and I wish will be eternal. Thank you for always motivating me (even in the worst situations). For be many patients and comprehensive (especially, in the all long nights at the lab – but you at home; and, in this stressed thesis writing period when my eyes were only on the computer monitor). And, simply, for love me! P.S.: I love you.

All my family (Schiavinatti and Tavares) members, which are a lot. For all fan in get-together parties, family’s barbecues and for all given care. Particularly, in memoriam of my loved grandparents (Lourdes and Pedro Schiavinatti, Ana and Ernesto Tavares), whom I will never forget and I will miss forever, thank you for being part of my life, make me a better person, and constructed all our beautiful family.

My other family (“the fiancée’s family”, Rossi). For loving me as a son (and the reciprocal is the totally true). For deposit a lot of confidence in me. For tolerate all my jokes. For help me greatly in any moment. For the lovely barbecues/lunches/dinners

together. And, to had Paty, for sure.

My friends (“CARNAPUNKers” and “MARECOS”) and my “school-university” friends (Tássio and Anderson). For the incredible union that makes us real friend. For the genial and enjoyable talks imbibed in the “chá the brack”... *always believe my friends!*

My advisor Vanderlei S. Bagnato. For the pleasurable teachings about physics and life. For giving me the opportunity to enter in the beautiful world of cold atoms. For your generosity and friendship. For your incredible capacity to be in all places at the same time and, even so, have time to discussions. Moreover, for giving me support in all these years.

All actual or past member of the BEC1 team: Amilson and Franklin (“os cara de égua”, rrsrs), André S., Rodrigo Shiozaki, Abasalt, Guilherme, Yuri, Gustavo, Prof. Emanuel and the Rb atoms. For all partnership, comprehensible explications, funny work and jokes. For share the same workbench every day, from where this thesis comes from. And, the extremely important help during the elaboration of this thesis text. Particularly, to Giacomo Roati for his contagious enthusiasm and great happiness in discussing and teaching physics, leaving me fissured with lab’s life. Who wise words I will never forget .

The lab friends: Kilvia (specially to be the first to present the lab for me, given me the welcome in the cold atoms world), Edwin, Emmanuel (“Emma”), Patrícia, Kelli, Rafael, Marcos, Jorge, Freddy, Anne, Stella, Andrés, Jair, Rodrigo (“Chê”), Caio (“Rasgueira”), Prof. Sérgio, Prof. Daniel, Prof. André and Prof. Ricardo. Also the theoretician friends: Monica, André, Rafael, Ednilson and Marios. Whom, in any way, contributes a lot for the lab work be better and funnier.

Our collaborators and friends: Prof. Robin Kaiser and Prof. François Impens.

The external thesis defense committee members: Giacomo Roati, Prof. Mahir S. Hussein, Prof. Francisco E. A. dos Santos, Prof. Rodrigo F. Shiozaki. For all discussion and suggestion about the text and the physics of my thesis.

LIEPO team: João (“Johny”), Carlos, Guilherme (“Morre”), Richard, Rogério (“Roger”), André, Denis (“o pimentinha”), Leandro (“Boni”). For the great dedication; producible talks; electronics explanation and development help; and, without doubts, the

delicious coffee.

My physics classmates and lab neighbors. For all life and physics discussions.

All optics group members. In special, to the secretaries and friends: Benê, Cristiane, Adriane, Patrícia, Wagner and Isabel. For the big affection, for the great attention, dedication and for the wonderful and indispensable work. Not forgetting to thanks the express coffee machine, for the daily fuel.

The colleagues from the post-graduation service: Silvio and Ricardo. Too many thanks for all the excellent work and real commitment with all IFSC Ph.D. students.

The library members, especially my colleague Maria Neusa, for your huge help and incontestable dedication in attending us with many cares.

The printing office members, especially my friend Ítalo, for your capacity to do perfectly your works in a short time and very quickly.

To University of São Paulo (USP) and the São Carlos Institute of Physics (IFSC), for make my professional formation a reality.

To CAPES, FAPESP and CNPq for the financial support for this research project. I would like to mention my respect to these institutions, for its huge efforts in fortifying the scientific development and the research in Brazil.

Finally, I would apologize for those whose name I forgot to mention. The fault is the agitation of the deadline day. I am sure that your participation in my work was very important.



*“The future belongs to those who believe  
in the beauty of their dreams.”*

— **Eleanor Roosevelt (1844 - 1962)**

*“Persistence is the road  
to accomplishment.”*

— **Charles Chaplin (1889 - 1997)**

*“For what does it profit a man  
to gain the whole world  
and forfeit his soul?”*

— **Mark 8:36**



# Abstract

TAVARES, P. E. S. **Excitations in Bose-Einstein condensates: collective modes, quantum turbulence and matter wave statistics**. 2016. 134 p. Thesis (Doctorate in Science) - Instituto de Física de São Carlos, Universidade de São Paulo, São Carlos, 2016.

In this thesis, we present the generation and studies of a  $^{87}\text{Rb}$  Bose-Einstein condensate (BEC) perturbed by an oscillatory excitation. The atoms are trapped in a harmonic magnetic trap where, after an evaporative cooling process, we produce the BEC. In order to study the effect caused by oscillatory excitations, a quadrupole magnetic field time oscillatory is superimposed to the trapping potential. Through this perturbation, collective modes were observed. The dipole mode is excited even for low excitation amplitudes. However, a minimum excitation energy is needed to excite the condensate quadrupole mode. Observing the excited cloud in TOF expansion, we note that for excitation amplitude in which the quadrupole mode is excited, the cloud expands without invert its *aspect ratio*. By looking these clouds, after long time-of-flight, it was possible to see vortices and, sometimes, a turbulent state in the condensed cloud. We calculated the momentum distribution of the perturbed BECs and a power law behavior, like the law to Kolmogorov turbulence, was observed. Furthermore, we show that using the method that we have developed to calculate the momentum distribution, the distribution curve (including the power law exponent) exhibits a dependence on the quadrupole mode oscillation of the cloud. The randomness distribution of peaks and depletions in density distribution image of an expanded turbulent BEC, remind us to the intensity profile of a speckle light beam. The analogy between matter-wave speckle and light speckle is justified by showing the similarities in the spatial propagation (or time expansion) of the waves. In addition, the second order correlation function is evaluated and the same dependence with distance was observed for the both waves. This creates the possibility to understand the properties of quantum matter in a disordered state. The propagation of a three-dimensional speckle field (as the matter-wave speckle described here) creates an opportunity to investigate the speckle phenomenon existing in dimensions higher than 2D (the case of light speckle).

**Keywords:** Bose-Einstein condensation. Collective modes. Quantum turbulence. Matter wave statistics.



# Resumo

TAVARES, P. E. S. **Excitações em condensados de Bose-Einstein: modos coletivos, turbulência quântica e estatística de ondas de matéria.** 2016. 134 p. Tese (Doutorado em ciências) - Instituto de Física de São Carlos, Universidade de São Paulo, São Carlos, 2016.

Nesta tese, descrevemos a produção e os estudos de condensados de Bose-Einstein, em átomos de  $^{87}\text{Rb}$ , perturbados através de excitações oscilatórias. Os átomos aprisionados são aprisionados em uma armadilha magnética harmônica onde produzimos o condensado de Bose-Einstein após o processo de resfriamento evaporativo. Com o objetivo de estudar o efeito de excitações oscilatórias, um campo magnético quadrupolar temporalmente oscilante é superposto ao campo de aprisionamento. Através dessa perturbação, podemos observar a excitação de modos coletivos no condensado. Mesmo para baixas amplitudes de excitação, o modo dipolar é facilmente excitado. Porém, observamos que para excitar o modo quadrupolar no condensado é necessária uma energia mínima. Através da expansão em tempo de voo da nuvem excitada, identificamos que, para amplitude de excitação na qual o modo quadrupolar é excitado, a nuvem expande sem inverter o *aspect ratio*. Analisando essas nuvens por longos tempos de voo, foi possível observar alguns vórtices e, às vezes, um estado turbulento na nuvem condensada. Calculamos a distribuição de momento dessas nuvens e notamos que ela exibe um comportamento de lei de potência, parecido com a lei de Kolmogorov para turbulência. Além disso, mostramos que pelo nosso método que desenvolvemos para calcular a distribuição de momento, a forma da curva dessa distribuição (inclusive o expoente da lei de potência) exibe uma dependência com o modo quadrupolar de oscilação da nuvem. A distribuição desordenada de picos e depleções, na imagem da distribuição de densidade do condensado turbulento expandido, assemelha-se ao perfil de intensidade de um feixe de luz com speckle. A analogia entre speckle de onda de matéria e de luz é fundamentada através das semelhanças entre a propagação (ou expansão) dessas duas ondas. Além disso, a função de correlação de segunda ordem foi calculada e a mesma dependência com a distância foi observada para as duas ondas. Isto cria a possibilidade de entender melhor as propriedades da matéria quântica em um estado de desordem. A propagação de um campo de speckle tridimensional (como é o caso do speckle de onda de matéria aqui descrito) cria uma oportunidade de investigar o fenômeno de speckle em dimensões maiores que 2D (o caso do speckle de luz).

**Palavras-chaves:** Condensação de Bose-Einstein. Modos coletivos. Turbulência quântica. Estatística de ondas de matéria.



# List of Figures

Figure 1 – Illustration of the BEC low-lying collective modes. The condensate is trapped in a harmonic cigar-shaped trap potential and the low-lying modes are: (a) Dipolar mode, (b) Breathing mode and (c) Quadrupolar mode. These figures refers to the fundamental frequencies of each mode.	46
Figure 2 – Diagram of processes in the experimental sequence to produce a Bose-Einstein condensate in our apparatus. Typical final atom numbers and temperatures are presented for each step. This experimental sequence has a duration of about 1 minute.	54
Figure 3 – New vacuum system 3D drawing. The three ion pumps are responsible to pump the MOT1 chamber, the differential pumping stage and the science chamber.	55
Figure 4 – Schematic draw of a magneto-optical trap configuration. The MOT is composed by three pairs of orthogonal counterpropagating laser beams (with circular polarization) and an inhomogeneous magnetic field (typically produced by a pair of coils in anti-Helmholtz configuration)	57
Figure 5 – Pictures of the atoms trapped in the MOTs. (a) Fluorescence of the trapped atoms in MOT1. (b) Fluorescence of the trapped atoms in MOT2.	58
Figure 6 – Quadrupole-Ioffe configuration (QUIC) magnetic trap. (a) Schematic draw of the QUIC trap. (b) Magnetic field magnitude as a function of the $x$ -direction, for the magnetic capture (black solid line) and during the transference from the MT (red dotted line) to the harmonic QUIC trap (purple long-dashed line).	62

Figure 7 – Image processing to obtain the normalized absorption image, $\tilde{I}(x, y)$ . We show the image of the probe beam with atoms, the probe beam image and the background image. We subtract the third image from the other and we divide both results, which originate the normalized image. . . . .	64
Figure 8 – Illustration of the Zeeman level shifts for different magnetic field value inside the QUIC trap. The high energy atoms reach higher magnetic field values, thus the Zeeman level shifts are greater than the less energetic atoms. . . . .	67
Figure 9 – RF-forced evaporative cooling. (a) RF ramp used to produce a BEC, it is composed by 5 linear ramps delimited by the circles. (b) Normalized absorption image of the cloud for different points of the RF ramp, showing the atoms number, the cloud temperature and, after the BEC transition, the condensation atoms fraction ( $N_0/N$ ). . . . .	68
Figure 10 – Absorption image profiles during the BEC transition. The numeric index above each cloud correspond to the marked images from Figure 9(b). . . . .	69
Figure 11 – Schematic drawing of the excitation system in the (a) $xy$ plane and (b) $xz$ plane. . . . .	70
Figure 12 – Schematic drawing of the excitation coils setup used to study the collective modes. (a) $xy$ plane and (b) $xz$ plane. . . . .	74
Figure 13 – Driven oscillations. Center-of-mass position as a function of the excitation time for three excitation frequencies: (a) $f_{\text{exc}} = 170$ Hz, (b) $f_{\text{exc}} = 194$ Hz and (c) $f_{\text{exc}} = 260$ Hz. . . . .	75
Figure 14 – Typical images acquired during the experimental runs. Normalized absorption images of the excited BEC evolving in-trap, after certain hold time (shown on the bottom of each image). The excitation amplitude was about 470 mG/cm and the images were taken after 20 ms time-of-flight. It is noticeable a movement of the cloud center-of-mass and a variation on the condensate shape as the hold time is increased. . . . .	76

Figure 15 – Low-lying collective excitation modes. (a) The center-of-mass and (b) the $AR$ as a function of the hold time, for 4 different excitation amplitudes, corresponding to the dipolar mode and the quadrupolar mode, respectively. . . . .	78
Figure 16 – BEC fraction ( $N_0/N$ ) as a function of hold time for a equilibrium BEC (blue squares) and a perturbed BEC (magenta circles) with excitation amplitude 550 mG/cm. . . . .	79
Figure 17 – Collective modes frequency and amplitude dependency with the excitation amplitude. (a) Dipolar and quadrupolar mode frequencies versus the perturbing amplitude. (b) Condensate CM and $AR$ oscillation amplitude as a function of the excitation amplitude. . . . .	80
Figure 18 – Image sequence of excited cloud for different time-of-flights (shown below of each image). The excitation amplitude and hold time was fixed in 550 mG/cm and 20 ms, respectively. . . . .	81
Figure 19 – Aspect ratio (A.R.) evolution during time-of-flight expansion for different excitation amplitudes. Each panel corresponds to a specific hold time: (a) 32 ms, (b) 33 ms, (c) 34 ms and (d) 35 ms. . . . .	82
Figure 20 – Illustration about the method to compute $G(r')$ . The atomic density distribution, $n(x, y)$ , is pictured by the blue region. The dark area represents the region that will give $G(r')$ for a radius $r'^2 = x'^2 + y'^2$ . . . . .	87
Figure 21 – Eliminating dipolar and scissors mode effect. (a) full absorption image. (b) Image centered in the cloud center-of-mass showing the cloud major axis. (c) Tilded image to match the cloud major axis with the picture vertical axis. . . . .	88
Figure 22 – Projected momentum distribution of non-excited BEC (black squares) and excited BECs (colored symbols) for different hold times. (a) Non-turbulent cloud (315 mG/cm of excitation amplitude). (b) Turbulent cloud (Excitation amplitude equal to 470 mG/cm). . . . .	89

Figure 23 – $k'_{n'(k')=1}$ oscillation as a function of the in-trap time, showing a sinusoidal behavior with frequency matching the BEC quadruple mode frequency. (b) Amplitude of the fitted oscillation as a function of the excitation amplitude, showing a non-linear behavior as observed for the quadrupolar mode. . . . .	91
Figure 24 – Atomic cloud expansion and optical beam propagation. Sequence of three different time-of-flight showing the expansion of a (a) regular BEC and (b) turbulent cloud. Sequence of three different propagation distance showing the expansion of a (d) Gaussian and (d) Speckle beam. The propagation distances $z_1$ , $z_2$ and $z_3$ , are chosen to the Gaussian beam aspect ratio match with the regular BEC one at the three given TOFs in (a). . . . .	96
Figure 25 – Cloud expansion during time-of-flight. Cloud dimensions $R_x$ and $R_y$ along the $x$ and $y$ directions, as a function of the time-of-flight for a (a) regular BEC and (b) turbulent BEC. . . . .	97
Figure 26 – Optical beam waists propagation. Beam sizes $w_x$ and $w_y$ along the $x$ and $y$ directions, as a function of the propagation distance for a (a) coherent Gaussian and (b) speckle beam. In the marked propagation distances $z_1$ , $z_2$ and $z_3$ , the Gaussian beam aspect ratio match with the regular BEC one at the three TOF of Figure 24(a). . . . .	98
Figure 27 – Comparison between turbulent cloud and speckle beam. (a) column integrated density profile for a turbulent BEC and (b) intensity profile for the cross section of a speckle beam. The integration in one of the 3D dimension of the BEC cloud result in slight reducing the amplitude of density variations. . . . .	100
Figure 28 – Second-order correlation function. (a) $g^{(2)}$ for a regular BEC (green circles and green fitted line) and a turbulent cloud (red squares and red fitted line) as a function of distance, $\Delta r$ . (b) $g^{(2)}$ for a Gaussian (green circles and green fitted line) and a speckle beam (red squares and red fitted line) as a function of distance, $\Delta r$ , in units of $\lambda$ . . . . .	101

Figure 29 – TOF expansion of a BEC with a multicharged vortex ( $n = 4$ ) produced by topological phase-imprinting technique. The time-of-flight of each picture are shown in its right-side. . . . .	108
Figure 30 – Illustrative drawing on the density-density correlation function calculation. $A$ and $B$ are two pixels of the cloud optical density (blue), at a position $(i, j)$ and $(i + \Delta i, j + \Delta j)$ , respectively. . . . .	127
Figure 31 – Comparison between a 2D speckle beam and its projection in one dimension. (a) Simulated speckle beam cross-section profile. (b) 1D projection profile of the speckle beam . . . . .	133
Figure 32 – Comparison between $g_{2D}^{(2)}(\Delta r)$ and $g_{1D}^{(2)}(\Delta r)$ . Second-order correlation function for a 2D speckle beam, $g_{2D}^{(2)}(\Delta r)$ (green squares), and for its projection in one dimension, $g_{1D}^{(2)}(\Delta r)$ (blue circles). . . . .	134



# List of abbreviations and acronyms

BEC	Bose-Einstein condensation/condensate.
GPE	Gross-Pitaevskii equation.
TFA	Thomas-Fermi approximation.
CT	Classical turbulence.
QT	Quantum turbulence.
LIAD	Light-induced atom desorption.
MOT	Magneto-optical trap.
MOT1	Magneto-optical trap produced in the first chamber.
MOT2	Magneto-optical trap produced in the science chamber.
MT	Magnetic trap.
QUIC	Quadrupole-Ioffe configuration.
TOF	Time-of-flight.
CCD	Charge-coupled device.
OD	Optical density.
RF	Radio-frequency.
PSD	Phase-space density.
CM	Center of mass.
AR	Aspect ratio.



# List of symbols

$m$	Atomic mass.
$\mu$	Chemical potential.
$g$	Atoms effective interaction.
$a$	Scattering length.
$V(\mathbf{r})$	Trapping potential.
$a_{\text{ho}}$	Harmonic oscillator length.
$\xi$	Healing length.
$n'(k')$	2D-projected momentum distribution.
$g^{(2)}$	Second order correlation function.
$\langle X \rangle$	Mean of $X$ .



# Contents

1	INTRODUCTION . . . . .	29
1.1	The journey to condensate dilute gases . . . . .	31
1.2	Thesis summary . . . . .	32
2	BOSE-EINSTEIN CONDENSATION, COLLECTIVE MODES AND QUANTUM TURBULENCE . . . . .	35
2.1	Ideal Bose gas in an external potential . . . . .	35
2.1.1	Ideal Bose gas in a box trap . . . . .	37
2.1.2	Ideal Bose gas in an anisotropic harmonic trap . . . . .	38
2.2	Weakly interacting Bose gas . . . . .	39
2.2.1	Gross-Pitaevskii equation . . . . .	39
2.2.2	Thomas-Fermi approximation . . . . .	41
2.2.3	Hydrodynamic equations . . . . .	42
2.3	Collective modes of a trapped condensate . . . . .	43
2.4	Turbulence . . . . .	46
2.4.1	Classical fluids . . . . .	47
2.4.2	Quantum fluids . . . . .	49
3	EXPERIMENTAL APPARATUS . . . . .	53
3.1	Experiment overview . . . . .	53
3.2	Vacuum system . . . . .	54
3.3	Double-MOT configuration . . . . .	56
3.4	Transference to a magnetic trap . . . . .	59
3.5	The magnetic QUIC trap . . . . .	61
3.6	Absorption imaging . . . . .	63
3.6.1	Thermal cloud . . . . .	64
3.6.2	Condensate cloud . . . . .	65

3.6.3	Bimodal cloud . . . . .	66
3.7	Evaporative cooling and the BEC . . . . .	67
3.8	Excitation system . . . . .	69
4	EXCITATION OF COLLECTIVE MODES BY AN OSCIL- LATORY PERTURBATION . . . . .	73
4.1	Setting the excitation system . . . . .	73
4.2	Setting the excitation frequency . . . . .	74
4.3	Observation of collective modes . . . . .	75
4.4	Results and discussions . . . . .	77
5	MOMENTUM DISTRIBUTION OF A PERTURBED BEC .	85
5.1	Introduction . . . . .	85
5.2	Methodology to compute the momentum distribution from an expanded cloud . . . . .	86
5.3	Momentum distribution coupled to the quadrupolar mode . .	88
6	QUANTUM TURBULENCE AND STATISTICAL ATOM OPTICS . . . . .	93
6.1	Motivation . . . . .	93
6.2	Equivalences between matter and optics waves . . . . .	95
6.3	Second-order correlation function . . . . .	99
7	CONCLUSIONS AND PROSPECTS . . . . .	103
7.1	Conclusions . . . . .	103
7.2	A glimpse into the future . . . . .	107
7.3	Prospects . . . . .	109
	REFERENCES . . . . .	111

**APPENDIX**

**125**

**APPENDIX A – Calculating  $g^{(2)}(\Delta r)$  . . . . . 127**

**APPENDIX B – Effects of a projection onto correlation length . . . . . 133**



# 1 Introduction

The Bose-Einstein condensation (BEC) was predicted in 1925, by Albert Einstein (1) using the method introduced, in 1924, by Satyendra Nath Bose (2) to obtain the black-body spectrum. When a gas of noninteracting atoms is cooled below a critical temperature, the particles condensate in the single particle state, the ground energy state. The large occupation of the ground state makes the condensate to reveal quantum properties macroscopically. That has made the BEC an excellent model system for exploring different areas of physics: thermodynamics (3,4), statistical mechanics (5), quantum mechanics (6,7), quantum field theory (8,9), condensed matter physics (10,11), many-body physics (12), and beyond.

The superfluidity observed in liquid helium (13,14) was also related to the manifestation of BEC (15). In 1941, (16) Landau developed the first theory of superfluidity, studying its elementary excitations. An important improvement in this field happened with the predictions of quantized vortices and turbulence in superfluids (17,18) and with its experimental observation. (19)

Experimental studies on BEC of atomic gases were developed much later. By thinking in the BEC principle, it may seem to be simple to reach the condensation in atomic gases: just need to cool the gas until the atoms are in the lowest energy state and the atomic wave packets overlap. However, following this simple rule, in most cases the familiar transitions to a liquid or solid state will occur and the quantum degeneracy will never be achieved in the gas phase. It is necessary to have a dilute gas\* to avoid the conventional condensation into a liquid or solid. Under this condition, the thermal equilibrium of the gas translational degree of freedom is reached much faster than the chemical equilibrium. Thus, dilute gases can exhibit quantum degeneracy. However, these low densities ( $\sim 10^{14}$  atoms/cm<sup>-3</sup>) implies in an ultra-low critical temperature, around a

---

\* a gas with atomic density,  $n$ , where the atomic s-wave scattering length,  $a$ , is smaller than the mean inter-particle distance, proportional to  $n^{-1/3}$ . Thus, the diluteness condition is  $na^3 \ll 1$

few hundreds of nanokelvin.

Those values made the search to BEC in dilute gases a long journey with great scientific advances, where we can highlight the development of atom cooling and trapping techniques with light or magnetic field (20–22) and the evaporative cooling (23) technique. In 1995, three groups produced experimentally Bose-Einstein condensates in:  $^{87}\text{Rb}$  (24) sample by the group of Eric A. Cornell and Carl Wieman,  $^{23}\text{Na}$  (25) by Wolfgang Ketterle's group, and  $^7\text{Li}$  (26) by Randall G. Hulet's group.

While the early works in atomic BECs were focused on the thermodynamics around the phase transition, the dynamics of a trapped BEC induced by external perturbation became one of the major research topics in condensates. We can highlight the studies (27–29) about the superfluid characteristics of a BEC, (30–32) about the quantized vortices and (33–36) about the quantum turbulence.

The experimental research on BECs in our group started in 2004 with Kilvia M. Farias thesis (37), where sodium atoms was cooled until the quantum degeneracy. Because of experimental limitations of that system, they started another experiment with a different atomic species, the isotope 87 of rubidium atoms. This experimental system, that we called *BEC-I*, had its first version built during the Ph.D of Emanuel A. L. Henn (38).

In a first series of studies, in which a condensate was perturbed by an oscillatory magnetic field, it was possible to observe (29) a counterflow oscillation between the BEC and the thermal cloud, (31) the vortex nucleation and (33) the first evidence of quantum turbulence in BEC of dilute gases. However, the experimental system had many technical problems and those studies left some questions concerning the generation mechanism of this interesting phenomenon. Motivated by these questions, we decided to rebuild the *BEC-I* experiment (this was the initial mark of my Ph.D.). In 2012, March 23rd, we finished to set the vacuum system and approximately one year later (in March 26th, 2013) we achieved again the Bose-Einstein condensation in  $^{87}\text{Rb}$  atoms.

In the next section, we present an overview of the journey of technical development

that happened for the world first experimental production of BEC in dilute gases.

## 1.1 The journey to condensate dilute gases

The Maxwell's theory of eletromagnetism provides a qualitative understanding that eletromagnetic radiation exerts a force in matter. At the beginning of the 19th century, Pyotr N. Lebedev (39) and Ernest F. Nichols together with Gordon F. Hull (40,41), provided qualitative measurements of radiation pressure on macroscopic objects. In 1933, deflecting an atomic sodium beam with resonant radiation from a lamp, (42) Robert Frisch made the first demonstration of the light pressure on atoms.

A remarkable improvement in science and technology happened in 1960, when Theodore H. Maiman (43) created the first working lasers. Arthur Ashkin (44) recognized, in 1970, the potential of the intense, narrow-band light to manipulate atoms. The measurement of atomic spectral lines with tunable sources of laser light (45) allowed, in 1972, two groups (46,47) to first demonstrate the deflection of atomic beams with lasers.

The laser cooling technique (the reduction of thermal velocities using radiation pressure) was proposed in 1975, independently, by (48) Theodor Hänsch's group and (49) David Wineland's group. Seven years later, William D. Phillips and Harold Metcalf (50) reported the first demonstration of laser cooling. An atomic laser beam of sodium atoms passing through a Zeeman slower was decelerated by two counter-propagating laser beams. In 1985, this group (51) also was the first to magnetically trap those cold sodium atoms. Moreover, in the same year, the group of Steven Chu demonstrated the optical molasses: a 3D cooling of sodium atoms with three orthogonal pairs of counter-propagating laser beams. Three years latter, David E. Pritchard's group improved the optical molasses by adding a quadrupole magnetic field centered with the laser beams crossing regions (52), which allowed them to cool and trap larger samples in a magneto-optical trap.

In 1988, the group of Daniel Kleppner performed the first evaporative cooling

(53) in spin-polarized hydrogen atoms. Finally, in 1995, by applying evaporative cooling technique, the Bose-Einstein condensation was first observed in sample of  ${}^7\text{Li}$ ,  ${}^{87}\text{Rb}$  and  ${}^{23}\text{Na}$  (24–26), independently.

Such experimental observation opened up a large range of possibilities for the condensation. The research community dedicated efforts to achieve this transition in many different atomic species, bosonic or fermionic. In fact, the list of isotopes, of which quantum degenerate gases were obtained, is quite long and keep growing. BEC was also observed for quantum degenerate Fermi gases (54), for photons in an optical cavity (55). Molecular BECs composed of bound fermionic atoms were produced (56). It is important to note that, even the first recipe for reach BEC was the one described above, each new experimental system can have its own way to produce a BEC, such is the robustness of this phenomenon. Also it is possible to have different types of traps: Magnetic traps, Optical traps, Hybrid (Magnetic and optical) traps. The greatest feature in this type of experiments concern the high level of control. For example, by increasing the confinement in one of the three-dimensions, it is possible to generate traps with 2D or 1D dimension.

## 1.2 Thesis summary

In this section we will present the thesis outline. Basically, in this thesis we describe three studies in an excited BEC: the first concerns the collective modes, the second is about the momentum distribution of the cloud, and the last one is the observation of a matter-wave speckle in turbulent atomic superfluids.

This thesis is organized as follows: In Chapter 2 we will briefly review the main theoretical concepts to support the presented results. The ideal gas confined in an external potential will be presented in Section 2.1. The interaction between the particles of the system will be taken into account and a more realistic case of BEC will be treated in Section 2.2. We end this chapter by providing a theoretical overview of specific topics

related to the experimental results, in Sections 2.3 and 2.4.

In Chapter 3 we present the experimental setup used to produce the BEC samples. A brief overview of the main experimental processes is shown in Section 3.1 and in the following sections of this chapter we will describe individually each one: vacuum system, double-MOT configuration, mode-matching processes, magnetic QUIC trap, evaporative cooling, absorption image, and the excitation system.

We observed low-lying collective modes by perturbing the BEC with an external temporal magnetic oscillation, this will be described in Chapter 4. We start, in Section 4.1, by showing the procedure used to set the excitation system. The excitation sequence and parameters are presented in Section 4.3, which also shows the observed modes. We conclude this chapter, in Section 4.4, by providing the quantitative analysis of these modes and revealing the non-linear behavior to excite efficiently the quadrupole mode. A final remark is that the condensate, perturbed with a large quadrupolar mode, exists in a turbulent regime.

Motivated by the observation of a turbulent regime, in Chapter 5 we studied the momentum distribution of a perturbed BEC as a function of the excitation parameters. In Sections 5.1 and 5.2 we provide the motivation to study the momentum distribution and the methodology to compute the momentum distribution from an expanded cloud. The results of this analysis are shown in Section 5.3. A coupling between the momentum distribution curves and the quadrupolar collective mode was observed. This effect might have a more prosaic explanation for the apparent discrepancy from the Kolmogorov's power law observed (57) in a previous work.

In Chapter 6, we analyze the properties of quantum turbulence by taking into account its wave nature. Section 6.1 presents the motivation of this analysis. The randomness of amplitude and phase introduced in the turbulent cloud allows an analogy of the free expanding turbulent cloud (disordered matter wave) with the propagation of a speckle light field (disordered optical wave). In order to establish this equivalences, in Section 6.2 we compare the propagation divergence for both waves. In Section 6.3 we compute the second-order correlation and supply the analogy between a turbulent atomic

cloud in expansion and the propagation of a speckle field.

The conclusions are summarized in Chapter 7, and we also discuss some experimental prospects for subsequent studies in the *BEC-I* system.

## 2 Bose-Einstein condensation, collective modes and quantum turbulence

In this chapter we present a theoretical overview about the Bose-Einstein condensation and some concepts that are important to understand the results presented in this thesis. In section 2.1 we discuss the non-interacting Bose gas confined in an external potential, which we are based on the (3,5) standard textbooks and (58,59) references. A more realistic case will be treated in section 2.2, following the references (60,61), where the interaction between the particles of the system will be taken into account. Finally, in the last two sections we will give a theoretical overview about the topics related to the experimental results presented in this thesis.

### 2.1 Ideal Bose gas in an external potential

We consider a gas of  $N$  non-interacting bosons with mass  $m$ , confined in an external potential  $V(\mathbf{r})$ . The particle distribution,  $n_\varepsilon$ , in the potential energy levels,  $\varepsilon$ , is given by the Bose-Einstein distribution,

$$n_\varepsilon = \frac{1}{\exp\left(\frac{\varepsilon - \mu}{k_B T}\right) - 1} \quad , \quad (2.1)$$

where  $\mu$  is the chemical potential,  $k_B$  is the Boltzmann constant and  $T$  is the temperature of the gas.

The total number of atoms in the gas is given by summing the distribution, Equation (2.1), over all states,

$$N = \sum_{\varepsilon} n_\varepsilon \quad . \quad (2.2)$$

In the thermodynamic limit, the potential energy level spacing is much smaller than the typical energy of the system,  $\varepsilon_{i+1} - \varepsilon_i \ll k_B T$ . Consequently, the energy levels spacings become infinitesimal and the system can be described as a continuous distribution of states. Thus, we define a density of states,  $\rho(\varepsilon)$ , and the sum in equation (2.2) can be substituted by integral,

$$N = N_0 + \int_0^\infty n_\varepsilon \rho(\varepsilon) d\varepsilon \quad , \quad (2.3)$$

where we separated the term  $N_0$ , which refers to the population of ground state ( $\varepsilon = 0$ ) because for  $\varepsilon \rightarrow 0$ , typically, we have that  $\rho(\varepsilon) \rightarrow 0$ . The population in the ground state is very small, except for the special case of Bose-Einstein condensation in which it becomes macroscopic, hence, it is convenient to study separately the term for  $N_0$ .

For bosons  $\mu$  is always negative, increases monotonically with decreasing the temperature  $T$  and becomes  $\mu = 0$  for any temperature value in which  $T \leq T_C$ . (3) When  $\mu = 0$  the integral of Equation (2.3) takes its maximum value which saturates the occupation number of the excited states. This means that, for  $T \leq T_C$  any particle added in the system will accumulate in the ground-state, increasing  $N_0$ . This change in the system behavior characterizes a phase transition (Bose-Einstein condensation) in which the atom fraction in the ground state can be used as an order parameter:

$$\frac{N_0}{N} = \begin{cases} 0 & , \text{ if } T > T_C \\ 1 - \frac{1}{N} \int_0^\infty n_\varepsilon \rho(\varepsilon) d\varepsilon & , \text{ if } T \leq T_C \end{cases} \quad (2.4)$$

We can generalize the density of states for a confined gas using the standard textbooks calculation for a free gas. (3,5) The external potential constrains the energy-space available to the gas, therefore the density of states, in thermodynamic limit ( $\varepsilon_{i+1} - \varepsilon_i \ll k_B T$ ) and assuming the semiclassical approximation, can be written as

$$\rho(\varepsilon) = \frac{2\pi(2m)^{3/2}}{h^3} \int \sqrt{\varepsilon - V(\mathbf{r})} d^3r \quad . \quad (2.5)$$

To evaluate the density of states from Equation (2.5) we have to explicit the spacial dependence of the potential that are confining the bosons. In what follows we will calculate the density of states for two confinement cases: the box trap and the anisotropic harmonic

trap. Despite well-known, this calculation provides an overview of essential quantities for the condensation.

### 2.1.1 Ideal Bose gas in a box trap

We will consider a gas of non-interacting bosons, with mass  $m$ , confined in a box potential of volume  $\mathcal{V}$ . The density of states is calculated from Equation (2.5) and results in

$$\rho(\varepsilon) = \frac{2\pi(2m)^{3/2}}{h^3} \mathcal{V} \sqrt{\varepsilon} . \quad (2.6)$$

Applying this result in Equation (2.3) and equating  $N = 0$  and  $T = T_C$  (where  $\mu \rightarrow 0$ ) we obtain the condition for the phase transition of the system, as described above,

$$\left(\frac{N}{\mathcal{V}}\right) \left(\frac{h}{\sqrt{2\pi m k_B T_C}}\right)^3 = 2.612 . \quad (2.7)$$

The critical temperature  $T_C$  for the phase transition can be calculated from Equation (2.7). In BEC experiments of  $^{87}\text{Rb}$  atoms, the densities are typically  $\frac{N}{\mathcal{V}} \sim 10^{13} - 10^{14}$  atoms/cm<sup>3</sup> which leads to  $T_C \approx 100 - 300$  nK.

Equation (2.7) also provides a visible interpretation for the condensation. We can identify the thermal de Broglie wavelength at a temperature  $T$ :  $\lambda_{dB} = \frac{h}{\sqrt{2\pi m k_B T}}$ . For  $^{87}\text{Rb}$  atoms, close to the transition  $\lambda_{dB} \approx 1 \mu\text{m}$ , which is of the order of the mean distance between the particles in typical experimental conditions. Therefore, the condensation can be visualized as if the atoms wave packet had the size of the particles spacing which generates a giant matter wave.

The right side of Equation (2.7) represents the phase-space density of the atoms, PSD =  $n\lambda_{dB}^3$ , where  $n = N/\mathcal{V}$  is the density of atoms. This quantity works like an universal marker to transition (58): if its value is higher than 2.612 it will have a phase transition which are known as Bose-Einstein condensation (BEC). Using the Equation (2.6) we can

rewrite the Equation (2.4) to calculate the condensation fraction as a function of the temperature. In this way, we obtain the textbooks results for the order parameter of the transition:

$$\frac{N_0}{N} = 1 - \left( \frac{T}{T_C} \right)^{3/2} . \quad (2.8)$$

### 2.1.2 Ideal Bose gas in an anisotropic harmonic trap

In most of the experiments with ultracold trapped gases, the bottom of the confining potential can be approximated by a harmonic shape. A general discussion for arbitrary polynomial potential can be found in (58) reference. Here, we will discuss the typical case of a three-dimensional anisotropic harmonic potential:

$$V(x, y, z) = \frac{m}{2} (\omega_x^2 x^2 + \omega_y^2 y^2 + \omega_z^2 z^2) , \quad (2.9)$$

where  $\omega_j$  is the oscillator frequency along  $j = x, y, z$  directions.

The density of states is calculated from Equation (2.5) and (2.9), which results in

$$\rho(\varepsilon) = \frac{1}{2} \frac{\varepsilon^2}{(\hbar\bar{\omega})^3} , \quad (2.10)$$

where  $\bar{\omega} = (\omega_x \omega_y \omega_z)^{1/3}$  is the geometric mean of the trap frequencies.

As done in the previous section, we obtain that the critical temperature in this case is

$$T_C = 0.941 \frac{\hbar\bar{\omega}}{k_B} N^{1/3} . \quad (2.11)$$

This equation describes an equivalent criterion to determine the condition to reach the phase transition, as the Equation (2.7).

In this case, the condensed fraction as a function of the temperature is

$$\frac{N_0}{N} = 1 - \left( \frac{T}{T_c} \right)^3 . \quad (2.12)$$

Comparing the Equation (2.12) with the Equation (2.8), which was obtained for a box potential, we conclude that in a harmonic trap, as the temperature is lowered, the atoms populates the ground state faster than in the previous case.

In the next section we will describe a more realistic case, where we take into account the effects caused by the interaction between the particles

## 2.2 Weakly interacting Bose gas

Bose-Einstein condensates confined in a potential have high densities ( $\sim 10^{14}$  atoms/cm<sup>3</sup>), thus the interactions between the particles play an important role when we are studying the BEC phase transition, wavefunction, dynamics and thermodynamics properties. In this section we are going to present the Gross-Pitaevskii equation (GPE) which approximately describes this interacting system. More details about GPE can be found in (60–62) references.

### 2.2.1 Gross-Pitaevskii equation

The Gross-Pitaevskii equation was simultaneously and independently formulated by Eugene Gross (63) and Lev Pitaevskii (64) to describe quantized vortices in a Bose gas. This equation can be derived from the many-body Hamiltonian in second quantization (60, 62). The assumption is that all the bosons of the system are in the same quantum state, thus the system is approximated described by one single-particle state,  $\psi(\mathbf{r}, t)$ , and the condensate density is determined by  $n = |\psi(\mathbf{r}, t)|^2$ .

The diluteness conditions implies that in condensed clouds the scattering length,  $a$ , is much smaller than the typical particle separation,  $n|a|^3 \ll 1$ . Under this condition,

the cloud is dilute enough such that only the two-body interactions are relevant and it can be modeled by a pseudo-potential given by a Dirac delta:  $V_{int}(\mathbf{r}) = g\delta(\mathbf{r} - \mathbf{r}')$ , where  $\mathbf{r}$  and  $\mathbf{r}'$  are the two atoms positions, and  $g$  is the atoms effective interaction which is related to the atomic mass,  $m$ , and the scattering length,

$$g = \frac{4\pi\hbar^2}{m}a \quad . \quad (2.13)$$

These approximations results in an important equation for the condensate wave-function, in a trap potential  $V(\mathbf{r})$ ,

$$i\hbar\frac{\partial\psi(\mathbf{r},t)}{\partial t} = \left[ -\frac{\hbar^2}{2m}\nabla^2 + V(\mathbf{r}) + g|\psi(\mathbf{r},t)|^2 \right] \psi(\mathbf{r},t) \quad , \quad (2.14)$$

which is the time-dependent Gross-Pitaevskii equation, also known as nonlinear Schrödinger equation.

The GPE takes a simple form in the case of stationary solutions where the condensate wave function evolves in time according to  $\psi(\mathbf{r},t) = \phi(\mathbf{r})e^{-i\frac{\mu}{\hbar}t}$ . The GPE reduces to the time-independent GPE,

$$\left[ -\frac{\hbar^2\nabla^2}{2m} + V(\mathbf{r}) + g|\phi(\mathbf{r})|^2 \right] \phi(\mathbf{r}) = \mu\phi(\mathbf{r}) \quad , \quad (2.15)$$

where  $\mu$  is the chemical potential. We can find the chemical potential from the normalization condition of the wave function ,

$$N = \int |\phi(\mathbf{r})|^2 d^3r \quad . \quad (2.16)$$

In the absence of interactions ( $g = 0$ ), the equation (2.15) becomes the Schrödinger equation for a particle. If the confining potential is harmonic, we will have a quantum harmonic oscillator. Thus, in this case, the wave function of the fundamental state has a Gaussian shape with a characteristic length given by the harmonic oscillator length,

$$a_{ho} = \sqrt{\frac{\hbar}{m\omega}} \quad . \quad (2.17)$$

This oscillator length is the cloud radius,  $R$ , in the equilibrium between the kinetic and potential energy.

When the interactions are taken into account,  $\langle g |\phi(\mathbf{r})|^2 \rangle = \langle gn(\mathbf{r}) \rangle \approx gN/R^3$ , we can see that the mean-field energy term is proportional to  $R^{-3}$  and, as it is an additional term to the potential energy, the consequence is that the equilibrium condition will be given at a different distance. Therefore, one effect of the interactions is to increase (or decrease) the cloud radius in case where the interactions are repulsive (or attractive).

### 2.2.2 Thomas-Fermi approximation

For repulsive interactions, an important energy regime happens when the kinetic energy can be neglected with respect to the interaction energy. In harmonic trap, the ratio between these two energies varies as (60):  $E_{int}/E_{kin} \propto Na/a_{ho}$ .

In the experimental regime of parameters that condensation normally takes place, the condition  $Na/a_{ho} \gg 1$  is satisfied and the *Thomas-Fermi approximation*(TFA) can be done by omitting the kinetic energy term in the Gross-Pitaevskii equations. From Equation (2.15) we obtain

$$\left[ V(\mathbf{r}) + g |\phi(\mathbf{r})|^2 \right] \phi(\mathbf{r}) = \mu \phi(\mathbf{r}) \quad . \quad (2.18)$$

The Equation (2.18) is an algebraic equation and the solution describes the density of the condensed atoms, which we call as Thomas-Fermi profile:

$$n(\mathbf{r}) = |\phi(\mathbf{r})|^2 = \begin{cases} \frac{\mu - V(\mathbf{r})}{g} & , \text{ if } \mu > V(\mathbf{r}) \\ 0 & , \text{ if } \mu \leq V(\mathbf{r}) \end{cases} \quad . \quad (2.19)$$

We can see that the condensate density profile is proportional to the inverse of the confining potential.

Typically atoms are trapped in an anisotropic harmonic potential. According to Equation (2.19) the density profile of the BEC will reflect this with an anisotropic parabolic shape. This profile will be discussed in section 3.6.

### 2.2.3 Hydrodynamic equations

In the last section we were concerned with the description of the BEC through the time-independent GPE because we were interested in the stationary solutions of this equation. In this section we are interested in the time evolution, and hence, we will develop a set of equations which can be used to describe the condensate dynamics.

The Gross-Pitaevskii equation, Equation (2.14), can be written in a form of a hydrodynamic continuity equation. We have to multiply the GPE by  $\psi^*(\mathbf{r}, t)$  and, from this resulting equation, subtract its complex conjugate. This operation yields to

$$\frac{\partial |\psi|^2}{\partial t} + \nabla \cdot \left[ \frac{\hbar}{2mi} (\psi^* \nabla \psi - \psi \nabla \psi^*) \right] = 0 . \quad (2.20)$$

The Equation (2.20) is the continuity equation for a BEC. We can identify the current density,  $\mathbf{j}(\mathbf{r}, t)$ , as

$$\mathbf{j}(\mathbf{r}, t) = -i \frac{\hbar}{2m} (\psi^* \nabla \psi - \psi \nabla \psi^*) . \quad (2.21)$$

From Equation (2.20) we can find an expression to the velocity field of the BEC,  $\mathbf{v}(\mathbf{r}, t)$ . For this we can write the condensate wave function (the order parameter) in terms of the condensate density  $n(\mathbf{r}, t)$  and its phase  $S(\mathbf{r}, t)$ ,

$$\psi(\mathbf{r}, t) = \sqrt{n(\mathbf{r}, t)} e^{iS(\mathbf{r}, t)} . \quad (2.22)$$

Applying the Equation (2.22) into Equation (2.21) and remembering that  $\mathbf{j} = n\mathbf{v}$ , we obtain the condensate velocity field:

$$\mathbf{v}(\mathbf{r}, t) = \frac{\hbar}{m} \nabla S(\mathbf{r}, t) . \quad (2.23)$$

Finally, substituting the Equation (2.22) into GPE, Equation (2.14), results in a time-dependent equation for the condensate velocity field:

$$m \frac{\partial \mathbf{v}}{\partial t} + \nabla \cdot \left( \frac{m\mathbf{v}^2}{2} + V + gn - \frac{\hbar^2}{2m\sqrt{n}} \nabla^2 \sqrt{n} \right) = 0 , \quad (2.24)$$

the last term inside the parentheses of this equation is the quantum pressure term. (62)

The Equations (2.20) and (2.24) are the BEC hydrodynamic equations, and they are equivalent to the GPE. In the next section, we will use these equations to describe the collective excitation modes of a Bose-Einstein condensate.

## 2.3 Collective modes of a trapped condensate

In the Thomas-Fermi approximation, the quantum pressure term from Equation (2.24) can be neglected with respect to the interacting term (62), because as the number of trapped atoms are sufficiently large, the density profile,  $n(\mathbf{r}, t)$ , varies smoothly. Thus, the hydrodynamic equation becomes

$$m \frac{\partial \mathbf{v}}{\partial t} + \nabla \left( \frac{m \mathbf{v}^2}{2} + V + gn \right) = 0 \quad . \quad (2.25)$$

The collective modes are investigated by considering small deviations of the coherent mode (stationary solution of GPE) from equilibrium and finding periodic solutions of the hydrodynamic equations. (61) We can write the density as  $n(\mathbf{r}, t) = n_0(\mathbf{r}) + \delta n(\mathbf{r}, t)$ , where  $n_0(\mathbf{r})$  is the coherent mode and  $\delta n(\mathbf{r}, t)$  the departure of the density from its equilibrium value. By treating  $\delta n(\mathbf{r}, t)$  and  $\mathbf{v}(\mathbf{r}, t)$  as small quantities, we can linearize the Equations (2.20) and (2.25) which results in

$$\frac{\partial \delta n}{\partial t} + \nabla \cdot (n_0 \mathbf{v}) = 0 \quad (2.26)$$

and

$$m \frac{\partial \mathbf{v}}{\partial t} + g \nabla \delta n = 0 \quad , \quad (2.27)$$

where we used that:  $\frac{\partial n_0}{\partial t} = 0$ , because  $n_0$  is a stationary solution of GPE, and the spatial variation of  $n_0$  is much smaller than the variation of  $\delta n$ ,  $|\nabla n_0| \ll |\nabla \delta n|$ .

Taking the time derivative of Equation (2.26) and using the Equation (2.27) to eliminate the velocity, results in the equation of motion

$$\frac{\partial^2 \delta n}{\partial t^2} = \nabla \cdot (c^2 \nabla \delta n) \quad , \quad (2.28)$$

where  $mc^2 = gn_0$  and from Equation (2.19) we can write  $mc^2 = \mu - V(\mathbf{r})$ . The quantity  $c(\mathbf{r})$  represents a local sound velocity.

Now, to find periodic solutions from Equation (2.28), we use a temporal oscillatory ansatz for the density fluctuation,  $\delta n(\mathbf{r}, t) = \delta n(\mathbf{r})e^{-i\omega t}$ , and its result in

$$\omega^2 \delta n(\mathbf{r}) = \nabla \cdot (c^2 \nabla \delta n) \quad . \quad (2.29)$$

The solutions of the Equation (2.29) correspond to the low-lying frequency modes of a condensate that are obtained (59) by solving the Bogoliubov-de Gennes equation.

In the case of our experiment, the confining potential is harmonic and has a symmetry axis (see section 3.5), the collective modes are described by the equation:

$$m\omega^2 \delta n(\mathbf{r}) = \nabla \cdot \left\{ \left[ \mu - \frac{m}{2} (\omega_r^2 r^2 + \omega_x^2 x^2) \right] \nabla \delta n \right\} = 0 \quad , \quad (2.30)$$

where  $\omega_x$  is the trap frequency along the symmetry axis and  $\omega_r = \omega_y = \omega_z$  is the frequency along the radial direction  $r^2 = y^2 + z^2$ .

Due to the axial symmetry of Equation (2.30), the density fluctuations are described with functions of the form:  $\delta n \propto P(r)Y_{\ell m}(\theta, \varphi)$ , where  $P(r)$  are functions with radial dependence and  $Y_{\ell m}(\theta, \varphi)$  are the spherical harmonics. (65) Explicit results of Equation (2.30) are available in some particular cases. For example, for the case that the density fluctuations of the form  $\delta n \sim r^l Y_{\ell m}(\theta, \varphi)$  are solutions of this equation for  $m = \pm \ell$  and  $m = \pm(\ell - 1)$ , which results in the dispersion laws

$$\text{for } m = \pm \ell: \quad \omega_{\ell m}^2 = \ell \omega_r^2 \quad , \quad (2.31)$$

$$\text{for } m = \pm(\ell - 1): \quad \omega_{\ell m}^2 = (l - 1)\omega_r^2 + \omega_x^2 \quad . \quad (2.32)$$

Through the value of  $\ell$  the low-laying modes can be labeled as:

**(i) Dipole oscillations (or dipolar modes):**  $\ell = 1$ .

In this case,  $\delta n \sim r Y_{1m}(\theta, \phi)$  and the frequencies of this mode are:

$$\omega_{D,\pm 1} = \omega_r \quad , \quad (2.33)$$

$$\omega_{D,0} = \omega_x \quad . \quad (2.34)$$

This mode corresponds to the translation of the cloud inside the trap with no deformation in its shape, i.e. the cloud center of mass (CM) oscillates. The frequencies of this mode coincides with the trap frequencies, a fact that makes it a precise tool to characterize the trap (27), as we will present in sections 3.5 and 4.4.

**(ii) Quadrupole oscillations (or quadrupolar modes):  $\ell = 2$ .**

In this case,  $\delta n \sim r^2 Y_{2m}(\theta, \phi)$  and Equations (2.31) and (2.32) only account the frequencies for  $m = \pm 1$  and  $m = \pm 2$  components:

$$\omega_{Q,\pm 2} = \sqrt{2}\omega_r \quad , \quad (2.35)$$

$$\omega_{Q,\pm 1} = \sqrt{\omega_r^2 + \omega_x^2} \quad . \quad (2.36)$$

The solution for the quadrupole mode with  $m = 0$  is coupled with the monopole mode ( $\ell = 0$ ). (61) In this case, the solutions of Equation (2.30) are:

$$(\omega_{\ell 0}^2 - 4\omega_r^2)(\omega_{\ell 0}^2 - 3\lambda^2\omega_r^2) - 2\lambda^2\omega_r^4 = 0 \quad , \quad (2.37)$$

where  $\lambda = \frac{\omega_x}{\omega_r}$ . Thus, the dispersion laws are given by

$$\omega_{B,0}^2 = \omega_r^2 \left( 2 + \frac{3}{2}\lambda^2 + \frac{1}{2}\sqrt{9\lambda^4 - 16\lambda^2 + 16} \right) \quad (2.38)$$

and

$$\omega_{Q,0}^2 = \omega_r^2 \left( 2 + \frac{3}{2}\lambda^2 - \frac{1}{2}\sqrt{9\lambda^4 - 16\lambda^2 + 16} \right) \quad . \quad (2.39)$$

Typically, the  $m = 0$  fast mode, described by Equation (2.38), is called breathing mode. For a cigar-shaped trap,  $\lambda \ll 1$ , the two frequencies become  $\omega_{B,0} = 2\omega_r$  and  $\omega_{Q,0} = \sqrt{\frac{5}{2}}\omega_x$ . These two modes are characterized by the changing in the condensate shape (66), and this can be measured from the condensate aspect ratio or from the condensate radii.

Figure 1 illustrates the manifestation of the dipolar and quadrupolar modes in a Bose-Einstein condensate, for the fundamental frequency of each mode. In chapter 4 we will study the manifestation of these modes by magnetically oscillating a Bose-Einstein condensate.

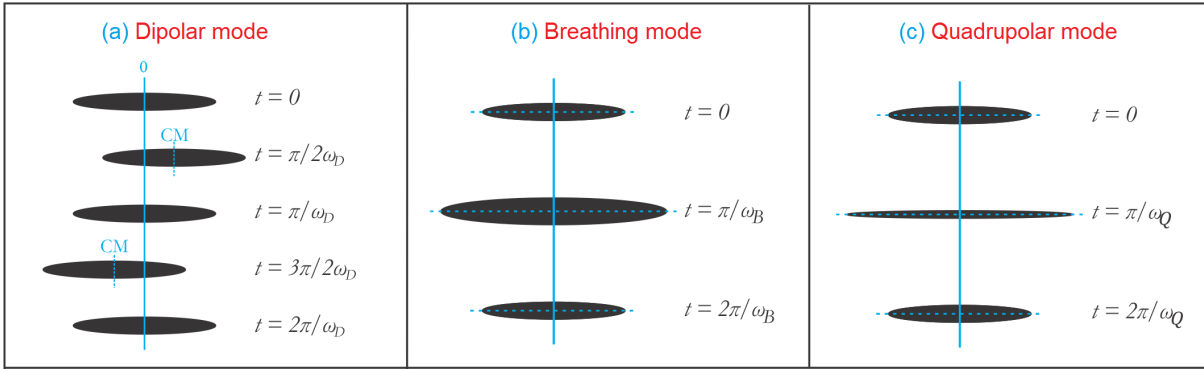


Figure 1 – Illustration of the BEC low-lying collective modes. The condensate is trapped in a harmonic cigar-shaped trap potential and the low-lying modes are: (a) Dipolar mode, (b) Breathing mode and (c) Quadrupolar mode. These figures refers to the fundamental frequencies of each mode.

Source: By the author.

## 2.4 Turbulence

In fluid dynamics, turbulence or turbulent flow is a regime characterized by a non-regular (chaotic) motion of fluids and is present in many everyday situations. This extraordinary phenomena has tracked the curiosity of great researchers and also artists. Even though in the 15th century, Leonardo da Vinci (67, 68) made a first qualitative description of turbulence flow, turbulence remains “the most important unsolved problem of classical phenomena”, as declared by Richard P. Feynman. Furthermore, in 1955 Feynman was the first to predict the existence of turbulence in superfluids. (18) The superfluid flow is known to be constrained by quantum restrictions, and this motivated Russel J. Donnelly (69) to name the turbulence in superfluids as *Quantum Turbulence (QT)*.

Despite have being studied for hundreds of years, our understating of turbulence still is not complete and a lot of work and research are devoted to this topic. In what follows, we present an overview of the principal concepts and characteristics of turbulence in classical fluids (classical turbulence, CT) and in quantum fluids (quantum turbulence, QT). A deeper discussion about this topic can be found in (70) a recent review article.

### 2.4.1 Classical fluids

Here we will briefly discuss the fundamental equations, the dynamical regimes and the turbulent flow properties of classical fluids. In references (68, 71) more details about the classical fluids flow can be found.

The classical fluid dynamics is governed by the non-linear Navier-Stokes equation. For an incompressible fluid with density  $\rho$  and viscosity  $\eta$ , under a pressure force  $\nabla P$  and external forces  $\mathbf{f}$ , the fluid velocity field  $\mathbf{v} = \mathbf{v}(\mathbf{r}, t)$  is described by the Navier-Stokes equation and is written as

$$\frac{\partial \mathbf{v}}{\partial t} + (\mathbf{v} \cdot \nabla) \mathbf{v} = -\frac{1}{\rho} \nabla P + \nu \nabla^2 \mathbf{v} + \mathbf{f} \quad , \quad (2.40)$$

where  $\nu = \frac{\eta}{\rho}$  is the kinematic viscosity of the fluid. The left-side terms describes the fluid acceleration, the second term  $(\mathbf{v} \cdot \nabla) \mathbf{v}$  is particularly important which is known as the nonlinear inertial force and is responsible for the convection process. In the right-side, the term  $\nu \nabla^2 \mathbf{v}$  describes the viscous force and is related to diffusion process, the term proportional to  $\nabla P$  accounts for the pressure gradient and is related to the internal forces in the fluid while the term  $\mathbf{f}$  accounts for the external forces.

Experimentally studying the transition from laminar to turbulent flows (72, 73), Osborne Reynolds understood the interplay of viscous and inertial forces. He recognized an important quantity, useful to describe the dynamical ranges of the fluid flow, the dimensionless Reynolds number,  $Re$ . (74) This quantity is defined as the ratio between the magnitude of the inertial force,  $(\mathbf{v} \cdot \nabla) \mathbf{v}$ , and the magnitude of the viscous force,  $\nu \nabla^2 \mathbf{v}$ . Thus, the Reynolds number quantifies the relative importance of these two types of forces for given flow conditions. For example, a fluid flowing with a velocity  $v$  finds an obstacle with a transversal section of size  $D$ , will have a Reynolds number  $Re = vD/\nu$ . At small Reynolds number, the viscous force is dominant and the fluid motion is constant and smooth, characterizing a laminar flow. On the other hand, if the Reynolds number is large, the non-linear inertial force dominates the motion, the laminar profile is destabilized and tend to produce chaotic eddies with different sizes and other flow

instabilities, characterizing a turbulent flow.

The evolution to a turbulent regime can be explained with the Richardson cascades (75) picture. From a laminar flow, when the Reynolds number condition to a turbulent flow is reached occurs the formation of large eddies (or vortices). These vortices are unstable and they broke into smaller vortices. By themselves, these new vortices suffer the same process, dividing into even smaller eddies. Successively, this process repeats until the eddies length scales become very small so that the Reynolds number is  $Re \sim 1$ . In this case, the viscosity effect start to be dominant and the energy is dissipated. This process creates a path for the energy flow going from large to small eddies (or scales) until it dissipated. We can clearly identify three ranges of length scale: the first is called energy containing range and describe the process when energy is input in the system but the flow still laminar; the second is the inertial range where the Richard cascade occurs; finally, the third one is the dissipation range.

Andrey N. Kolmogorov (76, 77) propose that the Richardson cascades have an universal law for the inertial range. In the Kolmogorov's theory, the range of length scales ( $r$ ) is described with the wavenumber  $k = 2\pi/r$  and corresponds to  $k_D \ll k \ll k_K$ , where the lower limit  $k_D$  is related to the largest scale length and for a energy injection rate  $\varepsilon$ , the upper limit of the range is defined as  $k_K = (\varepsilon/\nu^3)^{1/4}$ . In this range, the Kolmogorov energy spectrum is

$$E(k) = C\varepsilon^{2/3}k^{-5/3} \quad (2.41)$$

where  $C$  is a dimensionless constant, experimentally found to be around 0.5 (78) and  $k$  is the wavenumber obtained from the Fourier transform of the fluid velocity field.

The Kolmogorov spectrum, Equation (2.41), present some important properties. We can highlight the remarkable universality since it only depends on  $k$  and  $\varepsilon$  (this means that it is independent of the fluid nature, boundary conditions of the system and the mean velocity flow field). This universal character was demonstrated (79) by measuring the normalized energy spectrum for several physical system. We also point out that the Kolmogorov law describes the self-similarity of the turbulence along all length scales included in the inertial range, typical characteristic of a universal system ("free of

scale”).

## 2.4.2 Quantum fluids

Now, we will briefly describe the new aspects that turbulence manifests in the quantum world of superfluid helium and atomic condensate. In references (80,81) can be found a very good introduction and discussion about quantum turbulence (QT).

We may start the discussion by showing that quantum effects restrict the superfluid flow. For this, we have to return to the superfluid velocity field described by Equation (2.23). We can see that the superfluid flow is irrotational, i.e.  $\nabla \times \mathbf{v} = 0$ . This is true unless the phase of the wave function has a singularity. In the case of the existence of this singularity (like a vortex), a circulation in the phase around this point has to be a multiple of  $2\pi$ , because the wave function has a unique value. Thus, the circulation of the velocity field is quantized,

$$\Gamma = \oint \mathbf{v} d\mathbf{l} = 2\pi\ell \frac{\hbar}{m} = \ell \frac{h}{m}, \quad (2.42)$$

where  $d\mathbf{l}$  is line element of integration and  $\ell$  is an integer number that specifies the “quanta” of circulation. This equation implies that the circulation of the velocity field around a vortex is quantized. Thus, in superfluid the only way to have rotational flow is by means of quantized vortices.

A vortex is a topological defect whose equilibrium extension is of the order of the healing length,  $\xi$ . This characteristic internal size of a condensate is defined (61) as the length scale which the kinetic energy becomes comparable with the interaction energy,

$$\frac{\hbar^2}{2m} |\nabla\psi|^2 \sim g|\psi|^4 \quad (2.43)$$

thus

$$\frac{\hbar^2}{2m} \frac{|\psi|^2}{\xi^2} = g|\psi|^4 \Rightarrow \xi = \frac{\hbar}{\sqrt{2mgn}} = \frac{1}{\sqrt{8\pi an}}, \quad (2.44)$$

where  $n$  is the superfluid bulk density and in the last step we use the Equation (2.13). For  $^4\text{He}$  superfluid the healing length is of the order of a few angstroms, while for an atomic BEC this value is typically a few microns. This fact makes the atomic BEC a better physical system to observe and study such topological defects.

The turbulence in quantum fluids was proposed by Feynman (18) and consists of a configuration of vortices in which the vortex lines are spatially tangled. The Feynman idea was experimentally demonstrated by William Vinen and Henry Hall (19, 82–85) in superfluid helium where they produced a thermal counterflow between the normal fluid and superfluid fraction and observed tangled vortices in superfluid component.

Other important experiments on turbulence in superfluid  $^4\text{He}$  were done by the group of P. Tabeling (86) and by the group of R. J. Donnelly (87), simultaneously. They showed that the Kolmogorov spectrum is satisfied in turbulent  $^4\text{He}$  superfluid, for a specific inertial range, and it is independent of the fluid temperature. This is an impressive result, considering the differences between the classical fluids and quantum fluids flow.

This implies that the energy transport process in quantum turbulence is equivalent to the classical turbulence one. Which means that it is based on the Richardson cascades. But with an important difference from the classical system. The dissipation mechanism in superfluid cannot be related to the fluid viscosity, as in classical turbulence, and the other obvious mechanism would be through the normal fluid fraction. In fact this happens, but it is not enough since at very low temperatures the normal fluid component is less than 2% of the total fluid and the Kolmogorov spectrum is still valid.

To explain how quantum turbulence is formed and dissipates, the most accepted hypothesis is a process known as vortex reconnections. (88, 89) When two straight vortices, with well defined orientations, interact and approach each other close enough, they can reconnect at a certain point for some short time. After the reconnection, two vortices emerge with a kinked form. In a superfluid containing many distributed vortices, the reconnections will occur frequently and form a big tangle with all other vortex. This is exactly the Feynman scheme for superfluid turbulence. As consequence of many reconnections, a vibration will be generated in each vortex line. This excitation is known

as (90, 91) Kelvin waves (like phonon radiation). In superfluids, the Kelvin waves can transfer energy from the inter-vortex scale to smaller scales (92–94), as the vortex core. Therefore, this becomes an important mechanism in the decay of turbulence because the energy is transferred from larger length scales to smaller scales of the system (95), where it is dissipated.

There are two principal approaches to describe theoretically the quantum turbulence. The first is more appropriated to describe the QT in helium superfluids due to the smaller vortex size. This approach is known as the filament model (96) in which the flow around a filament (vortex) is expressed by a Biot-Savart law expression. The other approach (93, 97) consists in solving the Gross-Pitaevskii equation with an additional term responsible for the dissipation. This method is applicable for atomic BECs, because the superfluid helium is not a weakly interacting system.

A remarkable result for atomic BEC is presented in references (93, 97), where they simulated a trapped BEC rotating around two perpendicular axes. They found that the initial configuration evolves into a QT regime following the Kolmogorov power law, in the inertial range between  $\frac{2\pi}{R_{TF}} < k < \frac{2\pi}{\xi}$ , where  $R_{TF}$  is the condensate radius and  $\xi$  the healing length. The interest in experimentally produce turbulence in atomic BECs has been heavily motivated by this theoretical predictions and by the progress in understanding quantum turbulence in liquid helium. The first experimental evidence of QT in dilute BECs was provided by our research group (33) and it has an indication (57) that this system exhibits a Kolmogorov like power-law spectrum. In this work, the exponent in the  $k$  dependence does not match with the Kolmogorov spectrum, Equation (2.41). In Chapter 5 of this thesis, we will give a justification about this discrepancy.



## 3 Experimental apparatus

In our research group there are three experimental systems designed to study Bose-Einstein condensates. This thesis is inserted in the so called *BEC-I* experiment. The first version of this experimental system is described in (38,98) Ph.D. theses, (99,100) master theses and (101) an article. The new version of this experimental system will be briefly discussed in this chapter. There were many upgrades since the first version, but the main idea remains the same.

### 3.1 Experiment overview

In order to reach Bose-Einstein condensation in dilute gases, it is necessary to bring a monoatomic gas to temperatures and densities of the order of  $10^2$  nK and  $10^{14}$  cm<sup>-3</sup>. This is only possible if the atoms are isolated inside a region free from impurities and from material walls. This is done by putting the atoms inside an ultrahigh vacuum chamber and trapping them with magnetic field and/or laser light.

In general lines, our vacuum system is composed by two chambers. The first chamber, where we have the atoms source (dispensers and LIAD), is kept at a pressure of  $P \sim 10^{-9}$  Torr. The pressure of the second chamber is  $P \sim 10^{-12}$  Torr, presenting the ideal conditions to produce Bose-Einstein condensates.

Three commercial high-power lasers (from Toptica: two DLX110L and one TA pro) compose our lasers system. The lasers are locked, individually and actively, to one appropriate hyperfine line of the <sup>87</sup>Rb atom observed by Doppler-free spectroscopy in a vapor cell. The output light is used for atomic cooling, trapping, manipulating the atomic states and to probe the atoms.

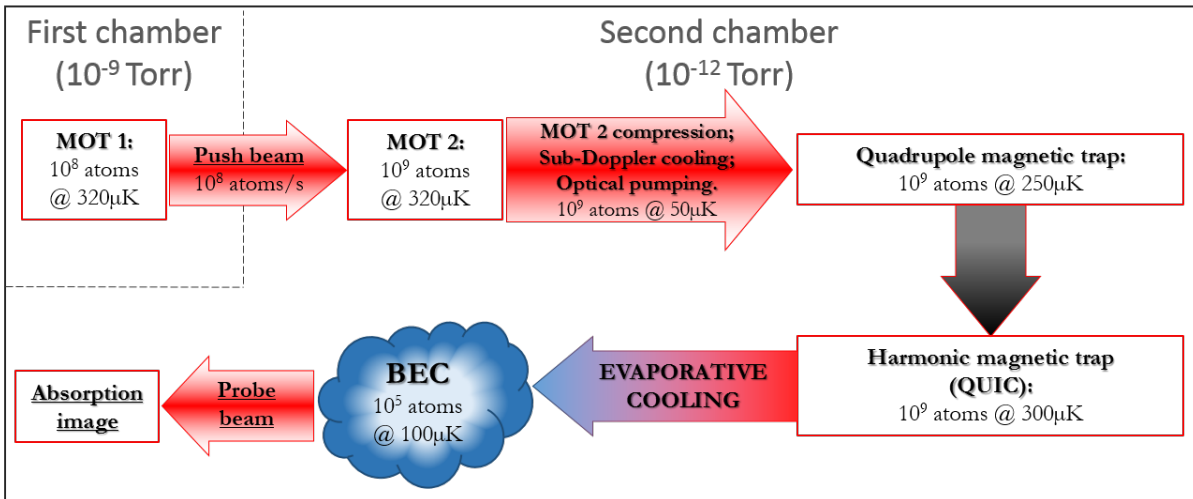


Figure 2 – Diagram of processes in the experimental sequence to produce a Bose-Einstein condensate in our apparatus. Typical final atom numbers and temperatures are presented for each step. This experimental sequence has a duration of about 1 minute.

Source: By the author.

Several stages are used to reach the Bose-Einstein condensation. Figure 2 shows a schematic diagram of the involved process in our experimental sequence. To control the experimental sequence we program a *Labview* routine in a control computer. The communication with the experiment is done by two *National Instruments* NI-DAQ boards (NI-6733 and NI-6259), from where we extract the analogical and digital signals that are used during the experiment. Finally, as the experimental sequence ends, after about one minute, the experimental data (specially the atomic cloud absorption image) are acquired and analyzed in an acquisition computer.

## 3.2 Vacuum system

In dilute gases systems, the sample lifetime in a trap is better the lower the background pressure. Thereby, a vacuum system is essential and important in cold atoms experiments, specially for those where the cooling processes depend on longer thermalization times, as it is the case for evaporative cooling. (23)

Each experiment in cold atoms has a particular vacuum system configuration. (50,

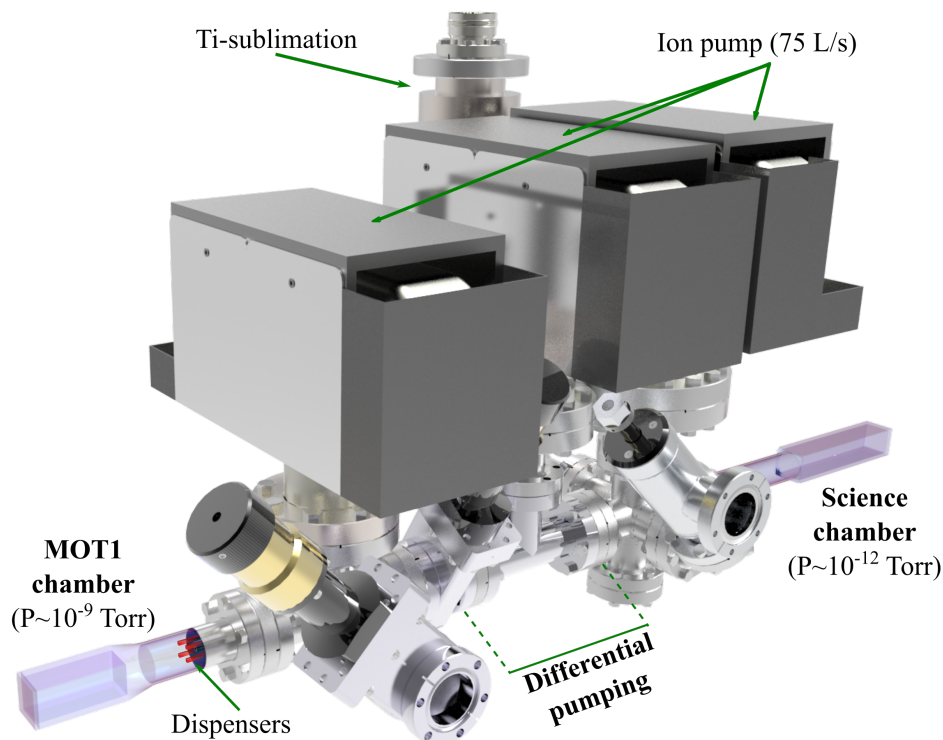


Figure 3 – New vacuum system 3D drawing. The three ion pumps are responsible to pump the MOT1 chamber, the differential pumping stage and the science chamber.

Source: By the author.

102,103) A common choice is a two chambers configuration. Typically, the first chamber is a high-vacuum region, with a pressure of about  $P \sim 10^{-9}$  Torr, where the atom sources are located. The second one is an ultra-high-vacuum region,  $P \sim 10^{-12}$  Torr, which provides the ideal background pressure conditions to manipulate the atoms until the production of a BEC. To reach this vacuum level it is necessary a differential pumping between the two regions.

We have constructed the new vacuum system of our apparatus at the beginning of my Ph.D. and at the end of R. F. Shiozaki Ph.D. (in 2012). In Figure 3 we present a 3D drawing of this system, which is a double-MOT configuration. (102) It can be divided into three regions: the first region, where there are atoms source and the first magneto-optical trap (MOT1) is produced; the second region is the differential pumping stage; and the third one, where the second magneto-optical trap (MOT2) is formed and the BEC is achieved (we normally call this region as science chamber). Details about the calculations and estimations for this system can be found in R. F. Shiozaki thesis. (98)

The first chamber (MOT1 region) is a rectangular cell, with dimensions  $60 \times 30 \times$

30 cm<sup>3</sup>, made of quartz (Hellma). This cell is connected to: an ion pump (Varian 75 L/s), which keeps the pressure around  $4 \times 10^{-9}$  Torr in this region; an electric feedthrough to activate the dispensers, which are inside the MOT1 cell; and the transference tube, that connect the MOT1 region with the MOT2 region and ensure the differential pumping.

The second chamber (MOT2 region) is a quartz cell (Hellma) with dimensions  $150 \times 30 \times 30$  cm<sup>3</sup>, which has a high optical quality, important and necessary for diagnostics by imaging the atomic cloud. The cell is connected to an ion pump (Varian 75 L/s), a titanium sublimation pump (Varian-TSP) and a vacuum meter (Balzers - Cold Cathod Gauge). The transference tube ends inside this chamber and at its middle it is connected to another ion pump (Varian 75 L/s). This configuration creates a differential pumping that allows the pressure in the second chamber to be about four orders of magnitude lower than the first one. The pressure is around  $1 \times 10^{-12}$  Torr in the science chamber.

### 3.3 Double-MOT configuration

In our experimental apparatus, the atoms source is a set of alkali-metal dispensers (SAES Getters). The dispenser contains a mixture of rubidium chromate (Rb<sub>2</sub>CrO<sub>4</sub>) and a reducing agent. An electric current heats the dispenser and its contents to about 600 °C. This initiates a reduction reaction in the mixture and Rb vapor is released in the MOT1 region. (104–106)

The LIAD (*Light-Induced Atom Desorption*) technique (107) with UV LEDs is also applied as an additional atoms source. The UV light desorbs the rubidium atoms from the inner walls of the vacuum chamber. This increases the number of atoms in the rubidium vapor at MOT1 region.

We initially trap <sup>87</sup>Rb atoms in a 3D magneto-optical trap (MOT). Basically, the combination of radiation pressure produced by three pairs of orthogonal counterpropagating laser light beams (with circular polarization) and an inhomogeneous magnetic field

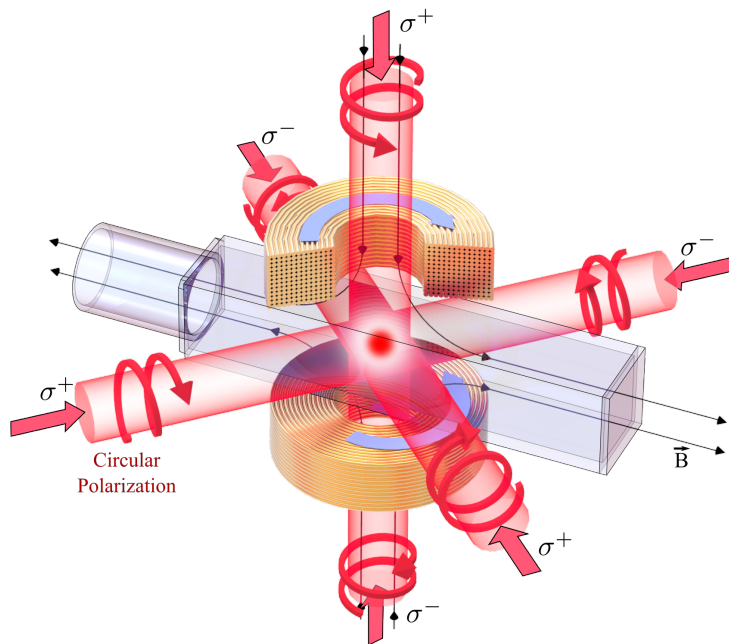


Figure 4 – Schematic draw of a magneto-optical trap configuration. The MOT is composed by three pairs of orthogonal counterpropagating laser beams (with circular polarization) and an inhomogeneous magnetic field (typically produced by a pair of coils in anti-Helmholtz configuration) .

Source: By the author.

(typically produced by a pair of coils in anti-Helmholtz configuration) confines the atoms in a MOT. Figure 4 presents a schematic draw of a MOT configuration. Details about the principle of laser cooling and magneto-optical trapping can be found in (20–22, 108–110) references. The first experimental realization of a MOT was in 1987 (52) and, since then, this trap has been present in almost every cold atoms research apparatus.

The MOT1 optical part is produced by three independent retroreflected laser beams. This light is composed by two superimposed laser beams with different frequencies. One is 20 MHz red-detuned from the  $5^2S_{1/2}(F = 2) \rightarrow 5^2P_{3/2}(F = 3)$  transition of  $^{87}\text{Rb}$  atoms, which we call trapping light. The second light is resonant with the  $5^2S_{1/2}(F = 1) \rightarrow 5^2P_{3/2}(F = 2)$  transition and is called repumper light. The MOT1 magnetic part is composed by a pair of coils in anti-Helmholtz configuration (named quadrupole coils), that generates a magnetic gradient field of around 10 G/cm, and three orthogonal pairs of coils in Helmholtz configuration (named compensation coils), that are used to center the MOT1 in the push beam. Figure 5(a) shows the fluorescence of the trapped atoms in MOT1. Around  $3 \times 10^8$   $^{87}\text{Rb}$  atoms are trapped in MOT1, with a

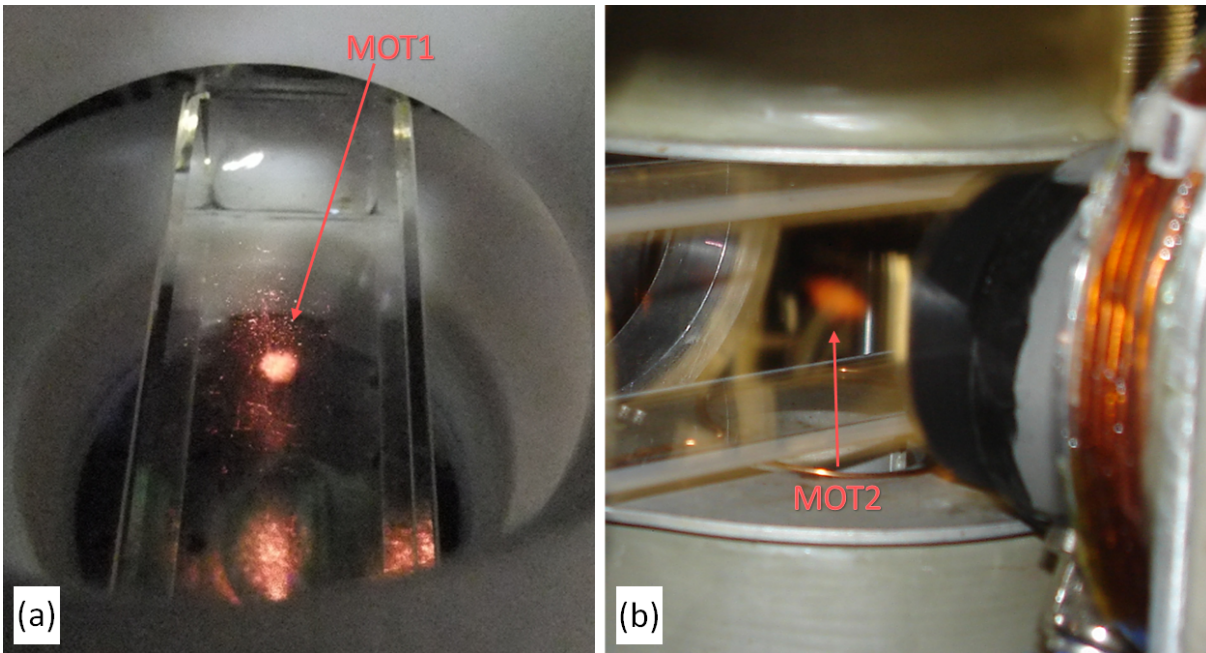


Figure 5 – Pictures of the atoms trapped in the MOTs. (a) Fluorescence of the trapped atoms in MOT1. (b) Fluorescence of the trapped atoms in MOT2.

Source: By the author.

temperature of about  $320 \mu\text{K}$ .

Once the atoms are trapped in MOT1, they are continuously transferred to the ultra-high vacuum region. A small laser beam (called push beam), with 1 mm diameter, 2 mW of power and with the same frequency of the MOT1 trapping light, is applied at MOT1 to push the atoms to the science chamber. In this region, the transferred atoms are trapped in another 3D magneto-optical trap (MOT2). Thus, the MOT1 works like an atom source to the MOT2 and the push beam as a funnel that takes the atoms from one region to the other. The MOT1 and push beam alignment is done in a way to maximize the transferred atoms to MOT2.

The MOT2 is more carefully prepared, because the atoms trapped there will be used to produce the BEC. To this, the MOT2 optical part is produced by six independent, orthogonal and counterpropagating beams. This allows us to precisely adjust the alignment, power and polarization of each beam. The MOT2 light has the trapping and repumper light as like in MOT1. The magnetic part is composed by quadrupole coils that generate a magnetic gradient field of around  $20 \text{ G/cm}$ , and compensation coils, that are used to compensate the spurious fields in the trapping region. Figure 5(b) shows the

fluorescence of the trapped atoms in MOT2. It traps around  $2 \times 10^9$  atoms in MOT2, with a temperature similar to the MOT1.

It is required thirty seconds to fully load the MOT2. Then, the atoms are transferred to a conservative trap (in our case, a magnetic trap) where the evaporative cooling is performed. To do this transference in an efficient way, it is necessary to prepare the sample to be trapped in the magnetic trap. All the processes involved will be described in the next section.

### 3.4 Transference to a magnetic trap

The atoms transference from the MOT2 to a magnetic trap (MT) is the most critical process to reach the BEC because, if not well optimized, we can lose a lot of atoms and/or the cloud can be heated. Basically, we can list four reasons for the importance of this process:

(i) *Positions of the trap centers:* In a magnetic trap, the center of the trap is the position of the minimum potential, which should be the same of MOT. However, small misalignments or power imbalance in the MOT light beams can change the MOT center. This condition reduces the transfer efficiency and also heats the atomic cloud.

(ii) *Trap geometries:* The capture volume and geometry of the two traps are very different. (111) The atomic cloud radius is typically 2.5 mm in a MOT and 0.5 mm in a MT. Furthermore, due to the light forces, the MOT shape can be quite irregular while the MT has, approximately, an ellipsoidal shape. For a good transference, it is desired that the sample acquires the magnetic trap shape.

(iii) *Cloud temperature:* The colder is the cloud the smaller it will be. Thus, if we reduce the cloud temperature it will be easier to capture the cloud in the MT.

(iv) *Atomic internal states:* We trap all Zeeman levels of the hyperfine  $5^2S_{1/2}(F =$

2) state in the MOT. However, for  $^{87}\text{Rb}$  only the Zeeman levels  $|F = 2, m_F = 2\rangle$  and  $|F = 2, m_F = 1\rangle$  are magnetically trappable. Thus, we need to prepare the sample in one of those two states before confine the atoms in the MT.

The stages to optimize this transference are called as mode-matching in the literature. In our experiment, we first compress the MOT2, changing the trapping light frequency detuning from  $\Delta = -20$  MHz to  $\Delta = -60$  MHz. This decreases the scattering rate of photons and the atoms will accumulate in the trap center, reducing the cloud size. The duration of this process is 5 ms.

The next step is to cool down the sample. To this, we perform the sub-Doppler cooling technique. The magnetic field is switched-off and the trapping light frequency is shifted more to the red, going to  $\Delta = -70$  MHz. This process lasts 3 ms. After this two stages, the cloud temperature is around  $50 \mu\text{K}$ .

Finally, the last process is to pump the atoms to a magnetically trappable Zeeman state. (109) We optically pump the atoms to the  $|F = 2, m_F = 2\rangle$  state. This process is divided in two stages. First, we perform a pumping to the hyperfine manifold  $F = 2$ , switching off the MOT2 trapping light before the repumper light for 1 ms. Second, we apply a homogeneous magnetic field of the order of 1 G, which splits the Zeeman levels. Simultaneously, in order to accumulate the atoms in the level  $|F = 2, m_F = 2\rangle$ , we optically pump the atoms promoting transition from  $m_F$  to  $m_{F+1}$ . For this, we apply two right-circularly polarized ( $\sigma^+$ ) light pulses. One of them is resonant with the  $5^2S_{1/2}(F = 1) \rightarrow 5^2P_{3/2}(F = 2)$  transition. The other, resonant to the  $5^2S_{1/2}(F = 2) \rightarrow 5^2P_{3/2}(F = 2)$  transition. The pulses duration are  $120 \mu\text{s}$  and  $25 \mu\text{s}$ , respectively. After this processes, the atomic cloud is ready to be magnetically trapped.

## 3.5 The magnetic QUIC trap

After the mode-matching process the atomic cloud is denser and colder, with  $T \approx 50 \mu\text{K}$  and  $4 \times 10^8$  atoms, and the atoms are in the  $|F = 2, m_F = 2\rangle$  magnetically trappable state. Now, all the light is switched off and starts the confinement in a conservative trap (magnetic trap in our case).

In references (109, 112) it can be found the mechanism of magnetic trap. Basically, the magnetic potential ( $V_B$ ) felt by the atoms is proportional to the magnetic field magnitude ( $B$ ), depends on the hyperfine atomic state ( $F$ ) and the Zeeman level ( $m_F$ ):  $V_B = -\mu_B g_F m_F B$ , where  $\mu_B$  is the Bohr magneton and  $g_F$  is the Landé g-factor, for the  $F = 2$  state, the Landé g-factor is  $g_F = 1/2$ .

We catch the atoms in the magnetic trap by turning on abruptly the quadrupole field with a magnetic field gradient of 75 G/cm. Then, we linearly increase the gradient to 330 G/cm during 400 ms. The initial gradient value, that we call catching field, is adjusted to have the higher atom number transferred from the MOT2 to the MT. The compression caused by this gradient ramp heats the cloud. The sample temperature at the end of this process is 250  $\mu\text{K}$ .

It is impossible to reach the BEC in a quadrupolar magnetic trap because the magnetic potential minimum is a point of zero magnetic field. In this region, the atoms can suffer Majorana transitions. (113) This changes the atom state to a non-trappable one, which expels the atom from the trap. To solve this problem some techniques (25, 114–116) were developed. We use a configuration similar to reference (116), in our experiment. We add a coil (Ioffe coil) with the principal axis orthogonal to the quadrupole axis. This quadrupole-Ioffe configuration (QUIC) allows to create a harmonic magnetic trap. Figure 6(a) present a drawing of the QUIC trap.

We transfer the atoms from the quadrupolar magnetic trap to the QUIC trap by slowly increasing the Ioffe coil current from zero to 25.1 A during 600 ms. Figure 6(b) shows the total magnetic field magnitude as a function of the  $x$ -direction, during this

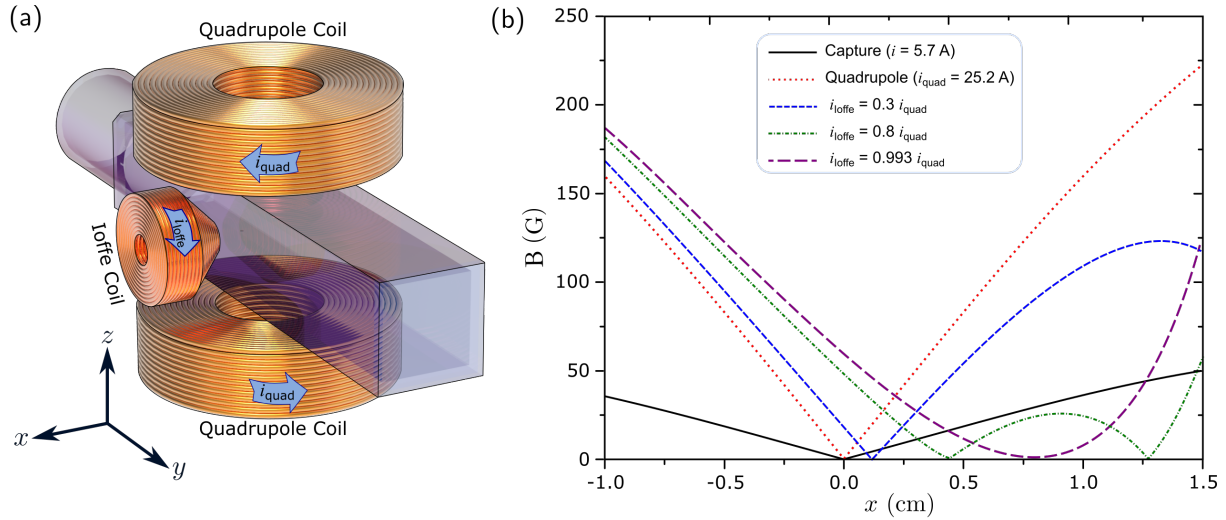


Figure 6 – Quadrupole-Ioffe configuration (QUIC) magnetic trap. (a) Schematic draw of the QUIC trap. (b) Magnetic field magnitude as a function of the  $x$ -direction, for the magnetic capture (black solid line) and during the transference from the MT (red dotted line) to the harmonic QUIC trap (purple long-dashed line).

Source: By the author.

transference. Initially, the magnetic field minimum position moves towards the Ioffe coil and a second minimum appears close to the Ioffe coil. Increasing even more the current, this two minimum get closer. Finally, when the current reaches the final value, the two minimum disappear and a potential with just one non-zero magnetic field is created. At this point, the atoms are displaced 8 mm towards the Ioffe coil and the trap potential, around the magnetic field minimum position, is harmonic:

$$V(x, y, z) = V_0 + \frac{m}{2} (\omega_x^2 x^2 + \omega_y^2 y^2 + \omega_z^2 z^2) , \quad (3.1)$$

where  $V_0$  is the non-zero potential minimum value (which corresponds to a magnetic field of around 1.45 G), named magnetic trap *bias*, and the trap frequencies in our experiment are:  $\omega_x = 2\pi \times 21.1(1)\text{Hz}$ ,  $\omega_y = 2\pi \times 189.3(2)\text{Hz}$  and  $\omega_z = 2\pi \times 187.1(4)\text{Hz}$ . Note that  $\omega_y \approx \omega_z \gg \omega_x$ . Traps with this axial symmetry are called cigar-shaped traps. The radial frequency can be approximated to  $\omega_r = 2\pi \times 188.2(3)\text{Hz}$ , thus the trap aspect ratio is  $\frac{\omega_x}{\omega_r} \approx \frac{1}{9}$ .

In the QUIC trap the cloud has  $2 \times 10^8$  atoms with a temperature around  $300 \mu\text{K}$ . The next stage to reach the quantum degeneracy is a RF-evaporative cooling. However, before describe this process, it is necessary to explain our diagnostic technique by absorption image which is essential to measure the efficiency of all the processes described here,

as well as to observe the Bose-Einstein condensation.

## 3.6 Absorption imaging

The methods to extract information from an atomic cloud are based on the atom-light interaction. (111) In our experiment, we implement the absorption image technique during time-of-flight (TOF). The atoms are released from the trap and imaged in free expansion after a TOF. The absorption image consists in shine the atoms with a probe beam pulse ( $\approx 40 \mu\text{s}$ ) and imaging its corresponding intensity profile. The probe beam is resonant with the  $5^2S_{1/2}(F = 2) \rightarrow 5^2P_{3/2}(F = 3)$  transition. The atomic cloud absorbs part of the light leaving a shadow in the beam. Then, the beam pass through a telescope lens system and the shadow is imaged in a CCD camera (PCO pixelfly qe). This shade is the cloud absorption profile and it is proportional to the atomic density. Two more images are captured by the CCD camera, one containing only the probe beam (without atoms) and the other containing just the background light. As illustrated in Figure 7, we calculate a normalized absorption image by combining these three images:  $\tilde{I}(x, y) = \frac{I_{atoms} - I_{back}}{I_{probe} - I_{back}}$ , where  $I_{atoms}$ ,  $I_{probe}$  and  $I_{back}$  are the beam with atoms, probe beam and background images, respectively.

The light absorption by the cloud can be described by the Beer-Lambert law. The intensity of a beam propagating along  $z$ ,  $I(x, y)$ , through an absorptive medium of density  $n(x, y, z)$ , is written as:

$$I(x, y) = I_0(x, y) e^{-\sigma_0 \tilde{n}(x, y)} \quad , \quad (3.2)$$

where  $I_0(x, y)$  is the initial probe beam intensity,  $\sigma_0$  is the resonant cross section for light absorption (for  $^{87}\text{Rb}$  atoms,  $\sigma_0 \approx 1.36 \times 10^{-9} \text{ cm}^2$ ) and  $\tilde{n}(x, y)$  is the column density of the cloud,

$$\tilde{n}(x, y) = \int n(x, y, z) dz \quad . \quad (3.3)$$

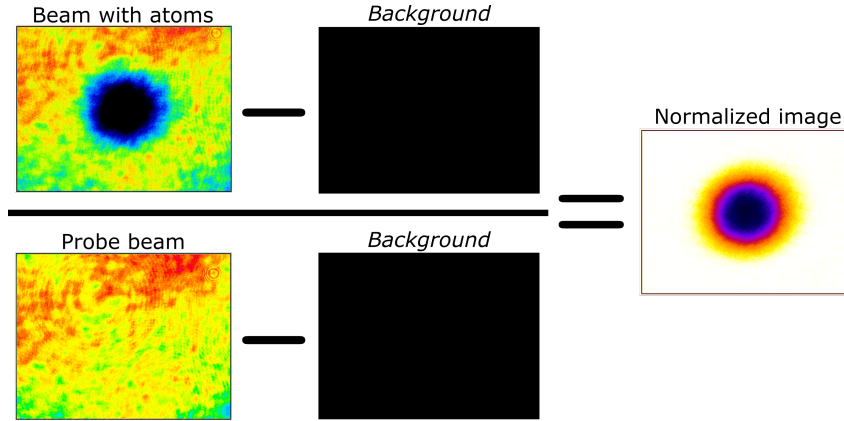


Figure 7 – Image processing to obtain the normalized absorption image,  $\tilde{I}(x, y)$ . We show the image of the probe beam with atoms, the probe beam image and the background image. We subtract the third image from the other and we divide both results, which originate the normalized image.

Source: By the author.

From Equation (3.2), we can define

$$\text{OD}(x, y) = \sigma_0 \tilde{n}(x, y) = -\ln \left( \frac{I(x, y)}{I_0(x, y)} \right), \quad (3.4)$$

the optical density profile of the cloud. Note that  $\frac{I(x, y)}{I_0(x, y)}$  is the normalized absorption image. Thus, the optical density can be evaluated directly from the experimental measurement by the normalized image.

It is possible to extract the cloud dimensions, number of atoms and temperature by fitting the  $\text{OD}(x, y)$  image with the theoretical function for the optical density of the cloud distribution. (111, 117) In what follows, we describe the analysis of a thermal cloud, a condensate cloud and a “bimodal” cloud.

### 3.6.1 Thermal cloud

The velocity distribution of the atoms in a thermal cloud can be described with the classical Maxwell-Boltzmann distribution. Thus, during time-of-flight, the optical density for a thermal cloud is a Gaussian function:

$$\text{OD}_{\text{th}}(x, y) = \text{OD}_{\text{th}}^0 \exp \left[ -\frac{(x - x_0)^2}{2\sigma_x^2} - \frac{(y - y_0)^2}{2\sigma_y^2} \right] \quad (3.5)$$

where,  $\text{OD}_{\text{th}}^0$  is the distribution peak value,  $x_0$  and  $y_0$  are the cloud center-of-mass,  $\sigma_x$  and  $\sigma_y$  are the cloud radii. All these parameters are obtained from the fitting of the experimental image with this Gaussian function.

The number of atoms in the thermal cloud can be calculated from

$$N_{\text{th}} = \int n(x, y, z) dx dy dz = \frac{1}{\sigma_0} \int \text{OD}_{\text{th}}(x, y) dx dy \quad , \quad (3.6)$$

which results in:

$$N_{\text{th}} = 2\pi \frac{\text{OD}_{\text{th}}^0}{\sigma_0} \sigma_x \sigma_y \quad . \quad (3.7)$$

The sample temperature is another important information that can be extracted from the thermal cloud. During time-of-flight,  $t$ , the cloud radii expand ballistically,  $\sigma_i = \sigma_{i0} + v_i t$ , where  $\sigma_{i0}$  is the initial radius in each  $i$ -direction. The expansion velocity is related to the temperature,  $\frac{k_B T_i}{2} = \frac{m v_i^2}{2}$ . For a sufficiently large time-of-flight\* (greater than 10 ms, in our experiment) we can assume that  $\sigma_{i0} \ll \sigma$ . Thus  $\sigma_x \approx \sigma_y \equiv \sigma$ , what results in a temperature:

$$T = \frac{m}{k_B} \left( \frac{\sigma}{t} \right)^2 \quad . \quad (3.8)$$

### 3.6.2 Condensate cloud

As discussed in Section 2.2.1, the density distribution of a pure BEC cloud inside a harmonic potential has a parabolic profile, in the Thomas-Fermi limit. Even after expansion, the cloud is still described by this profile. (118) Thus, the optical density for a pure BEC cloud is an integration of this density distribution along the probe direction, which results in the 2D Thomas-Fermi (TF) function,

$$\text{OD}_{\text{TF}}(x, y) = \text{OD}_{\text{TF}}^0 \max \left\{ \left[ 1 - \frac{(x - x_0)^2}{R_x^2} - \frac{(y - y_0)^2}{R_y^2} \right]^{3/2}, 0 \right\} \quad , \quad (3.9)$$

---

\* For a gas initially trapped in a harmonic trap with frequencies  $\omega_i$  this happens when  $t \gg \frac{1}{\omega_i}$ ,  $\forall i$ .

where  $\text{OD}_{\text{TF}}^0$  is the distribution peak value,  $x_0$  and  $y_0$  are the cloud center-of-mass,  $R_x$  and  $R_y$  are the BEC radii. All these parameters are obtained from the fitting of the experimental image with this TF function.

Similarly to Equation (3.6), the number of atoms in the BEC is obtained by:

$$N_0 = \frac{2\pi}{5} \frac{\text{OD}_{\text{TF}}^0}{\sigma_0} R_x R_y . \quad (3.10)$$

### 3.6.3 Bimodal cloud

Below the critical temperature, the atomic cloud has two components, the normal cloud (thermal atoms) and the quantum cloud (BEC atoms), this is the reason to call as “bimodal” cloud. The optical density of a this cloud can be written with a bimodal function,

$$\text{OD}(x, y) = \text{OD}_{\text{th}}(x, y) + \text{OD}_{\text{TF}}(x, y) , \quad (3.11)$$

where  $\text{OD}_{\text{th}}(x, y)$  and  $\text{OD}_{\text{TF}}(x, y)$  are defined by Equations (3.5) and (3.9).

The thermal cloud temperature can be evaluated from Equation (3.8) and the total number of atoms in the cloud is calculate from:

$$N = N_{\text{th}} + N_0 = 2\pi \frac{\text{OD}_{\text{th}}^0}{\sigma_0} \sigma_x \sigma_y + \frac{2\pi}{5} \frac{\text{OD}_{\text{TF}}^0}{\sigma_0} R_x R_y . \quad (3.12)$$

The processes involved in the condensate production, described in previous sections, was optimized by evaluating the number of atoms, the cloud temperature and the cloud size. In the following section we will describe the evaporative cooling process. A runaway evaporation, where the decrease in temperature results in an increase of the phase-space density and the elastic collision rate, leads to the Bose-Einstein condensation.

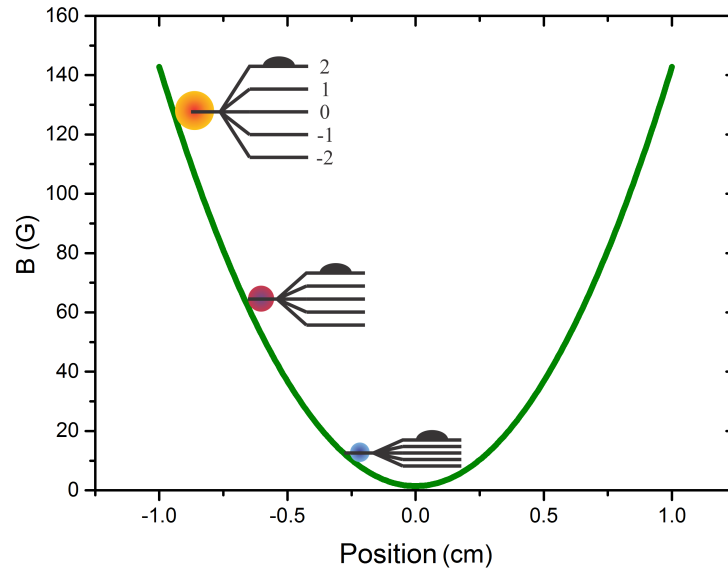


Figure 8 – Illustration of the Zeeman level shifts for different magnetic field value inside the QUIC trap. The high energy atoms reach higher magnetic field values, thus the Zeeman level shifts are greater than the less energetic atoms.

Source: By the author.

### 3.7 Evaporative cooling and the BEC

The evaporative cooling is done by selectively removing the hottest atoms of the atomic velocity distribution, at a given temperature  $T$ , and letting the cloud rethermalize at a lower temperature. Performing the evaporative cooling in a continuous way allow to reach colder samples (23, 119) and it is fundamental to produce condensate clouds. Evaporative cooling of trapped atoms was developed as a technique to cool hydrogen. (53, 120, 121) Here, we briefly summarize the basic aspects of evaporative cooling of magnetically trapped atoms using radio frequency (RF) radiation, for more details please see (23, 122) reviews.

In magnetic traps, we can perform a RF-forced evaporative cooling. In this process, the Zeeman levels energy dependence with the magnetic field allow to remove selectively the atoms. The high energy atoms (hottest atoms) will reach higher magnetic fields in the trapping potential, as a consequence, the energy shift between the  $m_F$  and  $m_{F\pm 1}$  level is greater than the less energetic atoms (coldest ones). Figure 8 shows an illustration of the Zeeman levels shifts for different magnetic field values, in the harmonic potential.

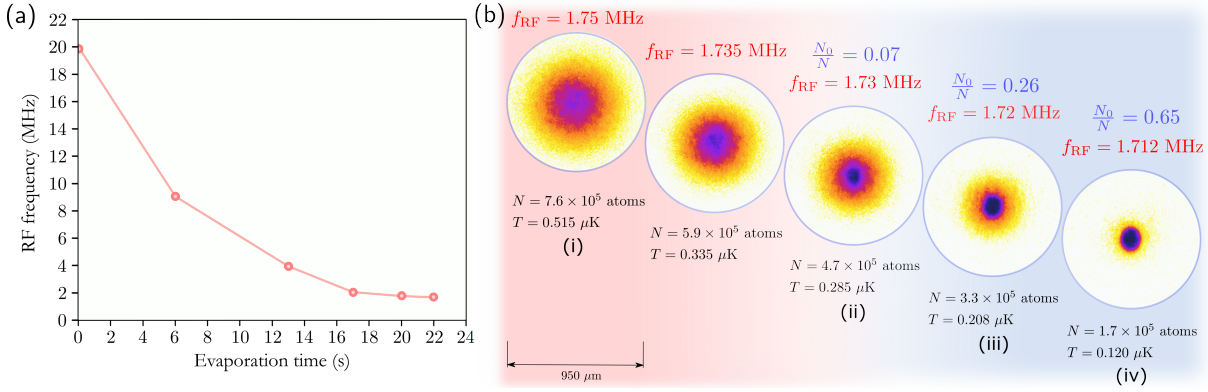


Figure 9 – RF-forced evaporative cooling. (a) RF ramp used to produce a BEC, it is composed by 5 linear ramps delimited by the circles. (b) Normalized absorption image of the cloud for different points of the RF ramp, showing the atoms number, the cloud temperature and, after the BEC transition, the condensation atoms fraction ( $N_0/N$ ). Source: By the author.

The RF radiation with an initially large frequency induces  $m_F \rightarrow m_{F-1}$  transitions in the higher energetic atoms, transferring them to a non-trappable state, which removes them from the trap. The remaining cloud will thermalize at a lower temperature. Then, the atoms reach a magnetic field value lower than before. Now, to remove the hottest atoms in that colder cloud, the radio-frequency should have lower energy. Decreasing the RF-frequency, continuously, in a rate following the cloud thermalization, we get a colder and denser cloud. Figure 9(a) shows the radio-frequency ramp in our experiment.

We evaluate the phase-space density (PSD) and the elastic collision rate ( $\gamma_{el}$ ) to optimize the evaporative cooling process. The phase-space density is  $\text{PSD} = n\lambda_{dB}^3$ , where  $n$  is the atomic density and  $\lambda_{dB}$  is the thermal de Broglie wavelength. The elastic collision rate is  $\gamma_{el} = n\sigma_{el}\bar{v}$ , where  $\sigma_{el}$  is the elastic collision cross section and  $\bar{v}$  is the average thermal velocity. In a harmonic potential:  $\text{PSD} \propto \frac{N}{T^3}$ ,  $n \propto \frac{N}{T^{-3/2}}$  and  $\bar{v} \propto T^{1/2}$ . (61) In order to better optimize the evaporative cooling process, we divide the RF ramp in several linear ramps, as shown in Figure 9(a). With this we are able to control the initial and final frequencies value, besides the frequency scan rate during each ramp.

To reach quantum degeneracy, the phase-space density has to be greater than or equal to 2.612. (58) Thus, a run-away evaporative cooling allows us to keep constant or increase the collision rate between the atoms and increase the phase-space density until the Bose-Einstein condensation is obtained. Figure 9(b) presents absorption images of

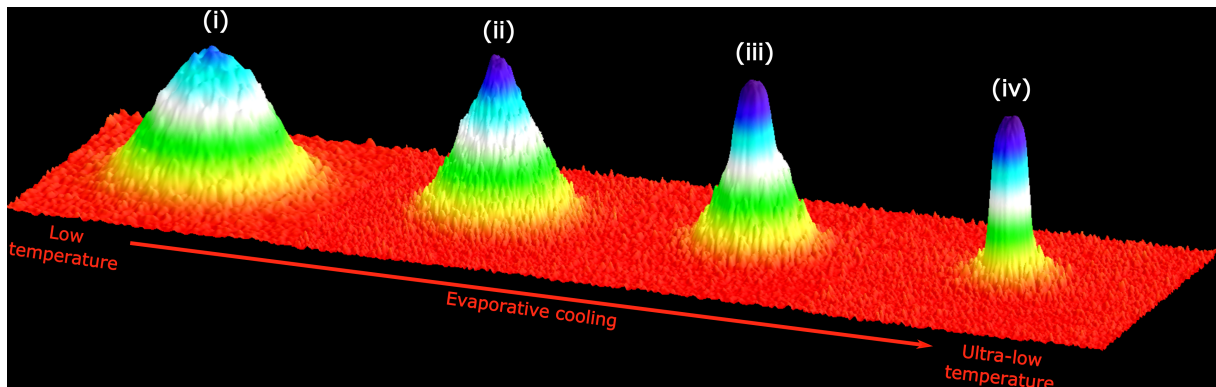


Figure 10 – Absorption image profiles during the BEC transition. The numeric index above each cloud correspond to the marked images from Figure 9(b).

Source: By the author.

the atomic cloud for different points in the RF ramp, showing the atom number and temperature of the cloud crossing the condensation critical point at  $T_c \approx 290$  nK, in our experiment.

Figure 10 shows absorption image profiles of the cloud for different temperatures. At higher temperatures, when the sample is completely thermal (i), its density profile is a Gaussian curve. Decreasing the temperature below the critical point (ii)-(iv), we observe a parabolic peak surrounded by a Gaussian profile. The parabolic peak corresponds to the condensed component while the Gaussian are the thermal atoms. This distribution is known as bimodal distribution, as explained in Section 3.6.

## 3.8 Excitation system

One research interest in our experiment is to analyze the effects caused by an external perturbation in a Bose-Einstein condensate. In particular, we investigate the mechanism of transferring angular momentum to the BEC, producing vortices and routes for the generation of quantum turbulence. (33) In our experiment, the excitation is produced by superimposing an oscillatory magnetic field with the trapping potential. A simulation of the effect caused by these coils can be found in reference (31) and it has been shown that

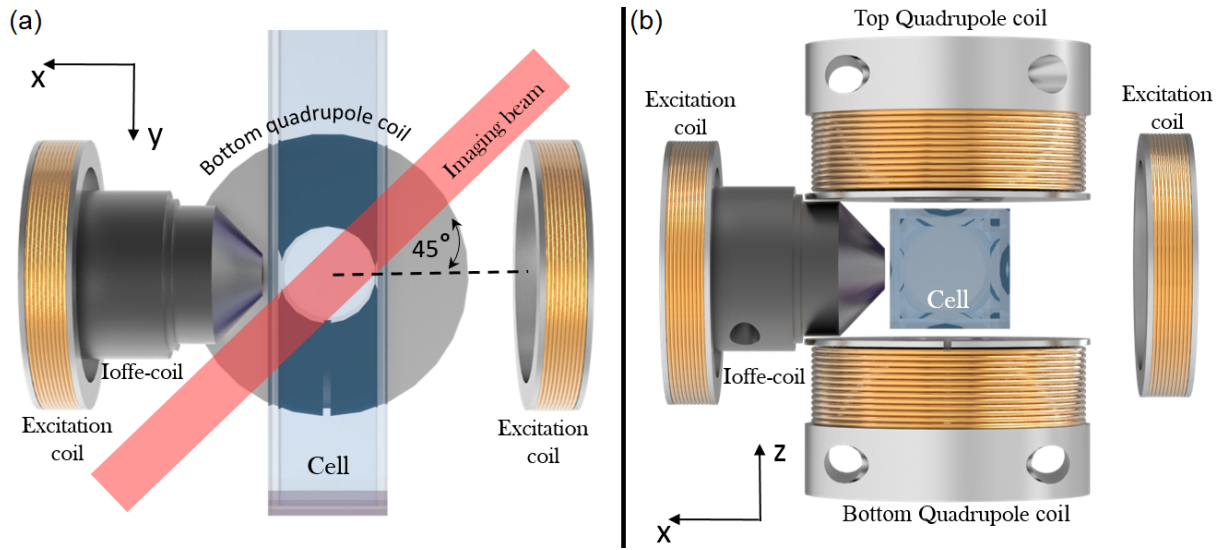


Figure 11 – Schematic drawing of the excitation system in the (a) *xy* plane and (b) *xz* plane.  
 Source: By the author.

this excitation produces a combination of translation, rotation and spatial deformation of the trapping potential.

The oscillating magnetic field is generated by a pair of coils in anti-Helmholtz configuration. We apply to the coil an ac-current  $I = I_0[1 - \cos(2\pi f_{exc} t_{exc})]$ , where  $f_{exc}$  is the excitation frequency,  $I_0$  is maximum excitation current and  $t_{exc}$  is the time interval in which the perturbing magnetic field is turned on (excitation time). One of these excitation coils is fixed close to the Ioffe coil, the other we can move in all spatial directions. Figure 11 shows an schematic drawing of the excitation system.

We perform the BEC perturbation in this way: as soon as the evaporative cooling ends and with the BEC still inside the QUIC trap, we turn on the oscillatory magnetic field. After the excitation time, only the perturbing field is turned off and the condensate is let free to move within the harmonic potential, during a period that we call hold time. Finally, we turn off the harmonic trap, the cloud expands in time-of-flight and we obtain the image of the cloud, as described in Section 3.6. With this procedure, the parameters that we can vary to investigate the perturbation effect in the condensate are: the spatial configuration of the coils, the excitation frequency, the amplitude of excitation (controlled by the maximum excitation current,  $I_0$ ), the excitation time, and the hold time.

Previous studies in our laboratory have shown that it is possible to induce collective

---

excitations (99), produce quantized vortices (31) and quantum turbulence (33) in the BEC with the excitation system described here. In those works, the excitation parameters (spatial configuration of the excitation coils, frequency and hold time) were fixed. In this thesis, we varied the excitation coils position to have a better perturbation in the BEC and we changed the excitation parameters to study the excitations generated in the condensate.



# 4 Excitation of collective modes by an oscillatory perturbation

In this chapter we describe results related to the perturbation of a Bose-Einstein condensate with an oscillatory magnetic field. These results are related to the experimental observation of collective modes that are excited in the BEC. We observed a non-linear behavior to efficiently excite the quadrupole mode, indicating the necessity of a minimum energy to couple this mode in the cloud.

## 4.1 Setting the excitation system

Using the excitation system described in Section 3.8, we were able to excite collective modes of the BEC. The first step was to adjust the relative position of the excitation coils. Then, we applied an ac-current, with fixed amplitude 1.2 A and frequency 189 Hz for 31.8 ms of excitation time, which corresponds to 6 periods of excitation. The oscillating current was turned off and the cloud was allowed to evolve in the harmonic trap during a hold time of 30 ms. The trap was switched off, leaving the cloud to expand freely for 20 ms. We observed the condensate by performing a standard absorption image with a weak probe beam in a CCD camera.

From that, we started to adjust the coils position. Depending on their relative position, the cloud was observed at different places in the image. To optimize the position of the excitation coils, we watched the position of the excited BEC center-of-mass (CM) relative to the non-excited one. The coils position was adjusted in order to create the largest displacement of the CM. After this procedure, the final configuration of the coils is shown in Figure 12.

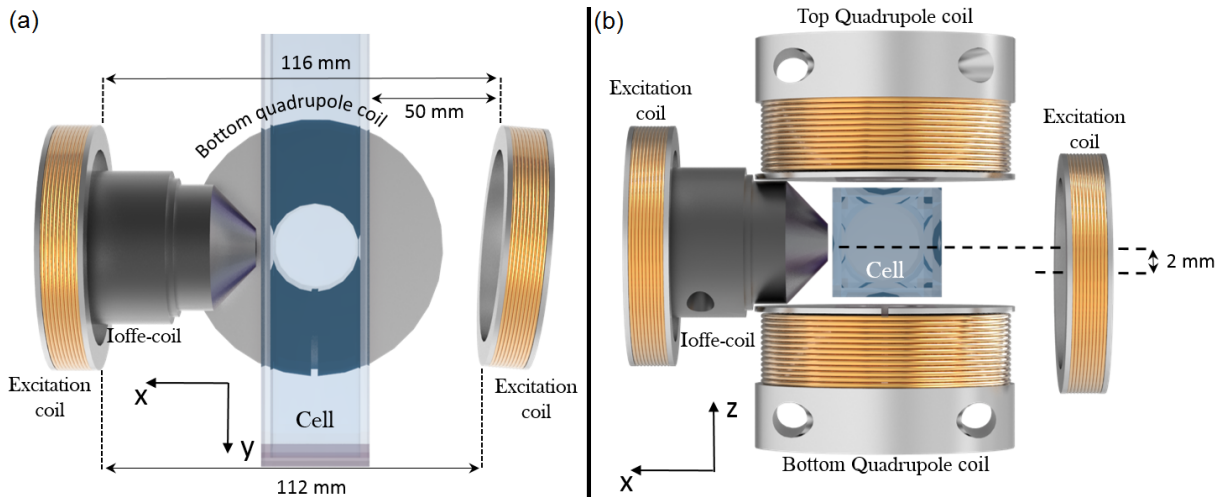


Figure 12 – Schematic drawing of the excitation coils setup used to study the collective modes. (a)  $xy$  plane and (b)  $xz$  plane.

Source: By the author.

For this configuration, the relation to convert current in magnetic field gradient is, approximately,  $420 \frac{\text{mG}}{\text{cm}\cdot\text{A}}$ . The perturbation of this excitation field in the trapped BEC can be expressed in terms of the chemical potential,  $\mu$ . In our system,  $\mu \approx 100 \text{ nK}$  and the perturbation field is around of  $100\mu/\text{A}$ .

## 4.2 Setting the excitation frequency

The excitation coils position were locked in place, as described in Section 4.1. To set the excitation frequency, we investigated the dependency of the center-of-mass dislocation as the oscillatory excitation evolves, for three different excitation frequency.

We fixed the excitation amplitude at  $315 \text{ mG/cm}$  and the perturbation field is applied during an excitation time. The Fig. 13 shows the dependence of the center-of-mass position as a function of the excitation time, for three excitation frequencies. For a fixed frequency, the system answer like a driven harmonic oscillator as the perturbation field is turned on. It is remarkable that for frequencies close to the radial trap frequency ( $f_r \approx 189 \text{ Hz}$ ) the system is resonant and the CM displacement is maximum, as shown in Fig. 13 (b). This is the reason that we choose a fixed excitation frequency at  $189 \text{ Hz}$  to

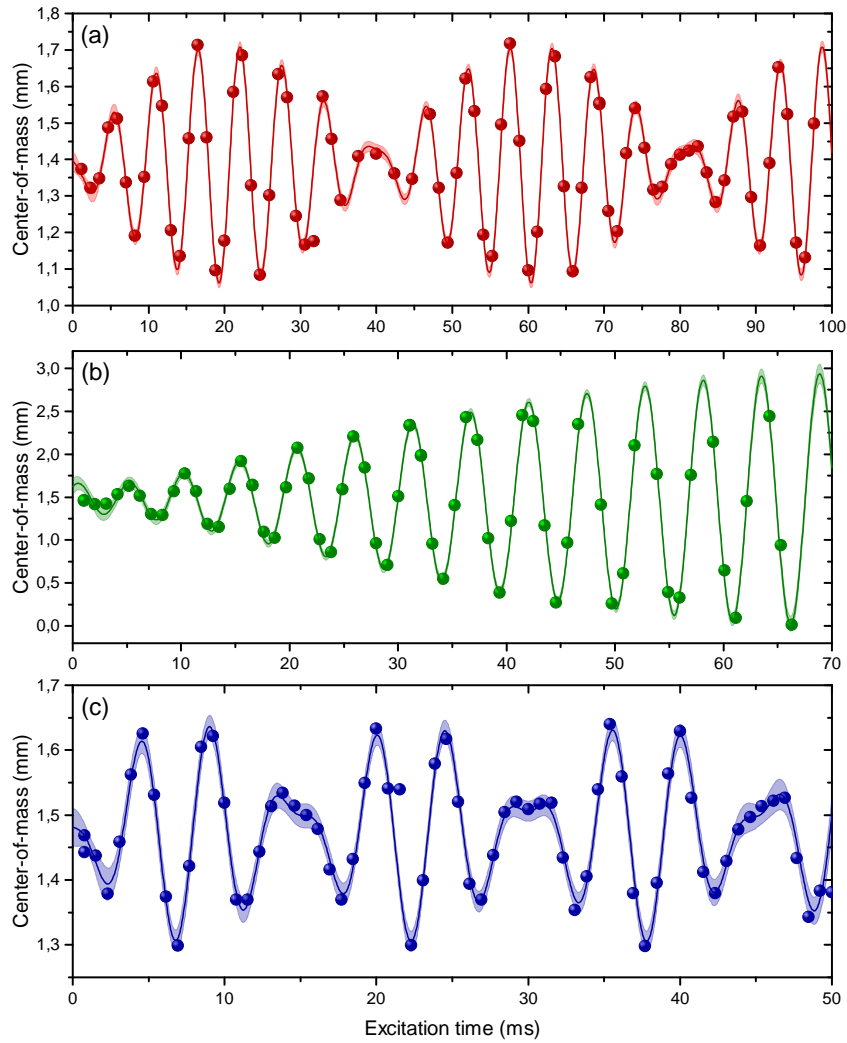


Figure 13 – Driven oscillations. Center-of-mass position as a function of the excitation time for three excitation frequencies: (a)  $f_{\text{exc}} = 170$  Hz, (b)  $f_{\text{exc}} = 194$  Hz and (c)  $f_{\text{exc}} = 260$  Hz.

Source: By the author.

perform the following experiments.

### 4.3 Observation of collective modes

After the procedures described in Sections 4.1 and 4.2, we started to investigate the effects induced by an oscillatory magnetic field in a trapped BEC. To perform this experiment, we started with a BEC containing about  $N_0 = 1.8(1) \times 10^5$  atoms with  $\frac{N_0}{N} = 0.70(5)$  of condensate fraction. In order to excite the trapped BEC, a sinusoidal

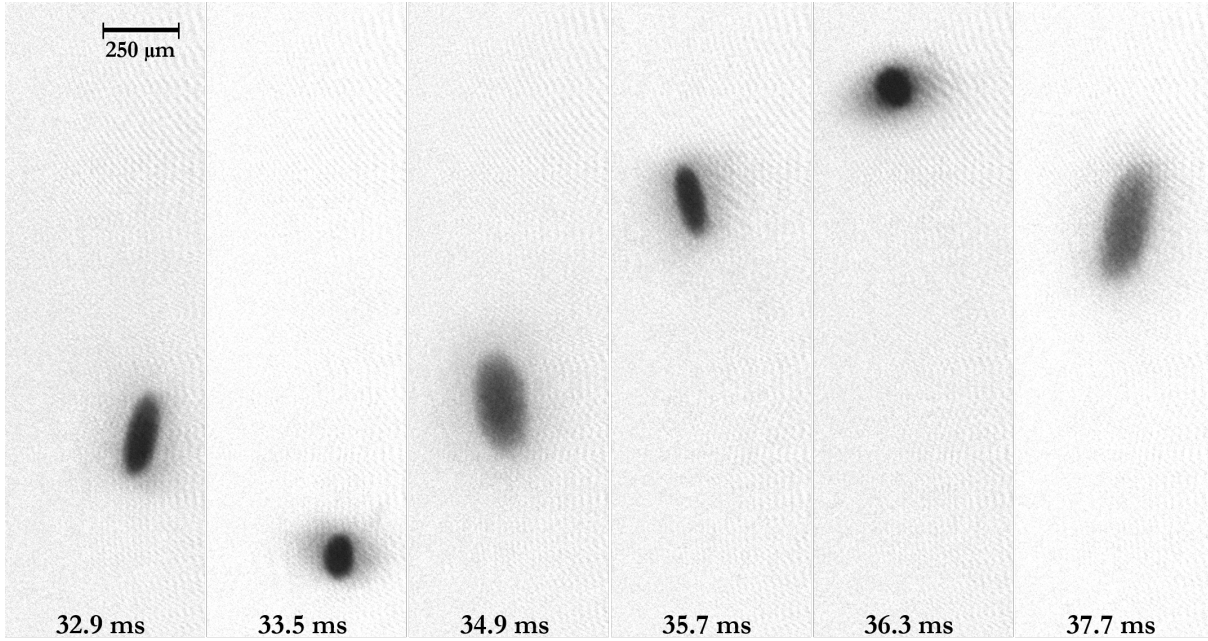


Figure 14 – Typical images acquired during the experimental runs. Normalized absorption images of the excited BEC evolving in-trap, after certain hold time (shown on the bottom of each image). The excitation amplitude was about 470 mG/cm and the images were taken after 20 ms time-of-flight. It is noticeable a movement of the cloud center-of-mass and a variation on the condensate shape as the hold time is increased.

Source: By the author.

magnetic field gradient is turned on and superimposed on the atoms right after the BEC is produced. The magnetic field gradient oscillates from zero to a maximum value, which we named as “excitation amplitude”. In this experiment, we scanned the excitation amplitude from 75 mG/cm to 790 mG/cm. For a fixed excitation amplitude, the extra magnetic field oscillates with a frequency of 189 Hz during 6 full cycles and then it is switched off. The cloud was held trapped during a hold time,  $t_{\text{hold}}$ , which varied from 30 ms to 50 ms. Finally, the magnetic trap was switched off and the excited BEC was imaged after 20 ms of TOF. In Figure 14, we present a sequence of typical BEC images produced by exciting the condensate with about 470 mG/cm, for six different hold times.

As we can see in Figure 14, the cloud’s center-of-mass and its shape oscillates as the hold time is changed. This characterizes the dipolar and the quadrupolar collective modes of the condensate, respectively. In the following section, we will present a quantitative analysis of these modes.

## 4.4 Results and discussions

To study the low-lying collective excitations (dipolar and quadrupolar), we followed the center-of-mass motion and the BEC shape, as a function of the hold time. In order to quantify the condensate shape, we evaluate the aspect ratio,  $AR = \frac{r_y}{r_x}$ , where  $r_y$  and  $r_x$  are the BEC radius in  $y$  and  $x$  direction, respectively. The condensate CM position and the BEC radii are determined from the image files, which are fitted by a bimodal function, as explained in Section 3.6.

The dipolar and quadrupolar mode analysis are shown in Figure 15, for four different excitation amplitudes. In Figure 15(a), the center-of-mass oscillation is presented, corresponding to the condensate dipolar mode. Note that the energy pumped by the excitation not only increases the amplitude of the dipolar mode, but also shifts the phase of the sinusoidal CM motion. The phase originates from the initial position where the cloud is left in the trap, after the excitation field was switched off.

The  $AR$  evolution in hold time is shown in Figure 15(b). One can see that the  $AR$  oscillates as a function of the hold time, which corresponds to one of the quadrupolar modes. We note that the amplitude and phase of this oscillation increase with the excitation amplitude.

We measure the cloud heating during these oscillations by calculating the condensate fraction ( $N_0/N$ ) during the hold time evolution. This result is presented in Figure 16. Comparing the BEC fraction for the non-excited and the perturbed BEC, we conclude that the excitation field produces a heating of about only 20% of the non-perturbed BEC. Moreover, during the hold time evolution, the BEC fraction reduces equally for both cases, showing that the observed small heating is caused by trap losses and it is not an effect related to the excited BEC.

The data presented in Figure 15 were fitted using sinusoidal functions from where we obtained the amplitude and the frequency of the observed collective modes, for each excitation amplitude. We plotted these results, as shown in Figure 17, as a function of

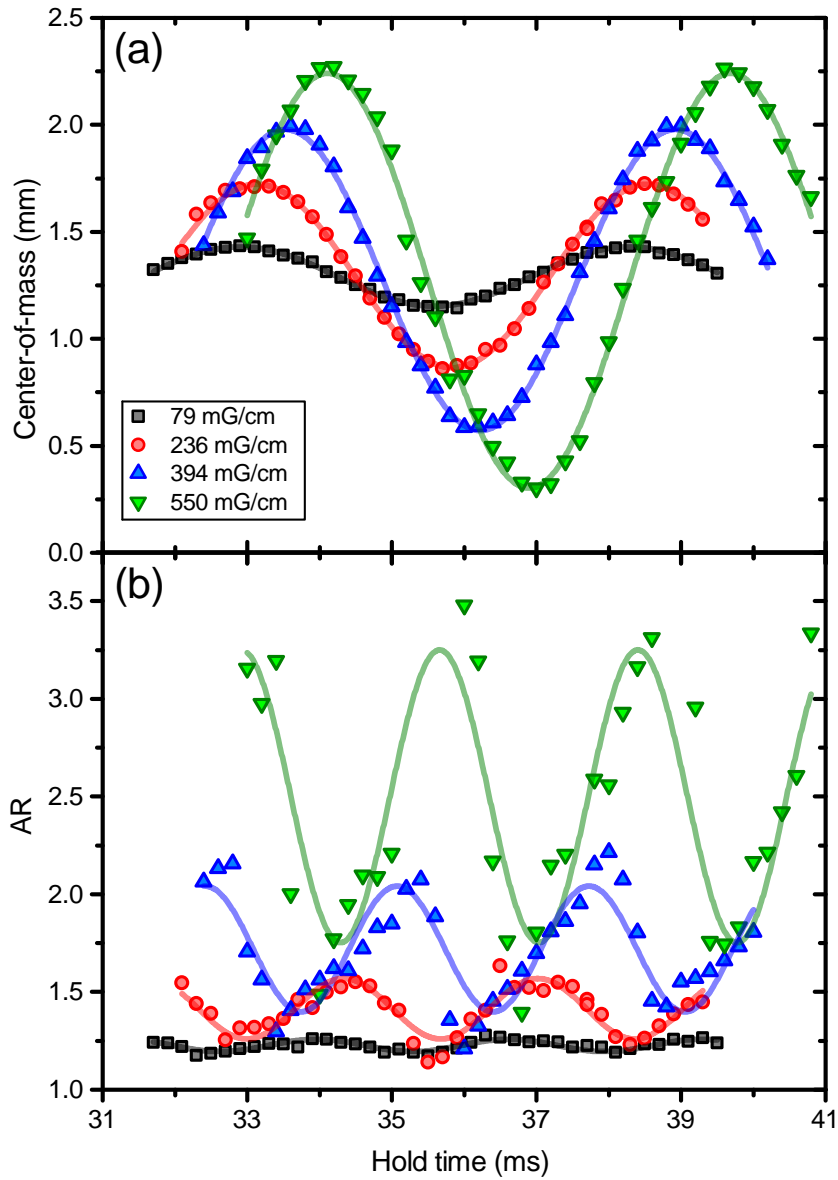


Figure 15 – Low-lying collective excitation modes. (a) The center-of-mass and (b) the  $AR$  as a function of the hold time, for 4 different excitation amplitudes, corresponding to the dipolar mode and the quadrupolar mode, respectively.

Source: Adapted from FRITSCH. (123)

the excitation amplitude.

The dipolar and quadrupolar mode frequencies as a function of the excitation amplitude are presented in Figure 17(a). The measured collective modes frequencies are  $f_d = 185(3)$  Hz for the dipolar mode, and  $f_q = 375(8)$  Hz for the quadrupolar mode. We can see that the dipolar mode frequency matches the radial trap frequency,  $\frac{\omega_r}{2\pi}$ , and the quadrupolar frequency is approximately  $2 \cdot \left(\frac{\omega_r}{2\pi}\right)$ , which corresponds to the  $m = 0$  fast quadrupolar mode (also called breathing mode). These frequencies are in good agreement

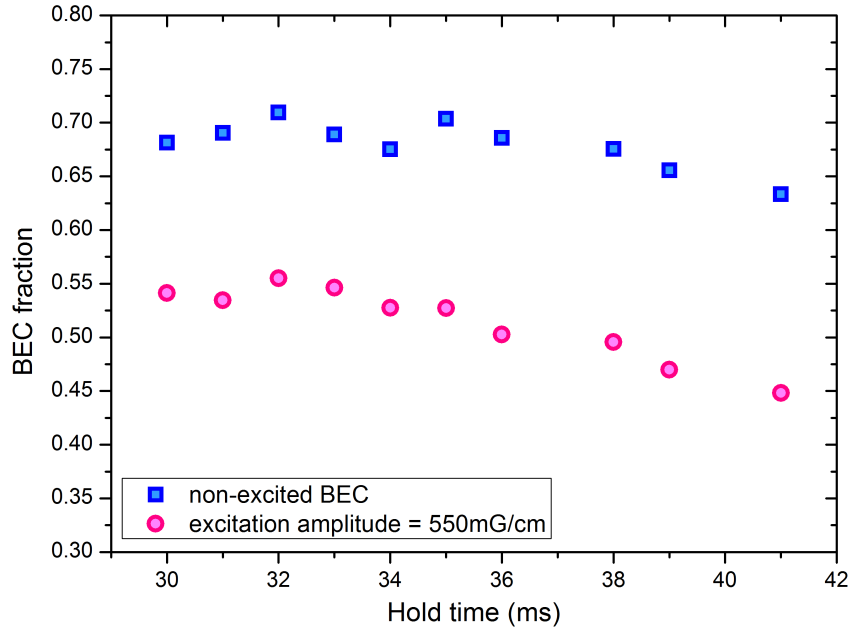


Figure 16 – BEC fraction ( $N_0/N$ ) as a function of hold time for a equilibrium BEC (blue squares) and a perturbed BEC (magenta circles) with excitation amplitude 550 mG/cm.

Source: By the author.

with the theoretical prediction presented and discussed in Section 2.3. For excitation amplitudes lower than 400 mG/cm these measured frequencies remain mostly constant with just a slight decrease (2–3%) for larger amplitudes. Similar observations about the collective modes frequency shifts were seen before. (115,124) For nearly pure condensates, the thermal excitations does not affect the condensate excitation spectrum. (124)

The center-of-mass and  $AR$  oscillation amplitude dependency with the excitation amplitude are shown in Figure 17(b). The dipolar mode is easily excited even for low excitation amplitudes. The CM oscillation amplitude proportionally increases with the excitation amplitude. On the other hand, the  $AR$  oscillation amplitude presents an interesting non-linear behavior for excitation amplitudes lower than 400 mG/cm, starting from zero, and having a large linear increase for higher amplitudes. This observation suggests that there may be a minimal energy to efficiently switch the quadrupolar mode on. We do not have yet a theoretical explanation for this observation, and new experiments (and studies) are needed to fully understand this phenomenon.

By observing the dipolar results shown in Figure 17(b), we conclude that the condensate is pushed farther away from the trap bottom, as the perturbation amplitude

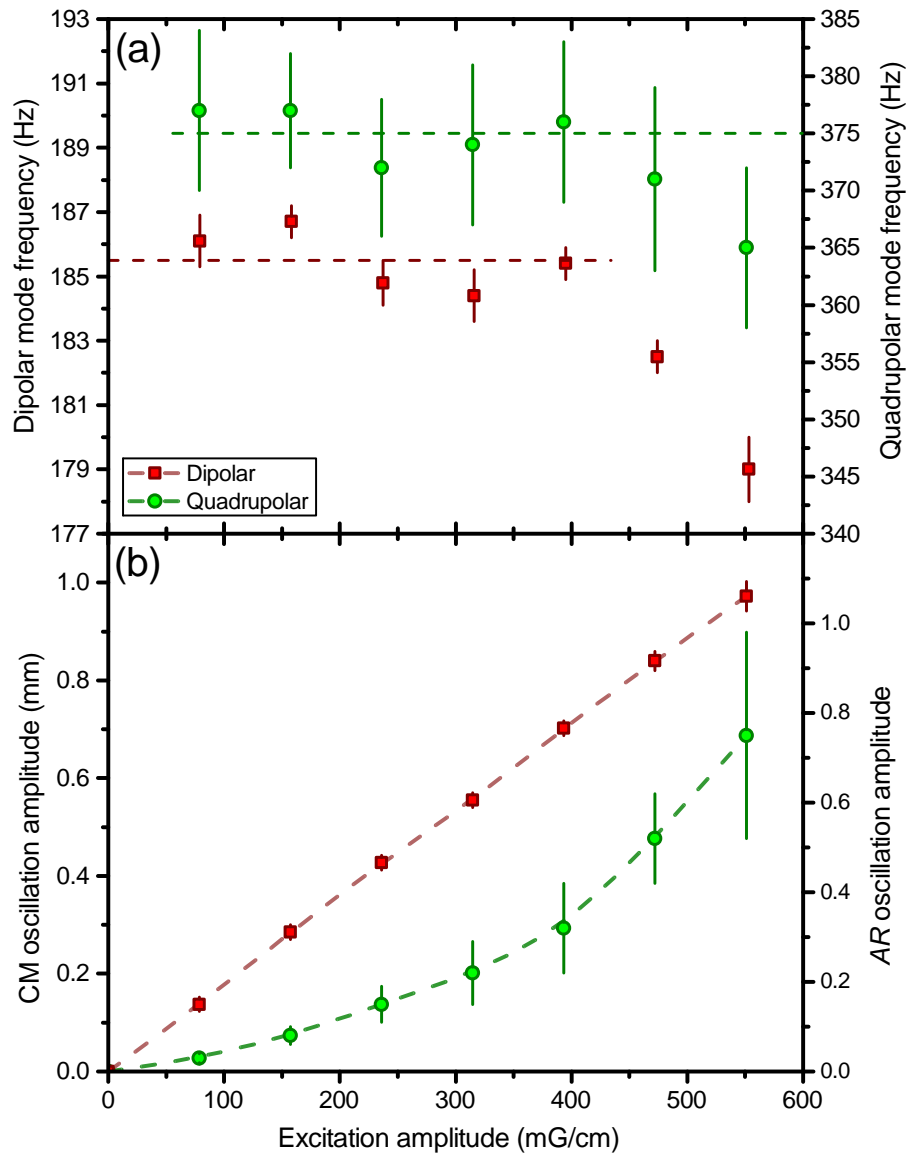


Figure 17 – Collective modes frequency and amplitude dependency with the excitation amplitude. (a) Dipolar and quadrupolar mode frequencies versus the perturbing amplitude. (b) Condensate CM and *AR* oscillation amplitude as a function of the excitation amplitude.

Source: Adapted from FRITSCH. (123)

increases. In a QUIC trap, being far from the trap bottom, means that the BEC reaches the anharmonic region. These outer trap regions present much steeper gradient field and curvature, which compress the cloud, than are more favorable to produce shape oscillations observed in the BEC. In other words, as the cloud travels far from the trap bottom (i.e. with higher dipolar oscillation) the quadrupolar mode is more likely excited. This is consistent with the observation of a change in the curvature shown in Figure 17(b) for the quadrupolar mode. Beyond that, we believe that the steep gradient regions might be

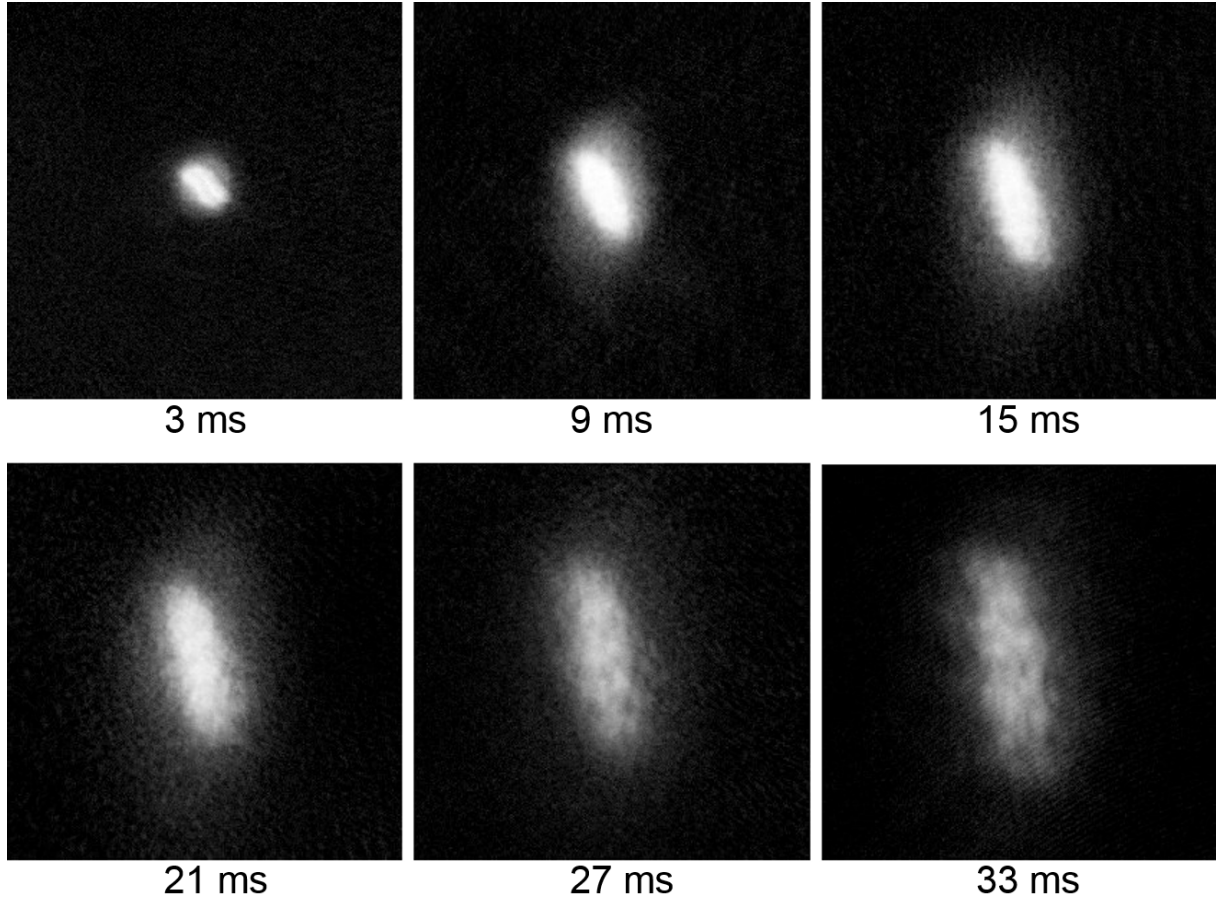


Figure 18 – Image sequence of excited cloud for different time-of-flights (shown below of each image). The excitation amplitude and hold time was fixed in 550 mG/cm and 20 ms, respectively.

Source: By the author.

inducing the dephasing observed in Figure 15. This complex coupling dynamics seems to be particular to our excitation system. It may also be the key to the better understand of the vortex nucleation and the turbulence emergence observed in previous experiments. (33, 34, 125)

It is important to present a final important observation. For amplitudes larger than 400 mG/cm the perturbed condensate exhibits topological defects. To better visualize such defects, we take images of excited clouds for different time-of-flight. A typical TOF sequence is presented in Figure 18, where we fixed the hold time and the excitation amplitude to 20 ms and 550 mG/cm, respectively.

We investigate the aspect ratio (A.R.) evolution during the time-of-flight for different excitation amplitudes and hold time. Figure 19 present the results for the non-excited BEC and three excitation amplitudes: 79 mG/cm, 314 mG/cm and 550 mG/cm. For the

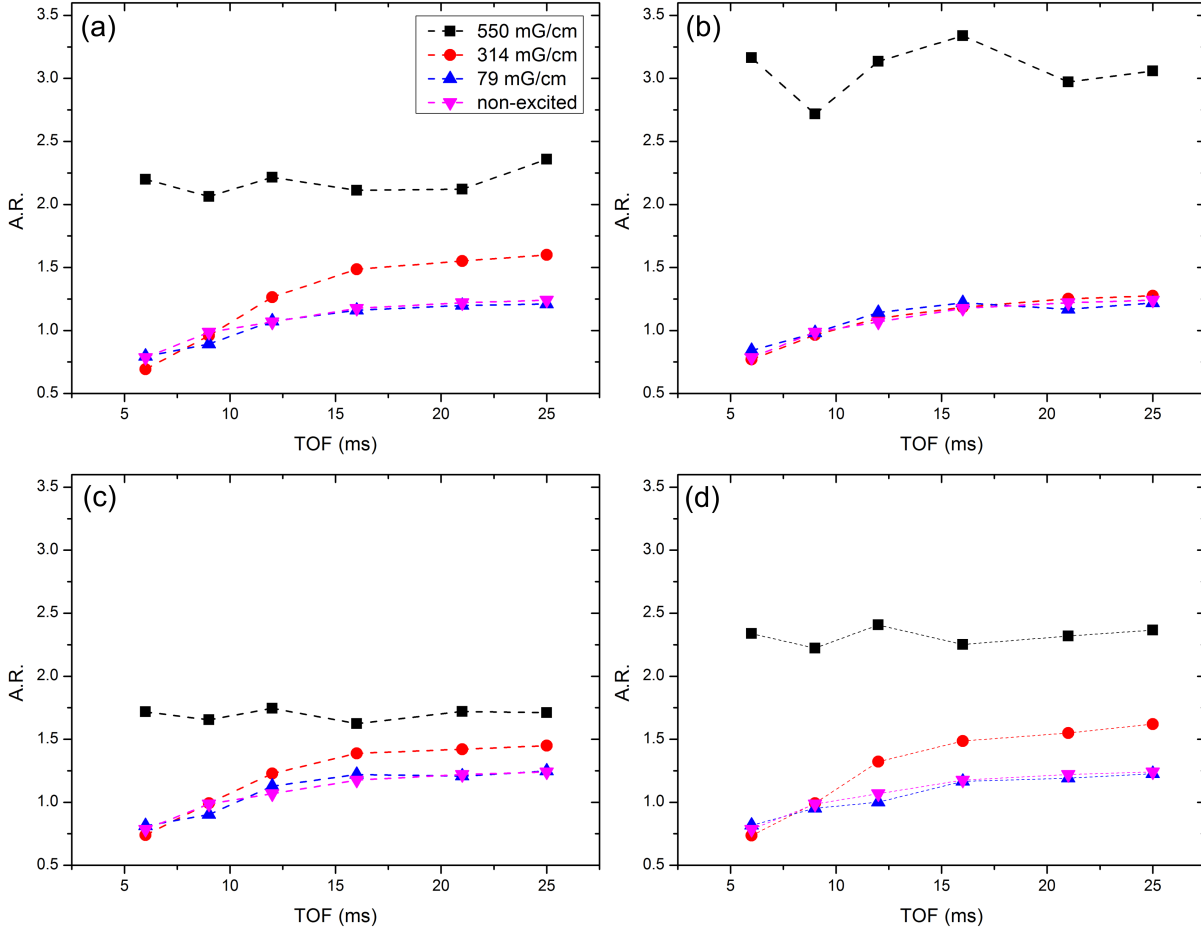


Figure 19 – Aspect ratio (A.R.) evolution during time-of-flight expansion for different excitation amplitudes. Each panel corresponds to a specific hold time: (a) 32 ms, (b) 33 ms, (c) 34 ms and (d) 35 ms.

Source: By the author.

non-perturbed BEC and for a BEC excited with low amplitude, we observed the typical aspect ratio inversion curves during TOF expansion. However, for higher amplitudes the aspect ratio is constant during time-of-flight. Moreover, the Figures 19(a)-(d) are taken for different hold time (respectively 32 ms, 33 ms, 34 ms and 35 ms) showing that the observed behavior does not depend on the hold time, which means that it is not related to the collective mode oscillation.

We can make two observations about the TOF sequence presented in Figure 18 and the results in Figure 19:

(i) For time-of-flight longer than 25 ms we can better see topological defects in the condensate, which suggests the existence of vortices or a turbulent state in some cases.

(ii) This TOF expansion shows the aspect ratio non-inversion, an observed char-

acteristic of turbulent BEC clouds. (33)

Motivated by these observations, we decided to study this turbulent regime. For this purpose, we want to investigate the energy spectrum of this cloud. However, it is difficult to obtain, directly, this spectrum from time-of-flight measurements. A possible alternative is to measure the cloud momentum distribution after an expansion in time-of-flight (57,100), which is related to the energy distribution of the cloud. In the next chapter, we will describe the analysis of the momentum distribution of the excited BECs.



# 5 Momentum distribution of a perturbed BEC

In this chapter, the momentum distribution of a perturbed BEC is investigated as a function of the excitation parameters (i.e. hold time and excitation amplitude). We show a coupling between the momentum distribution curves and the quadrupolar collective mode. This effect might be a more prosaic explanation for the apparent discrepancy in Kolmogorov's power law observed in (57) a previous work. The results presented here also were part of a master thesis. (126)

## 5.1 Introduction

Turbulence can be characterized by a very specific momentum distribution with a well defined power-law behavior, known as the Kolmogorov scaling law (127), Equation (2.41). This behavior has been seen in classical turbulence (79), quantum turbulence in superfluid liquid Helium (128) and predicted to take place in quantum turbulence in atomic superfluids. (97) The emergence of Quantum Turbulence (33) in a  $^{87}\text{Rb}$  Bose-condensed sample has immediately raised the question on how to obtain the momentum distribution to investigate the similarities and differences with other turbulent systems, either classical or quantum.

In a previous work (57), where the momentum distribution of turbulent clouds was analyzed, they have observed a power law in the momentum distribution with an exponent that did not match the one expected from a Kolmogorov power law,  $-5/3$ , but is on the order of  $-3$ . In that work, they did not do any analysis changing the excitation parameters, like the hold time and excitation amplitude.

## 5.2 Methodology to compute the momentum distribution from an expanded cloud

We use a procedure similar to previous works (57, 100) to compute the cloud's momentum distribution. In this section, we present this procedure.

An initial consideration is about the free expansion of a regular BEC (without vortex) and a BEC with vortices (or in a turbulent regime). After long time-of-flight (TOF  $> 10$  ms), it was shown (57, 100, 129) that the kinetic energy predominates over the interaction energy and rotational energy (from the vortices). This results that the atoms position will be approximated by

$$\mathbf{r}(t) = \frac{\hbar t}{m} \mathbf{k} \quad , \quad (5.1)$$

where  $t$  is the TOF,  $m$  is the atomic mass and  $\mathbf{k}$  is the *in situ* atomic momentum. This means that the atomic density distribution,  $n(\mathbf{r})$ , after a long free expansion, can be used to map its *in situ* momentum distribution,  $n(\mathbf{k})$ .

Experimentally, we obtain the atomic density distribution from an absorption image in TOF. This image is an integrated column density in the probe direction, which gives a 2D density profile,  $n(x, y)$ . Therefore, we can compute a 2D momentum distribution,  $n'(|k'| = k')$ .

From the absorption image of an expanded cloud, represented in Figure 20, we can define a function  $G(r')$  as the number of atoms in a region between  $r'$  and  $r' + \delta r'$ , represented by the dark area of Figure 20, where  $r'^2 = x'^2 + y'^2$ . The function  $G(r')$  is the integral of the density inside a ring with thickness  $\delta r'$ ,

$$G(r') = 2\pi \int_{r'}^{r'+\delta r'} n(r') r' dr' \quad , \quad (5.2)$$

and it is normalized by the cloud total number of atoms,  $N$ .

If the ring thickness is very small ( $\delta r' \ll r'$ ), the bulk density variation inside the

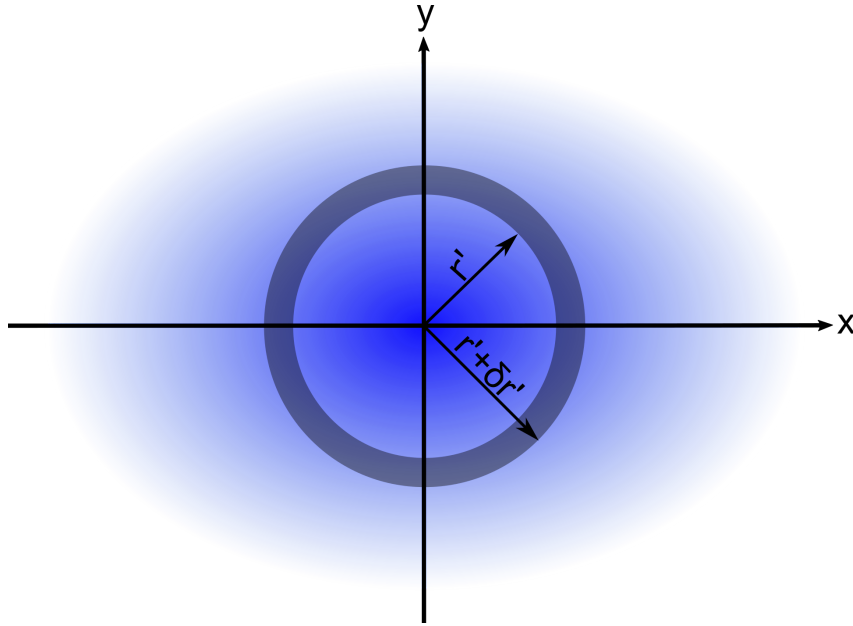


Figure 20 – Illustration about the method to compute  $G(r')$ . The atomic density distribution,  $n(x, y)$ , is pictured by the blue region. The dark area represents the region that will give  $G(r')$  for a radius  $r'^2 = x'^2 + y'^2$ .

Source: By the author.

ring is smooth. In this way, from Equation (5.2) we obtain

$$n'(k') \approx C \frac{G(k')}{k'} , \quad (5.3)$$

where we used Equation (5.1) to map position with the *in situ* momentum, and the constant  $C$  is determined by the normalization,

$$\int n'(k') k' dk' = N . \quad (5.4)$$

Thus, to determine the projected momentum distribution,  $n'(k')$ , we use the Equation (5.3). At this point, it is important to emphasize that the obtained momentum distribution,  $n'(k')$ , represents a 2D-projected momentum distribution, since the absorption image is a 2D integrated projection of the actual density distribution. While previous work (57) explained a way to recover the full momentum distribution, through an Abel transformation of  $n'(k')$ , here we restrict ourselves to the projected momentum distribution since it is enough to illustrate the effects we want to describe. In the next section, we present the results of the projected momentum distribution for a perturbed BEC, as a function of hold time and excitation amplitude.

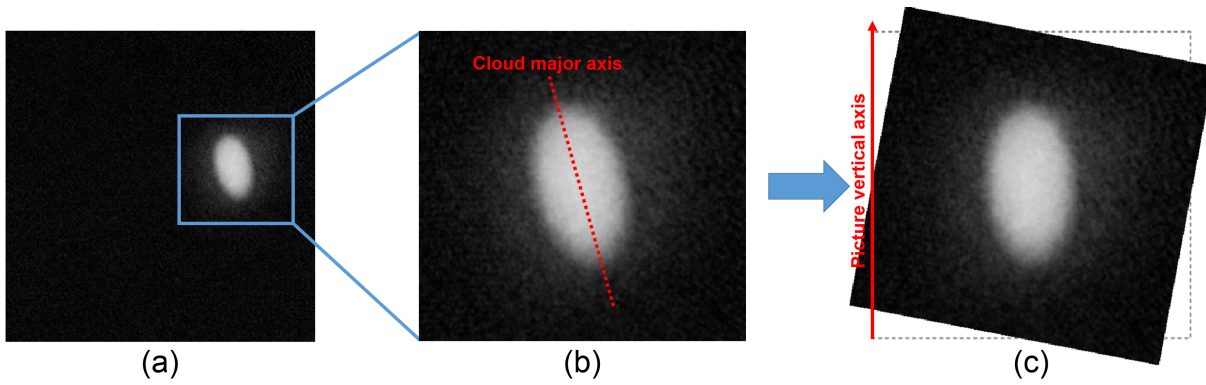


Figure 21 – Eliminating dipolar and scissors mode effect. (a) full absorption image. (b) Image centered in the cloud center-of-mass showing the cloud major axis. (c) Tilted image to match the cloud major axis with the picture vertical axis.

Source: By the author.

### 5.3 Momentum distribution coupled to the quadrupolar mode

We have used the same experimental dataset from which we analyzed the collective modes, to investigate the projected momentum distribution of a perturbed condensate.

We analyze each image by centering in the cloud center-of-mass and tilting the image to match the cloud major axis with the vertical axis of the picture, these two steps are illustrated in Figure 21. With this simple procedure we immediately eliminate any possible effect of the dipolar and scissors mode to our momentum distribution analyses.

From this point, we extract the projected momentum distribution of the cloud. The Figures 22(a)-(b) presents momentum distributions,  $n'(k')$ , of the non-excited BEC (black squares) and excited BECs (colored symbols) for different hold times.

We observed from Figures 22(a)-(b) a typical shape of the momentum distribution curves (in log scale) for cold atoms, as observed in (57) previous work. For a non-excited BEC (black square), the curve is almost constant for smaller  $k'$  values and follows in a smooth fall to zero. This behavior does not reveal any power-law and is characteristic of a Thomas-Fermi distribution. (100) When the BEC is excited the curve is changed. If we fix in one hold time, we can see that for smaller excitation amplitude, Figure 22(a), the

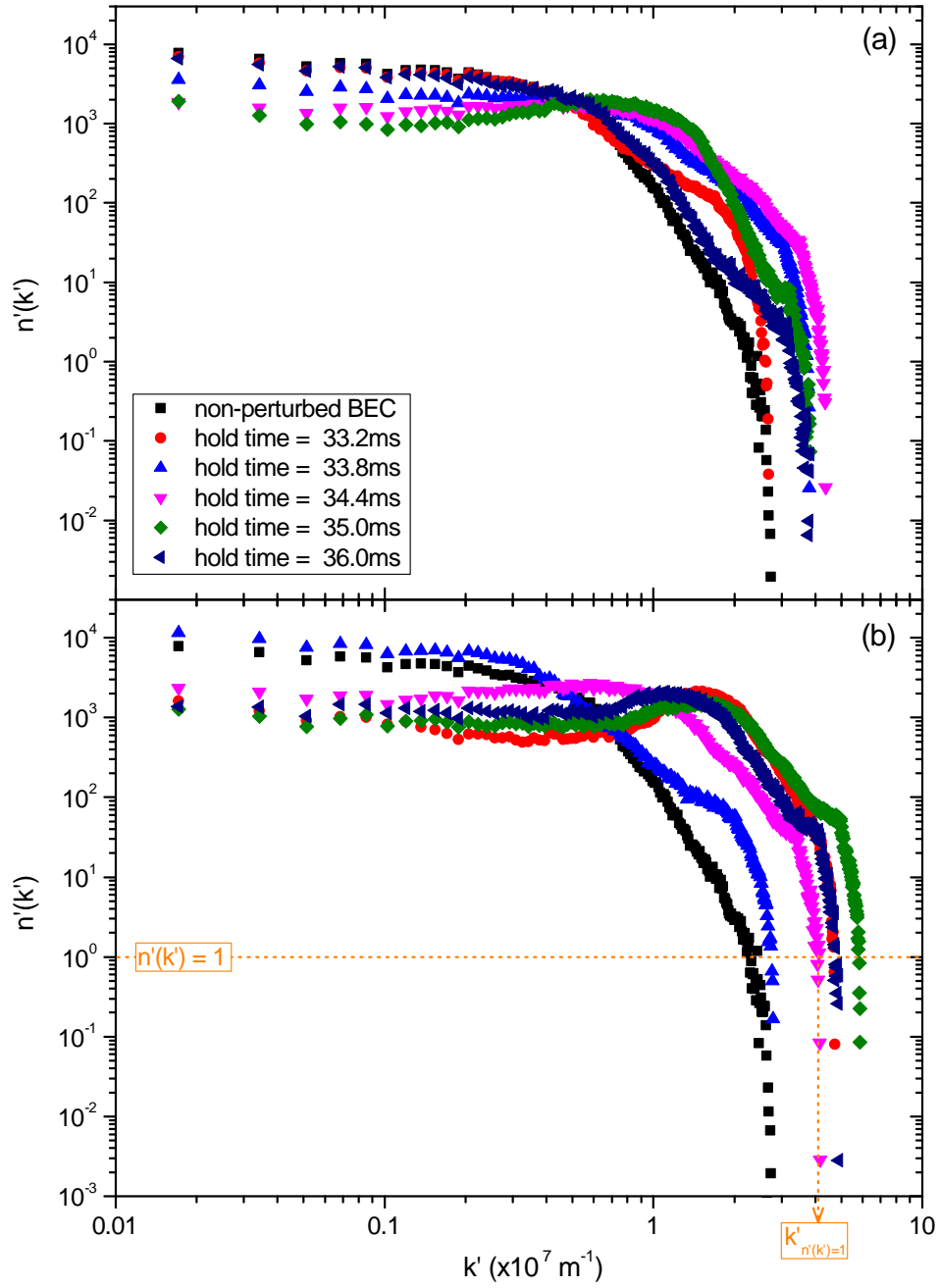


Figure 22 – Projected momentum distribution of non-excited BEC (black squares) and excited BECs (colored symbols) for different hold times. (a) Non-turbulent cloud (315 mG/cm of excitation amplitude). (b) Turbulent cloud (Excitation amplitude equal to 470 mG/cm).

Source: By the author.

curve looks like a non-excited BEC curve, however, it is more spread in  $k'$  values. For higher excitation amplitude, Figure 22(b),  $n'(k')$  is different from a non-excited BEC and has a characteristic shape of a turbulent regime: this curve exhibits a plateau for smaller momenta (the energy containing range), an almost linear decrease in the intermediate region (the inertial range) and a sharp decrease in the maximum momentum value of the

cloud (the dissipation range).

Now, if we fix the excitation amplitude and look how the curves change as the hold time is varying (i.e., focus on one of the Figures 22(a)-(b) per time) we can observe that the curve oscillates from a compressed curve (like a non-excited BEC) to a more widespread one. Furthermore, in the turbulent regime, all three regions (the energy containing range, the inertial range and the dissipation range) change their values and slopes as a function of the hold time.

Therefore, the momentum distribution changes its shape as a function of the in-trap evolution time, an aspect that has not been investigated in previous works. This causes, in the linear decrease region, an slope dependence with the hold time. We can explain the discrepancy obtained for the power-law results in previous work (57), where they analyzed the momentum distribution of a turbulent cloud for a fixed hold time. In other words, the excitation of the cloud normal modes modifies the size and shape of the cloud and affect the momentum distribution. As mentioned before, during the  $n'(k')$  analyses process, we remove any possible contribution of the dipolar and scissos mode, in that sense, the quadrupolar mode is the responsible to hinders the actual momentum distribution.

To verify this coupling between the momentum distribution and the quadrupolar mode, we concentrate in the final maximum momentum region. We fixed a  $n'(k')$  value and studied how the momentum  $k'$ , that gives the value  $n'(k')$ , change with respect to the hold time. In this work, we set the value  $n'(k') = 1$  and analyzed its correspondent momentum value, that we call  $k'_{n'(k')=1}$ , as represented in Figure 22(b).

In Figure 23(a) we plot  $k'_{n'(k')=1}$  as a function of hold time, for 470 mG/cm of excitation amplitude. We can see that  $k'_{n'(k')=1}$  evolve sinusoidally with a frequency of 365(4) Hz, which is equal to the quadrupolar mode frequency, as investigated in Chapter 4. The red line gives the reference for a non-excited BEC.

Furthermore, for each excitation amplitude we fitted a sinusoidal function and extracted the  $k'_{n'(k')=1}$  oscillation amplitude. In Figure 23(b) we present the  $k'_{n'(k')=1}$  os-

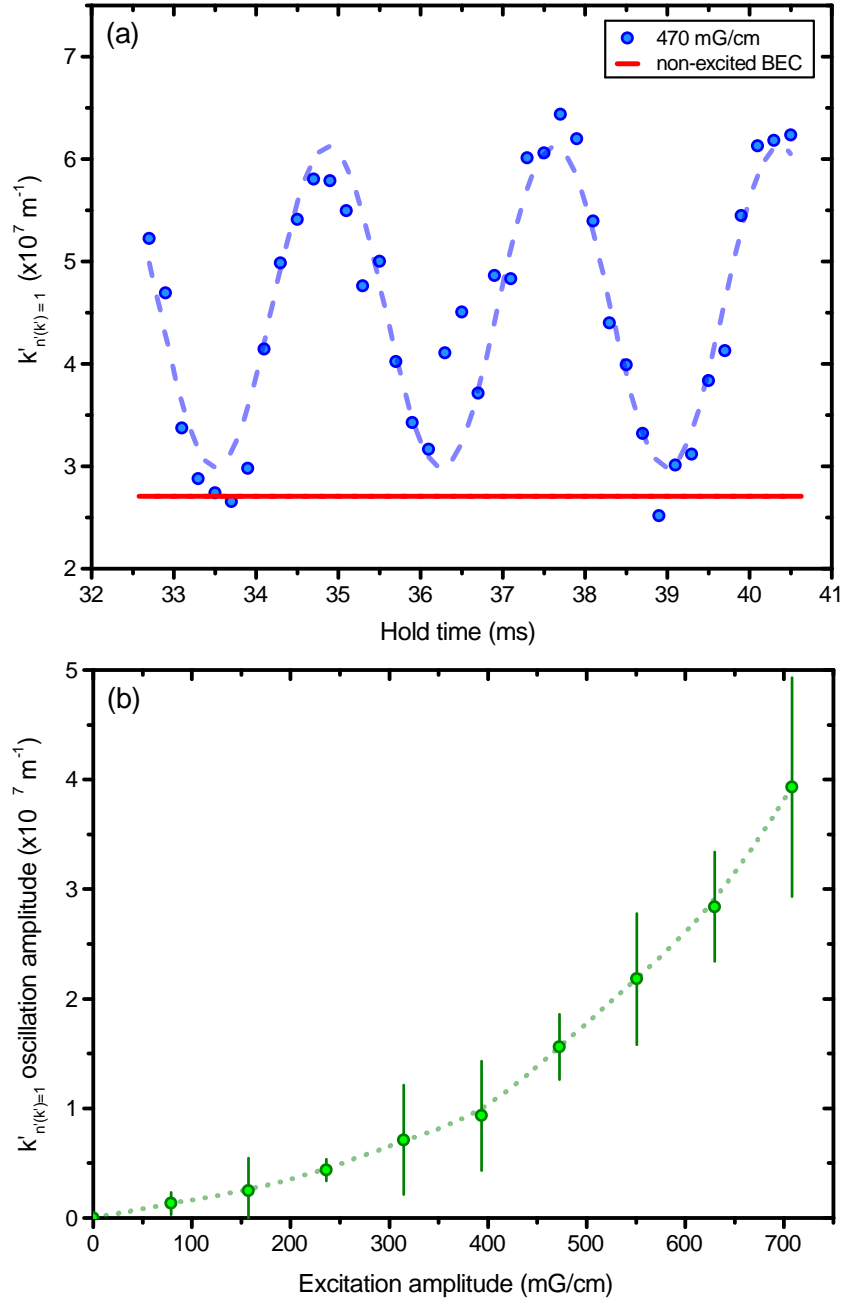


Figure 23 –  $k'_{n(k)=1}$  oscillation as a function of the in-trap time, showing a sinusoidal behavior with frequency matching the BEC quadrupole mode frequency. (b) Amplitude of the fitted oscillation as a function of the excitation amplitude, showing a non-linear behavior as observed for the quadrupolar mode.

Source: By the author.

cillation amplitude as a function of the excitation amplitude. Comparing Figure 23(b) with Figure 17(b) it is clear the same non-linear behavior as observed for the quadrupolar mode. (130) This gives an extra indication of the coupling between the momentum distribution and the quadrupolar collective mode.

In conclusion, applying our method to extract the momentum distribution in a

turbulent BEC, we observed a power-law behavior as expected by the Kolmogorov law. Nevertheless, the slope in the intermediate region is dependent of the quadrupolar mode. The main consequence of this coupling is that we cannot extract a precise quantitative analysis of the turbulent cloud momentum distribution. The further understanding of this coupling might shine some light on how to decouple them and eventually on the understanding of the momentum distribution of Bose-Einstein condensates under various conditions, in particular displaying vortices and turbulence.

Another way to investigate the properties of quantum turbulence is by considering its wave nature. It is well known that, during the expansion in time-of-flight, the condensate exhibits the so called aspect ratio inversion. This particular characteristic is a manifestation of the BEC matter wave properties. However, as shown in Figure 18, the expansion of a turbulent BEC happens in a self-similar way (i.e. the aspect ratio inversion does not occurs). This different behavior infers that some of the matter wave proprieties are affected by the large fluctuations in the density distribution of turbulent clouds. In the next chapter, we will study the turbulent regime by considering its wave expansion properties.

# 6 Quantum turbulence and statistical atom optics

In this chapter, we analyze the properties of a turbulent atomic superfluid by taking into account its matter wave nature. The randomness of amplitude and phase introduced in the turbulent cloud allows an analogy between the free expanding turbulent cloud (disordered matter wave) and the propagation of a speckle light field (disordered optical wave). The divergence during the propagation are compared to explain common features for both waves. Second-order correlation proves the analogy of a turbulent atomic cloud in expansion and the propagation of a speckle field creating new exciting possibilities to understand the behavior of quantum matter coexisting with disorder. The propagation of a three dimensional speckle field creates an unique opportunity to investigate this phenomenon in higher than two dimensions. This study had been developed in collaboration with Prof. Robin Kaiser (INLN) and Prof. Dr. François Impens (UFRJ).

## 6.1 Motivation

The investigation of ultracold trapped atoms has motivated new exciting discoveries. Applications range from condensed matter to fundamentals of quantum theory. (60, 131) Many-body physics has acquired a considerable advance including the possibility of quantum simulations with ultracold atoms. (12, 132) The propagation of coherent atomic waves has been the object of various theoretical (133, 134) and experimental studies (135, 136), including the Anderson localization of matter waves in a disordered potential. (11, 137) The superfluidity aspects of those systems was an important ingredient for investigation of quantized vortices. (30) An intriguing and exciting topic is the evolution of a vortex distribution to a tangle configuration characterizing quantum turbulence (QT).

(138) The emergence of QT in trapped atomic superfluid (33,34) opened up a new range of possibilities to study. The low atomic density allows direct observation of the vortices which can be detected with optical techniques, generating the possibility for the study of individual events related to vortices interaction and to their overall dynamics.

In a trapped atomic gas, the confining potential can be suddenly switched off, leaving the sample free to expand. This free expansion provides a clear signature of the quantum degeneracy in experimental BEC production in anisotropic traps (118), the aspect ratio inversion during time-of-flight. It also reveals the self-similar expansion, a characteristic behavior of turbulent BEC. (33,139) Another important aspect of expanding quantum fluids is that interactions are normally turned off after the first TOF (129), letting the expanding cloud to preserve similar properties to the *in situ* structure.

On the other hand, the description of a propagating coherent Gaussian beam and a speckle beam is a well established research area. (140,141) A propagating Gaussian beam with an elliptical cross section will exhibit an aspect ratio inversion due to the different divergence angles in the orthogonal directions. (142)

Beyond those propagation similarities, in the turbulent condensate the association of tangled vortices results in large fluctuations of density and phase. The predominance of vortices characterize the superfluid turbulence while only large fluctuations of density characterize the wave turbulence. (143) We normally define the overall scenario as quantum turbulence in which energy flows between scales by the energy cascade. In any case, the randomness and large deviation from equilibrium make the turbulent cloud a macroscopic combination of amplitudes and phases randomly distributed to the sample. Such a picture of a turbulent cloud strongly reminds us of a speckle light field. The main characteristic of a speckle light field is that the speckle pattern arises from a sum of complex statistically independent amplitudes bearing a random phase and module. (141)

## 6.2 Equivalences between matter and optics waves

We compare the experimental results for the free expansion of a regular BEC and turbulent condensate with numerical simulation results for the propagation of a coherent Gaussian beam and a speckle beam, in free space. The numerical simulation was provided in collaboration with Prof. Dr. François Impens (UFRJ) and Prof. Robin Kaiser (INLN). In general lines, the Gaussian beam propagates in  $z$  direction and it has an elliptical cross section. The waists at the focal point are  $w_{0x}$  and  $w_{0y}$  in  $x$  and  $y$  direction, respectively. These waists are chosen to have the same *in situ* BEC aspect ratio,  $\frac{w_{0x}}{w_{0y}} = \frac{1}{9}$ . For the generation of the speckle beam, a speckle mask is introduced at the focal point of that Gaussian beam, and its propagation is simulated from that point. Details about the Gaussian beam propagation and speckle beam simulations can be found in (140, 141) references. These results are summarized in Figure 24. We can see that the atomic clouds expansion and the optical beams propagation have the same behavior.

For a traditional Bose condensed gas, Figure 24(a), a clear signature of the quantum degeneracy is the aspect ratio inversion during free expansion after the cloud is released from an anisotropic trap. It is noticeable that for shorter TOF the BEC is elongated in one direction and for longer TOF it is elongated in the transverse direction. This is very distinct from a thermal cloud in free-expansion, which always evolves to an isotropic cloud (i.e. the aspect ratio tending to unit). For a turbulent quantum gas, Figure 24(a), a remarkable behavior is that it keeps the aspect ratio mostly unchanged in free expansion. (33, 34, 139, 144)

Now, If we look the propagation of a Gaussian beam, Figure 24(c), it has an aspect ratio inversion, like for a regular BEC. Furthermore, the simulation of the speckle beam propagation, Figure 24(d), shows the same characteristic of turbulent clouds: the aspect ratio is almost constant during expansion.

In order to compare the propagation of both waves, we analyze how their typical dimensions evolve. The results for the free expansion of the turbulent and non-turbulent

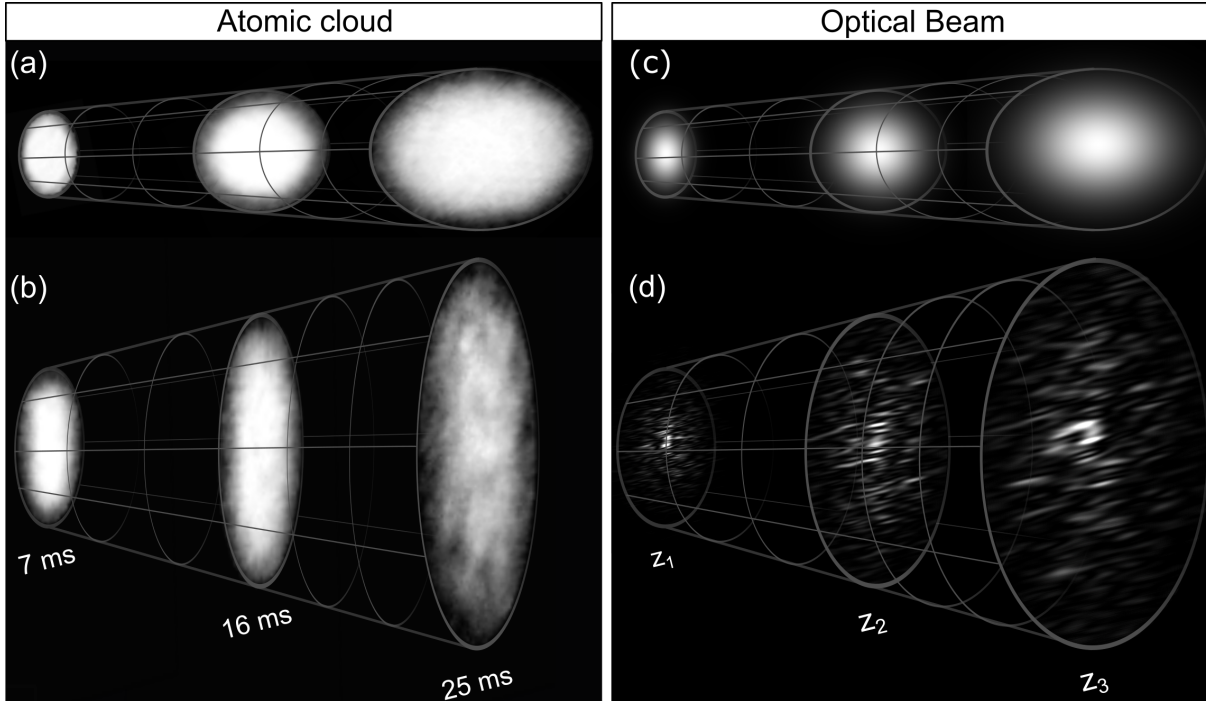


Figure 24 – Atomic cloud expansion and optical beam propagation. Sequence of three different time-of-flight showing the expansion of a (a) regular BEC and (b) turbulent cloud. Sequence of three different propagation distance showing the expansion of a (c) Gaussian and (d) Speckle beam. The propagation distances  $z_1$ ,  $z_2$  and  $z_3$ , are chosen to the Gaussian beam aspect ratio match with the regular BEC one at the three given TOFs in (a).

Source: By the author.

clouds are shown in Figure 25, where the cloud radii are plotted as a function of time-of-flight. For an equilibrium BEC in expansion, Figure 25(a), the initial smallest radius ( $R_y$ ) expands faster than the longest one ( $R_x$ ) and the aspect ratio inversion occurs at the crossing point around TOF = 8.5 ms. From this curves we can extract the expansion rate for both directions:  $\dot{R}_x^{\text{BEC}} = 0.47(1) \mu\text{m/ms}$  and  $\dot{R}_y^{\text{BEC}} = 3.9(1) \mu\text{m/ms}$ .

On the other hand, for the turbulent cloud in free expansion, Figure 25(b), the initial longest radius ( $R_y$ ) expands faster than the smallest one ( $R_x$ ), which means that the aspect ratio never inverts. Thus the turbulent cloud indicates a self-similar expansion with an aspect ratio almost constant during the whole expansion. In this case, the expansion rates are:  $\dot{R}_x^{\text{Turb}} = 1.5(1) \mu\text{m/ms}$  and  $\dot{R}_y^{\text{Turb}} = 5.3(2) \mu\text{m/ms}$ . Here, we can note that each direction expands faster than the regular BEC ones. Which leads to the relation  $\dot{R}_i^{\text{Turb}} > \dot{R}_i^{\text{BEC}}$ , in each  $i$ -direction.

The numerical simulation results for the propagation of an elliptical Gaussian light

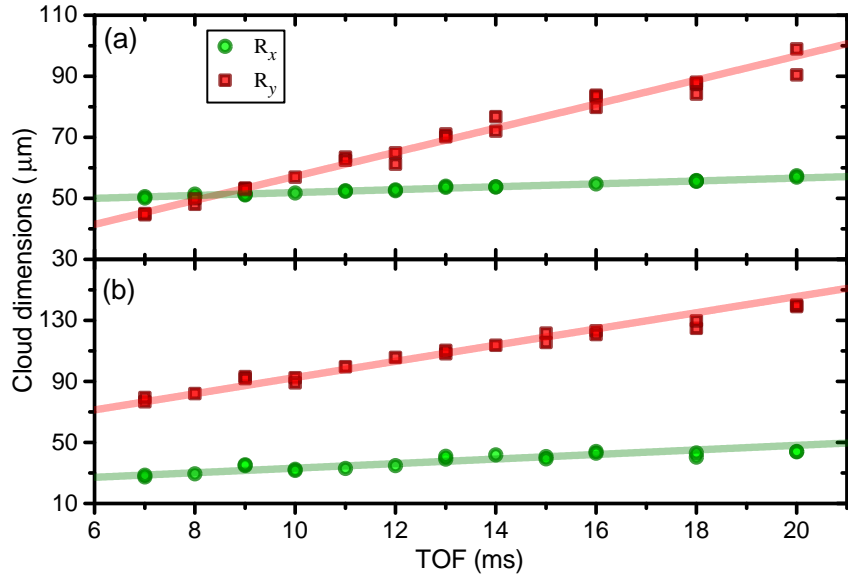


Figure 25 – Cloud expansion during time-of-flight. Cloud dimensions  $R_x$  and  $R_y$  along the  $x$  and  $y$  directions, as a function of the time-of-flight for a (a) regular BEC and (b) turbulent BEC.

Source: By the author.

beam without or with speckles are presented in Figure 26, where the beam waists\* are plotted as a function of the propagation distance. For the coherent beam, Figure 26(a), aspect ratio inversion occurs after some propagation distance, and for the speckle field that does not happen, Figure 26(b), and the speckle beam propagates in a self-similar shape. From these curves we can extract the beam divergence in each direction and for both cases. The results for a coherent Gaussian beam are:  $\dot{w}_x^{\text{Gauss}} = 39.64(2) \times 10^{-3}$  and  $\dot{w}_y^{\text{Gauss}} = 0.48(1) \times 10^{-3}$ . In the speckle beam case, the divergences are:  $\dot{w}_x^{\text{Speckle}} = 0.098(5)$  and  $\dot{w}_y^{\text{Speckle}} = 0.167(6)$ . In the simulation of Figure 26, both beams started with same elliptical cross section,  $w_{0x}$  and  $w_{0y}$ , and their evolution with the propagation is quite distinct due to the presence of the speckle pattern. The speckle beam divergence is higher than the coherent Gaussian beam. This leads to  $\dot{w}_i^{\text{Speckle}} > \dot{w}_i^{\text{Gauss}}$ , in each  $i$ -direction, similar to the atomic cloud case.

Since the Gaussian beam (and speckle field) as well as the regular BEC (and turbulent cloud) satisfy similar propagation equation, we analyze their features in an unified approach. In terms of light propagation, let first consider a Gaussian coherent laser beam propagating in space and consider that it has an elliptical cross section with

\* The beam waists are numerically evaluated by the second moment of the beam intensity profile. (140)

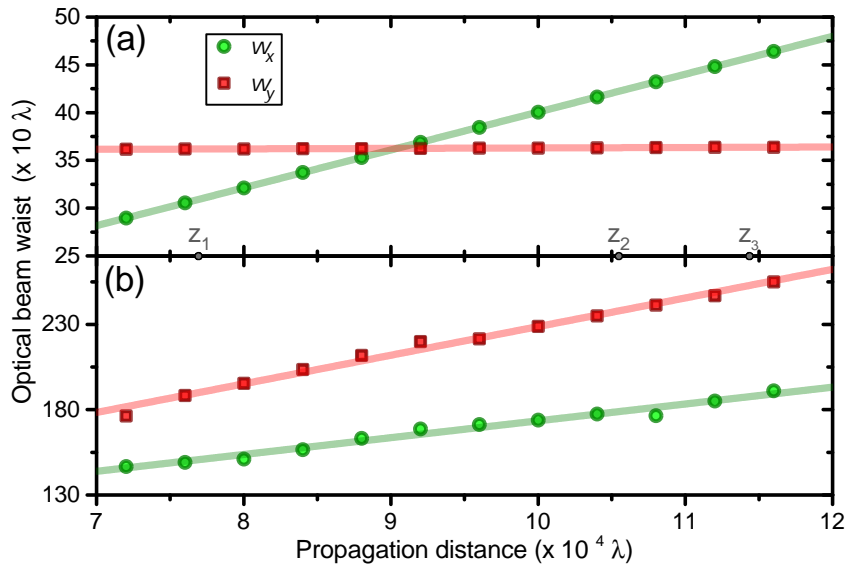


Figure 26 – Optical beam waists propagation. Beam sizes  $w_x$  and  $w_y$  along the  $x$  and  $y$  directions, as a function of the propagation distance for a (a) coherent Gaussian and (b) speckle beam. In the marked propagation distances  $z_1$ ,  $z_2$  and  $z_3$ , the Gaussian beam aspect ratio match with the regular BEC one at the three TOF of Figure 24(a).

Source: By the author.

waists  $w_{0x}$  and  $w_{0y}$  at the focal point. The divergence angle of the beam, in each  $i$ -direction, is given by  $\tan \theta_i^c = \frac{\lambda}{w_{0i}}$ , where  $\lambda$  is the wavelength and  $c$  refers to the coherent case. A smaller waist at the focus leads to a larger divergence, with higher angle. Therefore, the coherent laser propagation presents an inversion of the aspect ratio. This is equivalent to the expansion of the equilibrium BEC, which also presents inversion of the aspect ratio and agree with our observations above. If we consider the same elliptical beam, but now with a speckle pattern on it, the divergence as it propagates is quite different. The divergence angle for each direction is given by  $\tan \theta_i^d = \frac{\lambda}{\ell_i}$ , where  $\ell_i$  is the correlation length in the  $i$ -direction and  $d$  refers to the disorder case.

The data presented for the optical beams divergences, Figure 26, provides that  $\tan \theta_i^d > \tan \theta_i^c$ . That occurs when  $\ell_i < w_{0i}$ , i.e. for a beam with many speckle grains, having a divergence angle larger for the case of speckle. With the atomic clouds data, Figure 25, the expansion rates (equivalent to divergence angle) result in  $\tan \theta_i^d > \tan \theta_i^c$ , also given  $\ell_i < w_{0i}$  for the matter wave propagation. Notice that for the matter wave, the cloud radii is equivalent to the beam waists. Such consistent propagation behaviors and this microscopic description, allow us to establish an analogy between the propagating

speckle light field and the expansion of a matter wave originated from a turbulent quantum gas.

### 6.3 Second-order correlation function

Another way to investigate the equivalences between the propagation of these two waves is evaluating the second order correlation function. (141) In what follows, the atomic density plays a role completely analogous to the optical intensity. In Figure 27, we present the cross section intensity profile of a speckle field together with the density absorption profile for the expanding turbulent cloud. The similarities involving amplitudes distribution is clear. Note that the amplitude of fluctuations in the turbulent BEC density profile is smaller than in the speckle beam intensity profile. The column integration in the absorption image process reduces the amplitude of density variations.

Stating that intensity and density are equivalent quantities, we can evaluate the density-density correlation function<sup>†</sup>,  $g^{(2)}$ , for the expanded matter wave and compare it with its equivalent in the speckle field. For 30 ms of time-of-flight, the correlation function

$$g^{(2)}(\Delta r) = \frac{\langle n(r) n(r + \Delta r) \rangle}{\langle n(r) \rangle \langle n(r + \Delta r) \rangle} \quad (6.1)$$

for a regular BEC and a turbulent cloud are presented in Figure 28(a). The correlation for a regular BEC is basically constant and close to unity. At short distances,  $g^{(2)}$  is slightly larger than unity due to the small thermal fluctuations originated from the thermal atoms component as well as the finite size effects present in those samples. The turbulent cloud clearly shows a larger  $g^{(2)}$  for shorter distances and a typical exponential decay, which is the result of a correlation length ( $\ell_{Turb} = 8.5(2) \mu\text{m}$ ) much shorter than the sizes of the cloud ( $R_x = 63(3) \mu\text{m}$  and  $R_y = 198(6) \mu\text{m}$ ) and indicates the presence of fluctuations at smaller scales. This is exactly the same behavior observed in Section 6.2.

---

<sup>†</sup> See Appendix A for details.

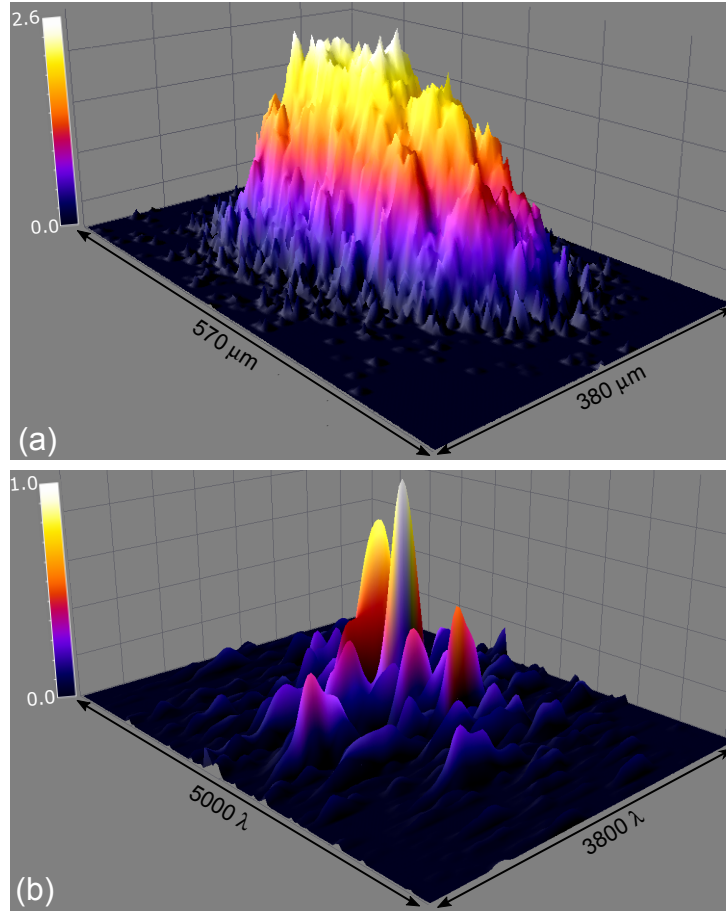


Figure 27 – Comparison between turbulent cloud and speckle beam. (a) column integrated density profile for a turbulent BEC and (b) intensity profile for the cross section of a speckle beam. The integration in one of the 3D dimension of the BEC cloud result in slight reducing the amplitude of density variations.

Source: By the author.

The  $g^{(2)}$  for the coherent Gaussian beam and the speckle beam are presented in Figure 28(b). The correlation for a Gaussian beam is basically constant, close to unity, as expected. (141) The speckle beam shows a larger  $g^{(2)}$  for shorter distances and a typical exponential decay, which is a result of a much shorter correlation length ( $\ell_{\text{Speckle}} = 15.8(8)\lambda$ ) than the beam waists ( $w_x = 1876\lambda$  and  $w_y = 2528\lambda$ ), which also indicates the presence of fluctuations at smaller scales. Again, this is exactly the same behavior observed in Section 6.2.

An important point concerning our measurements is the use of absorption images, which corresponds to a projection of the three dimensional cloud onto two dimensional plane. Despite the fact that this procedure reduces the amplitude of the detected fluctuations (as shown in Figure 27), the correlation length measured after projection is the

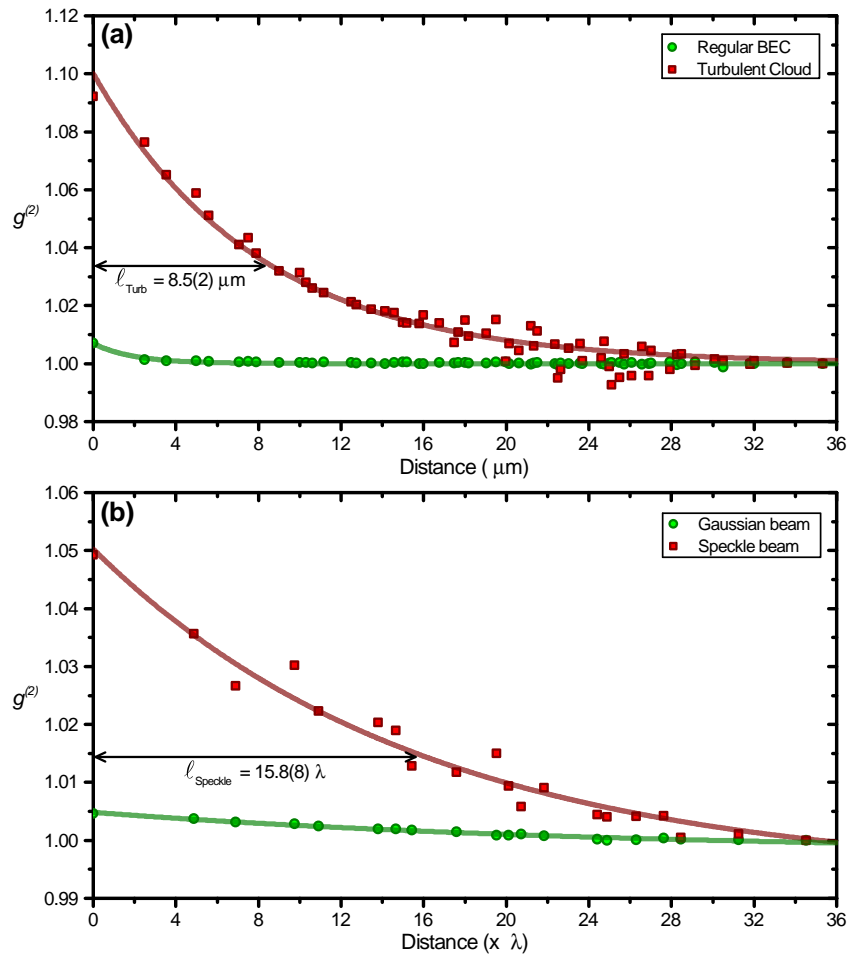


Figure 28 – Second-order correlation function. (a)  $g^{(2)}$  for a regular BEC (green circles and green fitted line) and a turbulent cloud (red squares and red fitted line) as a function of distance,  $\Delta r$ . (b)  $g^{(2)}$  for a Gaussian (green circles and green fitted line) and a speckle beam (red squares and red fitted line) as a function of distance,  $\Delta r$ , in units of  $\lambda$ .

Source: By the author.

same as in three dimensions. We support this claim by simulating a 2D optical speckle beam and its projection in one dimension, which are used to investigate the effects on to the correlation length measured from  $g^{(2)}$  correlation function. We observe that although the amplitude of the correlation function is reduced, the length scale of the fluctuation extracted from the correlation function remains unaffected<sup>‡</sup>.

The comparison between quantum turbulent BEC and speckle light only makes sense for an expanding cloud, which is equivalent to the matter wave propagation. In both, expanding matter wave and propagating light wave, the contained structures are frozen and therefore can not really provide the *in situ* dynamics that takes place during

<sup>‡</sup> See Appendix B for details.

the disorder onset introduced by the turbulence.

While light propagation is a well established subject and, in particular, speckle is also a well understood topic, the matter wave propagation is still in its very infancy. The introduction of disorder in matter wave, done through the emergence of turbulence in an atomic cloud, opens up a new window of research to better understand the nature of the disorder in the “quantum world”. Moreover, it may provide some insights concerning the intrinsic behavior of quantum turbulence. The possibility of having speckle matter waves was previously demonstrated (145) in a different context. In that study, a Bose-Einstein condensate guided by a light beam create a speckle pattern in the image. Their  $g^{(2)}$  correlation function in time was equivalent to the one here presented. Even though, here we report on similarities in the spatial fluctuations and the underlying physics of propagating speckle beam and disorder matter wave.

Speckle like behavior in turbulent quantum fluids consists of a three-dimensional speckle field and may be an excellent candidate to explore important aspect about the structures and the tomography of speckle fields in three dimensions.

# 7 Conclusions and prospects

In this chapter we present our main conclusions about the previous chapters. Moreover, we discuss possible prospects to improve the *BEC-I* experimental system with an alternative method to generate quantum turbulence, without excite the BEC collective modes, which can provide a more conclusive study concerning on the momentum distribution of a turbulent atomic superfluid.

## 7.1 Conclusions

In our group, the experimental research in quantum degenerate gas has been developed some time ago. (37, 38, 98, 146, 147) One of the most exciting results is related to the condensate's superfluid properties: (31, 33) the quantum vortices formation and the emergence of quantum turbulence. In the thesis presented here, we explore a condensate perturbed by an external oscillating excitation, and our study contributes in better understanding the generation of QT and its properties.

We produced Bose-Einstein condensates containing around  $N_0 = 1.8 \times 10^5$  atoms with a condensate fraction about of  $\frac{N_0}{N} \approx 0.7$ , following the processes described in Chapter 3. In order to excite the trapped BEC, a sinusoidal gradient magnetic field was superimposed in the trapping potential, right after the BEC is produced, during an excitation time and then it is switched off. The cloud was held trapped during a hold time. Then, the magnetic trap was switched off and the excited BEC was observed by absorption image, after expanding during a time-of-flight.

Our first results, concerning the excitation of collective modes in the condensate, were described in Chapter 4. For different excitation amplitudes, we change the hold time to observe the cloud dynamics inside the trap. We could conclude that:

- (a) The cloud's center of mass oscillates as the hold time is changed. This characterizes the dipolar collective mode of the BEC. We measured the frequency of this oscillation and obtained  $f_d = 185(3)$  Hz, which matches the radial trap frequency,  $f_r = \frac{\omega_r}{2\pi} = 188$  Hz and agrees to the theoretical prediction, Section 2.3.
- (b) The condensate shape also changes during the dipolar motion. To characterize this, we measure the BEC aspect ratio ( $AR$ ) during the hold time evolution. We found that the  $AR$  oscillates with a frequency  $f_q = 375(8)$  Hz. This frequency is approximately  $2f_r$ , which corresponds to the  $m = 0$  fast quadrupolar mode (also called breathing mode).
- (c) These frequencies are mostly constant, for excitation amplitudes lower than 400 mG/cm, and a slight decrease (2–3%) for larger amplitudes was observed. Similar results about the frequency shifts of collective modes were seen before. (115, 124)
- (d) The analysis of the dipolar and quadrupolar mode amplitude, as a function of the excitation amplitude, showed that the dipolar mode is easily excited even for low excitation amplitudes. The CM oscillation amplitude increased linearly with the excitation amplitude. However, the quadrupole mode presented an interesting non-linear behavior for excitation amplitudes lower than 400 mG/cm and had a huge linear increase for higher amplitudes. This means that, there may be a minimal energy to efficiently excite the condensate quadrupolar mode.
- (e) As the excitation amplitude increases, the dipolar mode amplitude gets higher, thus the condensate is pushed farther away from the trap bottom. In a QUIC trap, the BEC reaches anharmonic region as far it is going from equilibrium point. These outer regions of the trap have a much steeper gradient field, which compress the cloud and is more suitable to produce shape oscillations in the BEC. This means that, as the dipolar motion is increased, the quadrupolar mode is more excited. This is consistent with the non-linear behavior to excite the BEC quadrupolar mode. This coupling dynamics, between the dipolar and quadrupolar mode, seems particular to our excitation system. It may also be the key to the better understanding of the vortex nucleation and the turbulence emergence observed in previous (33, 34, 125) experiments.

- (f) For amplitudes larger than 500 mG/cm, when the quadrupolar mode was effectively excited, the perturbed condensates exhibited a couple of vortices. The TOF expansion of these clouds showed the aspect ratio non-inversion, an observed characteristic of turbulent BEC clouds. These two observations highly suggest a turbulent state of the atomic superfluid.

In references (31,33,34), our group reported the first observation of quantum turbulence. The results presented complements our understanding about the QT generation mechanism and were published in (123) reference.

We studied the momentum distribution of the perturbed BEC clouds, in Chapter 5. The cloud 2D-momentum distribution,  $n'(k')$ , was analyzed during its collective oscillations inside the trap. The main conclusions can be summarized as following:

- (a) For a non-excited BEC, the momentum distribution curves did not reveal any power-law. It is almost constant for smaller  $k'$  values and smoothly fall to zero as  $k'$  increases. This behavior is a characteristic of a Thomas-Fermi distribution. (100)
- (b) The  $n'(k')$  curves changed as the BEC was perturbed. For a fixed hold time, if the excitation amplitude was low ( $< 400$  mG/cm), these curves are similar to the non-excited BEC curves, however, it is more spread in  $k'$  values. On the other hand, as the excitation amplitude was increased, the  $n'(k')$  curves start to present a characteristic shape of a turbulent regime: a plateau for smaller momenta (the energy containing range), an almost linear decrease in the intermediate region (inertial range) and a sharp decrease in higher momentum values (dissipation range). Therefore, for the excitation amplitude range where the condensate absorption image suggested a turbulent cloud, the  $n'(k')$  curve also revealed a behavior similar to the turbulence phenomenon.
- (c) The momentum distribution curves as a function of the hold time was studied. We observed that the curve shape oscillates from a compressed curve (like a non-excited BEC) to a more widespread one. Furthermore, in the turbulent regime, all three regions (the energy containing range, the inertial range and the dissipation range) change their values and slopes as the hold time was varied. Therefore, the excitation

of the cloud normal modes modifies the size and shape of the cloud and affects the momentum distribution. This causes a slope dependence with the hold time, in the inertial range, which explains the discrepancy obtained for the power-law results in previous (57) work.

The first measurements of the momentum distribution of a turbulent BEC cloud was reported in the article (57) of our group. The result presented here clarify the observed discordance from the Kolmogorov spectrum and were published in (130) reference. It is also part of a master thesis. (126)

Finally, the last result presented in this thesis was the comparison between an expanding turbulent cloud and a propagating speckle light beam. This work had been done in collaboration with Prof. Robin Kaiser and Prof. François Impens. They could simulate the propagation of a coherent Gaussian beam and of a speckle Gaussian beam. In Chapter 6 we compared the experimental results, for the non-perturbed BEC and for the turbulent BEC, with their simulations. The conclusion are listed below:

- (a) The expansion of a non-perturbed (coherent) condensate, after released from the anisotropic trap, presented the aspect ratio inversion, which is a signature of the quantum degeneracy. For a turbulent quantum gas, the remarkable observed behavior was that it keeps the aspect ratio mostly unchanged in free expansion.
- (b) For the light beam case, the propagation of a coherent elliptical Gaussian beam exhibited an aspect ratio inversion, like for a regular BEC. Furthermore, the simulations of the speckle beam propagation, presented the same characteristic of turbulent clouds: the aspect ratio was almost constant during propagation.
- (c) We measured the expansion (propagation) divergence by fitting the data for the expansion of the BEC radii (optical waists). The results for a quantum gas were: for the coherent case,  $\dot{R}_x^{\text{BEC}} = 0.47(1) \mu\text{m/ms}$  and  $\dot{R}_y^{\text{BEC}} = 3.9(1) \mu\text{m/ms}$ ; and for the turbulent case,  $\dot{R}_x^{\text{Turb}} = 1.5(1) \mu\text{m/ms}$  and  $\dot{R}_y^{\text{Turb}} = 5.3(2) \mu\text{m/ms}$ . The results for the optical beam were:  $\dot{w}_x^{\text{Gauss}} = 39.64(2) \times 10^{-3}$  and  $\dot{w}_y^{\text{Gauss}} = 0.48(1) \times 10^{-3}$  for a coherent beam; and for the speckle beam,  $\dot{w}_x^{\text{Speckle}} = 0.098(5)$  and  $\dot{w}_y^{\text{Speckle}} = 0.167(6)$ .
- (d) The divergence measurement provides that  $\tan \theta_i^d > \tan \theta_i^c$ , where  $\theta_i$  is the divergence

angle in the  $i$ -direction for the coherent,  $c$ , or disordered,  $d$ , cases. This implies that  $\ell_i < w_{0i}$ , where  $\ell_i$  is the coherent length of the disordered wave and  $w_{0i}$  are the sizes of the coherent wave at the focus position (or initial TOF). Such consistent propagation behavior and this microscopic description, allowed us to establish an analogy between the propagating speckle light field and the expansion of a speckle matter wave, originated from a turbulent quantum gas.

- (e) We also demonstrated this analogy by calculating the second-order correlation function,  $g^{(2)}$ . For the matter wave: the coherent BEC showed a  $g^{(2)}$  that was basically constant, and close to unity, in the distance range; and the turbulent cloud presented a larger  $g^{(2)}$  for shorter distances and a typical exponential decay, which is the result of a correlation length ( $\ell_{Turb} = 8.5(2) \mu\text{m}$ ) much shorter than the sizes of the cloud ( $R_x = 63(3) \mu\text{m}$  and  $R_y = 198(6) \mu\text{m}$ ) and indicates the presence of fluctuations at smaller scales. For the light wave: the correlation function for a coherent Gaussian beam was basically constant, close to unity, as expected (141); and the speckle beam showed a larger  $g^{(2)}$  for shorter distances and a typical exponential decay, which is a result of a much shorter correlation length ( $\ell_{Speckle} = 15.8(8)\lambda$ ) than the beam waists ( $w_x = 1876\lambda$  and  $w_y = 2528\lambda$ ), similar to the observations for the matter wave.

This study opens up a new research field in our group and a paper on that measurements was prepared and submitted, and hopefully it will be published soon.

## 7.2 A glimpse into the future

The studies concerning the momentum distribution of the turbulent cloud, done in Chapter 5, concluded that, due to the coupling between our  $n'(k')$  analysis and the normal collective modes, it is necessary to develop a new method to measure the  $n'(k')$  or to create a new route to a quantum turbulent state, without excite this modes.

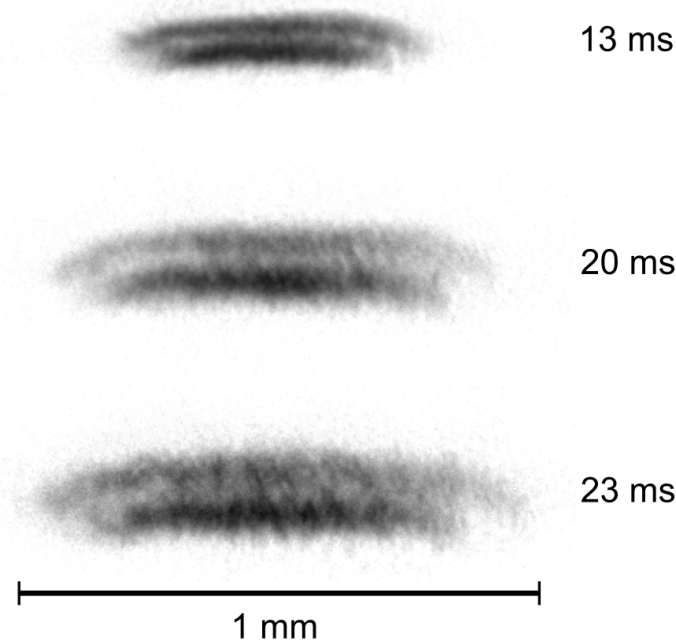


Figure 29 – TOF expansion of a BEC with a multicharged vortex ( $n = 4$ ) produced by topological phase-imprinting technique. The time-of-flight of each picture are shown in its right-side.

Source: By the author.

We choose to try another procedure to generate QT. In this way, a different method for vortex generation was necessary. We decided to implement a technique called *topological phase-imprinting* (148), which consist basically to imprint vortices in a BEC using topological phases by adiabatically inverting the magnetic bias field along the trap  $x$ -axis. This method allows to generate a multicharged vortex in the BEC (the charge depends on the hyperfine state of the atoms). In our case, the hyperfine state is the  $m_F = 2$  and a vortex with charge  $n = 4$  will be created using this method.

We have already implemented this method in our laboratory. Figure 29 shows some of the preliminary results of the vortex produced in the BEC by this method, where we can see the cloud falling in time-of-flight.

The energy of a  $n$ -charged vortex is higher than the energy of  $n$  unitary-charged vortex. (61,62,149) Thus, a multicharged vortex is not stable and it will decay in unitary vortices. The question is: How is this decay? We are studying this process, in collaboration with the group of Carlo F. Barenghi (Newcastle University), and an initial unpublished paper, about this working in progress, is available in (150) as an e-printed version.

The idea to study the giant vortices decay is that, following theoretical studies from our group (151, 152), it may be possible to generate, spontaneously, quantum turbulence through this decay. The *BEC-I* experimental team is now concentrating its efforts to investigate this new possibility in produce a turbulent atomic superfluid.

## 7.3 Prospects

In what follows, we listed general research prospects and some implementations to the *BEC-I* experimental system.

- One of the interesting topics of research is the condensate out-of-equilibrium. In this way, it is possible to study how the density-density correlation function is affected when the BEC is going from equilibrium to a perturbed state.
- Another study concerns the aspect ratio during expansion of the non-equilibrium BEC, to understand its behavior in the transition from a equilibrium BEC (coherent matter wave) to a turbulent cloud (matter wave speckle).
- One first experimental implementation is to picture the atomic cloud, simultaneously, in different (and orthogonal) image systems. This may allow to reconstruct the three-dimensional atomic distribution, which will be useful to better visualize and understand the matter wave speckle.
- Although those interests in the matter wave nature of QT, the dynamics properties of this regime remain an intriguing topic. A way to go further in this research is to study the decay of a multicharged vortex and map possible routes to quantum turbulence.
- Absorption images are destructive, this means that is only possible to probe the cloud once, and it does not seem to be a good technique to follow the cloud dynamics. Another experimental implementation is to setup a non-destructive image technique

(for example, the *phase-contrast* imaging). This method allows taking up to 20 images of the same BEC, which can be used to track the condensate (or the vortex) dynamics.

- Finally, the non-destructive technique also provides a possibility to study deeply the QT phenomenon. In particular the temperature dependence and the decay mechanisms, which are very important to conclusively demonstrate if the Kolmogorov spectrum is manifested in the turbulent atomic superfluids.

# References

- 1 EINSTEIN, A. Quantentheorie de einatomigen idealen Gases-Zweite. *Sitzungsberichte der Preussischen Akademie der Wissenschaften*, v. 1, p. 3–14, 1925.
- 2 BOSE, S. N. Plancks gesetz und lichtquantenhypothese. *Zeitschrift für Physik*, v. 26, n. 1, p. 178–181, 1924.
- 3 SALINAS, S. R. A. *Introdução à física estatística*. 2. ed. São Paulo: Editora da Universidade de São Paulo, 1997. 461 p.
- 4 ROMERO-ROCHÍN, V. Equation of state of an interacting Bose gas confined by a harmonic trap, the role of the harmonic pressure. *Physical Review Letters*, v. 94, n. 13, p. 130601, 2005.
- 5 HUANG, K. *Introduction to statistical physics*. 2nd ed. New York: Taylor & Francis, 2002. 290 p.
- 6 MEWES, M. O. et al. Output coupler for Bose-Einstein condensed atoms. *Physical Review Letters*, v. 78, n. 4, p. 582–585, 1997.
- 7 THOMAS, N. R. et al. Imaging of s and d partial-wave interference in quantum scattering of identical bosonic atoms. *Physical Review Letters*, v. 93, n. 17, p. 173201, 2004.
- 8 KAPUSTA, J. I. Bose-Einstein condensation, spontaneous symmetry breaking, and gauge theories. *Physical Review D*, v. 24, n. 2, p. 426, 1981.
- 9 MARQUES, G. C.; BAGNATO, V. S.; SPEHLER, D. Bose-Einstein condensation and spontaneous symmetry breakdown. *Laser Physics*, v. 14, n. 7, p. 1019–1030, 2004.
- 10 BLOCH, I. Ultracold quantum gases in optical lattices. *Nature Physics*, v. 1, n. 1, p. 23–30, 2005.
- 11 ROATI, G. et al. Anderson localization of a non-interacting Bose-Einstein condensate. *Nature*, v. 453, n. 7197, p. 895–898, 2008.
- 12 BLOCH, I.; DALIBARD, J.; ZWERGER, W. Many-body physics with ultracold gases. *Reviews of Modern Physics*, v. 80, n. 3, p. 885–964, 2008.

- 13 KAPITZA, P. Viscosity of liquid Helium below the  $\lambda$ -point. *Nature*, v. 141, n. 3558, p. 74, 1938.
- 14 ALLEN, J. F.; MISENER, A. D. Flow of liquid Helium II. *Nature*, v. 171, n. 3558, p. 75, 1938.
- 15 LONDON, F. The  $\lambda$ -phenomenon of liquid Helium and the Bose-Einstein degeneracy. *Nature*, v. 141, n. 3571, p. 643–644, 1938.
- 16 LANDAU, L. Theory of the superfluidity of Helium II. *Phys. Rev.*, v. 60, n. 4, p. 356–358, 1941.
- 17 ONSAGER, L. Statistical hydrodynamics. *Il Nuovo Cimento*, v. 6, n. 2, p. 279–287, 1949.
- 18 FEYNMAN, R. P. Application of quantum mechanics to liquid helium. *Progress in Low Temperature Physics*, v. 1, n. 1, p. 17–53, 1955.
- 19 HALL, H. E.; VINEN, W. F. The rotation of liquid helium II. I. experiments on the propagation of second sound in uniformly rotating helium II. *Proceedings of the Royal Society A: mathematical, physical and engineering sciences*, v. 238, n. 1213, p. 204–214, 1956.
- 20 CHU, S. Nobel lecture: the manipulation of neutral particles. *Reviews of Modern Physics*, v. 70, n. 3, p. 685–706, 1998.
- 21 COHEN-TANNOUDJI, C. N. Nobel lecture: manipulating atoms with photons. *Reviews of Modern Physics*, v. 70, n. 3, p. 707–719, 1998.
- 22 PHILLIPS, W. D. Nobel lecture: laser cooling and trapping of neutral atoms. *Reviews of Modern Physics*, v. 70, n. 3, p. 721–741, 1998.
- 23 KETTERLE, W.; DRUTEN, N. J. V. Evaporative cooling of trapped atoms. *Advances in Atomic, Molecular, and Optical Physics*, v. 37, p. 181–236, 1996.
- 24 ANDERSON, M. H. et al. Observation of Bose-Einstein condensation in a dilute atomic vapor. *Science*, v. 269, n. 5221, p. 198–201, 1995.
- 25 DAVIS, K. B. et al. Bose-Einstein condensation in a gas of sodium atoms. *Physical Review Letters*, v. 75, n. 22, p. 3969–3973, 1995.

- 26 BRADLEY, C. C. et al. Evidence of Bose-Einstein condensation in an atomic gas with attractive interactions. *Physical Review Letters*, v. 75, n. 9, p. 1687–1690, 1995.
- 27 JIN, D. S. et al. Collective excitations of a Bose-Einstein condensate in a dilute gas. *Physical Review Letters*, v. 77, n. 3, p. 420–423, 1996.
- 28 MARAGÒ, O. M. et al. Observation of the scissors mode and evidence for superfluidity of a trapped Bose-Einstein condensed gas. *Physical Review Letters*, v. 84, n. 10, p. 2056–2059, 2000.
- 29 TAVARES, P. E. S. et al. Out-of-phase oscillation between superfluid and thermal components for a trapped bose condensate under oscillatory excitation. *Laser Physics Letters*, v. 10, n. 4, p. 045501, 2013.
- 30 MATTHEWS, M. R. et al. Vortices in a Bose-Einstein condensate. *Physical Review Letters*, v. 83, n. 13, p. 2498–2501, 1999.
- 31 HENN, E. A. L. et al. Observation of vortex formation in an oscillating trapped Bose-Einstein condensate. *Physical Review A*, v. 79, n. 4, p. 043618, 2009.
- 32 SEMAN, J. A. et al. Three-vortex configurations in trapped Bose-Einstein condensates. *Physical Review A*, v. 82, n. 3, p. 033616, 2010.
- 33 HENN, E. A. L. et al. Emergence of turbulence in an oscillating Bose-Einstein condensate. *Physical Review Letters*, v. 103, n. 4, p. 045301, 2009.
- 34 HENN, E. A. L. et al. Generation of vortices and observation of quantum turbulence in an oscillating Bose-Einstein condensate. *Journal of Low Temperature Physics*, v. 158, n. 3-4, p. 435–442, 2010.
- 35 SEMAN, J. A. et al. Route to turbulence in a trapped Bose-Einstein condensate. *Laser Physics Letters*, v. 8, n. 9, p. 691, 2011.
- 36 SHIOZAKI, R. F. et al. Transition to quantum turbulence in finite-size superfluids. *Laser Physics Letters*, v. 8, n. 5, p. 393, 2011.
- 37 MAGALHÃES, K. M. F. *Obtenção da degenerescência quântica em sódio aprisionado*. 2004. 102 p. Tese (Doutorado) — Instituto de Física de São Carlos, Universidade de São Paulo, São Carlos, 2004.

- 38 HENN, E. A. L. *Produção experimental de excitações topológicas em um condensado de Bose-Einstein*. 2008. 126 p. Tese (Doutorado) — Instituto de Física de São Carlos, Universidade de São Paulo, São Carlos, 2008.
- 39 LEBEDEV, P. N. Untersuchungen über die druckkräfte des liches. *Annalen der Physik*, v. 311, n. 11, p. 433–458, 1901.
- 40 NICHOLS, E. F.; HULL, G. F. A preliminary communication on the pressure of heat and light radiation. *Physical Review*, v. 13, n. 5, p. 307–320, 1901.
- 41 NICHOLS, E. F.; HULL, G. F. The pressure due to radiation. *Physical Review*, v. 17, n. 1, p. 26–50, 1903.
- 42 FRISCH, R. Experimenteller nachweis des einsteinschen strahlungsrückstoßes. *Zeitschrift für Physik*, v. 86, n. 1, p. 42–48, 1933.
- 43 MAIMAN, T. H. Stimulated optical radiation in ruby. *Nature*, v. 187, n. 4736, p. 493–494, 1960.
- 44 ASHKIN, A. Atomic-beam deflection by resonance-radiation pressure. *Physical Review Letters*, v. 25, n. 19, p. 1321–1324, 1970.
- 45 HÄNSCH, T. W.; SHAHIN, I. S.; SCHAWLOW, A. L. High-resolution saturation spectroscopy of the sodium *d* lines with a pulsed tunable dye laser. *Physical Review Letters*, v. 27, n. 11, p. 707–710, 1971.
- 46 PICQUÉ, J. L.; VIALLE, J. L. Atomic-beam deflection and broadening by recoils due to photon absorption or emission. *Optics Communications*, v. 5, n. 5, p. 402–406, 1972.
- 47 SCHIEDER, R.; WALTHER, H.; WÖSTE, L. Atomic beam deflection by the light of a tunable dye laser. *Optics Communications*, v. 5, n. 5, p. 337–340, 1972.
- 48 HÄNSCH, T. W.; SCHAWLOW, A. L. Cooling of gases by laser radiation. *Optics Communications*, v. 13, n. 1, p. 68–69, 1975.
- 49 WINELAND, D. J.; DEHMELT, H. Proposed  $10^{14}\delta\nu < \nu$  laser fluorescence spectroscopy on  $\text{Ti}^+$  mono-ion oscillator III. *Bulletin of the American Physical Society*, v. 20, p. 637, 1975.

- 50 PHILLIPS, W. D.; METCALF, H. Laser deceleration of an atomic beam. *Physical Review Letters*, v. 48, n. 9, p. 596–599, 1982.
- 51 MIGDALL, A. L. et al. First observation of magnetically trapped neutral atoms. *Physical Review Letters*, v. 54, n. 24, p. 2596–2599, 1985.
- 52 RAAB, E. L. et al. Trapping of neutral Sodium atoms with radiation pressure. *Physical Review Letters*, v. 59, n. 23, p. 2631–2634, 1987.
- 53 MASUHARA, N. et al. Evaporative cooling of spin-polarized atomic hydrogen. *Physical Review Letters*, v. 61, n. 8, p. 935–938, 1988.
- 54 DEMARCO, B.; JIN, D. S. Onset of Fermi degeneracy in a trapped atomic gas. *Science*, v. 10, n. 5434, p. 1703–1706, 1999.
- 55 KLAERS, J. et al. Bose-Einstein condensation of photons in an optical microcavity. *Nature*, v. 468, n. 7323, p. 545–548, 2010.
- 56 GREINER, M.; REGAL, C. A.; JIN, D. S. Emergence of a molecular Bose-Einstein condensate from a Fermi gas. *Nature*, v. 426, n. 6966, p. 537–540, 2003.
- 57 THOMPSON, K. J. et al. Evidence of power law behavior in the momentum distribution of a turbulent trapped Bose-Einstein condensate. *Laser Physics Letters*, v. 11, n. 1, p. 015501, 2014.
- 58 BAGNATO, V. S.; PRITCHARD, D. E.; KLEPPNER, D. Bose-Einstein condensation in an external potential. *Physical Review A*, v. 35, n. 10, p. 4354–4358, 1987.
- 59 COURTEILLE, P. W.; BAGNATO, V. S.; YUKALOV, V. I. Bose-Einstein condensation of trapped atomic gases. *Laser Physics*, v. 11, n. 6, p. 659–800, 2001.
- 60 DALFOVO, F. et al. Theory of Bose-Einstein condensation in trapped gases. *Reviews of Modern Physics*, v. 71, n. 3, p. 463–512, 1999.
- 61 PETHICK, C. J.; SMITH, H. *Bose-Einstein condensation in dilute gases*. 2nd ed. Cambridge: Cambridge University Press, 2008. 569 p.
- 62 PITAEVSKII, L.; STRINGARI, S. *Bose-Einstein condensation*. New York: Oxford University Press, 2003. 382 p.

- 63 GROSS, E. P. Structure of a quantized vortex in boson systems. *Il Nuovo Cimento*, v. 81, n. 3, p. 454–477, 1961.
- 64 PITAEVSKII, L. P. Vortex lines in an imperfect Bose gas. *Soviet Physics Journal of Experimental and Theoretical Physics*, v. 13, n. 2, p. 451–454, 1961.
- 65 STRINGARI, S. Collective excitations of a trapped bose-condensed gas. *Physical Review Letters*, v. 77, n. 12, p. 2360–2363, 1996.
- 66 MEWES, M. O. et al. Collective excitations of a Bose-Einstein condensate in a magnetic trap. *Physical Review Letters*, v. 77, n. 6, p. 988–991, 1996.
- 67 RICHTER, J. P. *The notebooks of Leonardo da Vinci*. New York: Dover Publications, 1970. 514 p.
- 68 FRISCH, U. *Turbulence: the legacy of A. N. Kolmogorov*. Cambridge: Cambridge University Press, 1995.
- 69 DONNELLY, R. J.; SWANSON, C. E. Quantum turbulence. *Journal of Fluid Mechanics*, v. 173, p. 387–429, 1986.
- 70 TSATSOS, M. C. et al. Quantum turbulence in trapped atomic bose–einstein condensates. *Physics Reports*, v. 622, p. 1–52, 2016.
- 71 DAVIDSON, P. A. *Turbulence: an introduction for scientists and engineers*. Oxford: Oxford University Press, 2004.
- 72 REYNOLDS, O. An experimental investigation of the circumstances which determine whether the motion of water shall be direct or sinuous, and of the law of resistance in parallel channels. *Philosophical Transactions Royal Society of London*, v. 174, p. 935–982, 1883. Available from: <<http://www.jstor.org/stable/109431>>. Accessible at: 09 Feb. 2016.
- 73 ROTT, N. Note on the history of the Reynolds number. *Annual Review of Fluid Mechanics*, v. 22, n. 1, p. 1–12, 1990.
- 74 FALKOVICH, G. *Fluid mehanics*. Cambridge: Cambridge University Press, 2011.
- 75 RICHARDSON, L. F. *Weather Prediction by Numerical Process*. Cambridge: Cambridge University Press, 1922.

- 76 KOLMOGOROV, A. N. Dissipation of energy in the locally isotropic turbulence. *Doklady Akademii Nauk SSSR*, v. 32, p. 16–18, 1941. Available from: <<http://rspa.royalsocietypublishing.org/content/434/1890/15>>. Accessible at: 09 Feb. 2016.
- 77 KOLMOGOROV, A. N. The local structure of turbulence in incompressible viscous fluid for very large Reynolds numbers. *Doklady Akademii Nauk SSSR*, v. 30, p. 299–303, 1941. Available from: <<http://rspa.royalsocietypublishing.org/content/434/1890/9>>. Accessible at: 09 Feb. 2016.
- 78 SREENIVASAN, K. On the universality of the Kolmogorov constant. *Physics of Fluids*, v. 7, n. 11, p. 2778–2784, 1995.
- 79 SADDOUGH, S. Local isotropy in complex turbulent boundary layers at high Reynolds number. *Journal of Fluid Mechanics*, v. 348, p. 201–245, 1997.
- 80 BARENGHI, C.; DONNELLY, R.; VINEN, W. *Quantized vortex dynamics and superfluid turbulence*. New York: Springer Verlag, 2001. v. 571.
- 81 VINEN, W. F.; NIEMELA, J. J. Quantum turbulence. *Journal of Low Temperature Physics*, v. 128, n. 516, p. 167–231, 2002.
- 82 VINEN, W. F. Mutual friction in a heat current in liquid helium II. I. experiments on steady heat currents. *Proceedings of the Royal Society A: mathematical, physical and engineering sciences*, v. 240, n. 1220, p. 114–127, 1957.
- 83 VINEN, W. F. Mutual friction in a heat current in liquid helium II. II. experiments on transient effects. *Proceedings of the Royal Society A: mathematical, physical and engineering sciences*, v. 240, n. 1220, p. 128–143, 1957.
- 84 VINEN, W. F. Mutual friction in a heat current in liquid helium II. III. theory of the mutual friction. *Proceedings of the Royal Society A: mathematical, physical and engineering sciences*, v. 242, n. 1231, p. 493–515, 1957.
- 85 VINEN, W. F. Mutual friction in a heat current in liquid helium II. IV. critical heat currents in wide channels. *Proceedings of the Royal Society A: mathematical, physical and engineering sciences*, v. 243, n. 1234, p. 400–413, 1958.
- 86 MAURER, J.; TABELING, P. Local investigation of superfluid turbulence. *Europhysics Letters*, v. 43, n. 1, p. 29–34, 1998.

- 87 STALP, S. R.; SKRBEBEK, L.; DONNELLY, R. J. Decay of grid turbulence in a finite channel. *Physical Review Letters*, v. 82, n. 24, p. 4831–4834, 1999.
- 88 SVISTUNOV, B. V. Superfluid turbulence in the low-temperature limit. *Physical Review B*, v. 52, n. 5, p. 3647–3653, 1995.
- 89 KOBAYASHI, M.; TSUBOTA, M. Kolmogorov spectrum of quantum turbulence. *Journal of the Physical Society of Japan*, v. 74, n. 12, p. 3248–3258, 2005.
- 90 KOZIK, E. V.; SVISTUNOV, B. V. Kelvin-wave cascade and decay of superfluid turbulence. *Physical Review Letters*, v. 92, n. 3, p. 035301, 2004.
- 91 NAZARENKO, S. Differential approximation for Kelvin-wave turbulence. *Journal of Experimental and Theoretical Physics Letters*, v. 83, n. 5, p. 198–200, 2006.
- 92 KIVOTIDES, D. et al. Kelvin waves cascade in superfluid turbulence. *Phys. Rev. Lett.*, v. 86, n. 14, p. 3080, 2001.
- 93 TSUBOTA, M. Quantum turbulence – from superfluid helium to atomic Bose-Einstein condensates. *Journal of Physics: condensed matter*, v. 21, n. 16, p. 164207, 2009.
- 94 FONDA, E. et al. Direct observation of Kelvin waves excited by quantized vortex reconnection. *Proceedings of the National Academy of Sciences of the United State of America*, v. 111, p. 4707–4710, 2014.
- 95 KONDAUROVA, L. et al. Kelvin waves and the decay of quantum superfluid turbulence. *Physical Review B*, v. 90, n. 9, p. 094501, 2014.
- 96 SCHWARZ, K. W. Three-dimensional vortex dynamics in superfluid  $^4\text{He}$ : line-line and line-boundary interactions. *Phys. Rev. B*.
- 97 KOBAYASHI, M.; TSUBOTA, M. Quantum turbulence in a trapped Bose-Einstein condensate. *Physical Review A*, v. 76, n. 4, p. 1–4, 2007.
- 98 SHIOZAKI, R. F. *Quantum turbulence and thermodynamics on a trapped Bose-Einstein condensate*. 2013. 129 p. Tese (Doutorado) — Instituto de Física de São Carlos, Universidade de São Paulo, São Carlos, 2013.
- 99 TAVARES, P. E. S. *Consequências das excitações oscilatórias em condensados de Bose-Einstein*. 2012. 103 p. Dissertação (Mestrado) — Instituto de Física de São Carlos, Universidade de São Paulo, São Carlos, 2012.

- 100 BAGNATO, G. G. *Determinação da distribuição de momento em superfluidos atômicos aprisionados: regimes turbulento e não turbulento*. 2013. 113 p. Dissertação (Mestrado) — Instituto de Física de São Carlos, Universidade de São Paulo, São Carlos, 2013.
- 101 HENN, E. A. L. et al. Bose-Einstein condensation in  $^{87}\text{Rb}$ : characterization of the Brazilian experiment. *Brazilian Journal of Physics*, v. 38, n. 2, p. 279–286, 2008.
- 102 MYATT, C. J. et al. Multiply loaded magneto-optical trap. *Optics letters*, v. 21, n. 4, p. 290–292, 1996.
- 103 NELLESEN, J.; WERNER, J.; ERTMER, W. Magneto-optical compression of a monoenergetic sodium atomic beam. *Optics Communications*, v. 78, n. 3-4, p. 300–308, 1990.
- 104 WIEMAN, C. E.; FLOWERS, G.; GILBET, S. L. Inexpensive laser cooling and trapping experiment for undergraduate laboratories. *American Journal of Physics*, v. 63, n. 4, p. 317–330, 1995.
- 105 FORTAGH, J. et al. Fast loading of a magneto-optical trap from a pulsed thermal source. *Journal of Applied Physics*, v. 84, n. 12, p. 6499–6501, 1998.
- 106 RAPOL, U. D.; WASAN, A.; NATARAJAN, V. Loading of a Rb magneto-optic trap from a getter source. *Physical Review A*, v. 64, n. 2, p. 023402, 2001.
- 107 KLEMPT, C. et al. Ultraviolet light-induced atom desorption for large rubidium and potassium magneto-optical traps. *Physical Review A*, v. 73, n. 1, p. 013410, 2006.
- 108 PRITCHARD, D. E. et al. Light traps using spontaneous forces. *Physical Review Letters*, v. 57, n. 3, p. 310–313, 1986.
- 109 METCALF, H. J.; STRATEN, P. *Laser cooling and trapping*. New York: Springer-Verlag Inc., 1999. 323 p.
- 110 FOOT, C. J. *Atomic physics*. New York: Oxford University Press., 2005. 331 p.
- 111 KETTERLE, W.; DURFEE, D. S.; KURN, S. D. M. Making, probing and understanding Bose-Einstein condensates. In: INGUSCIO, M.; STRINGARI, S.; WIEMAN, C. E. (Ed.). *Bose-Einstein Condensation in Atomic Gases*. New York: IOS Press, 1999. (Proceedings of the International School of Physics “Enrico Fermi,” Course CXL).

- 112 BERGEMAN, T.; EREZ, G.; METCALF, H. J. Magnetostatic trapping field for neutral atoms. *Physical Review A*, v. 35, n. 4, p. 1535–1546, 1987.
- 113 MAJORANA, E. Atomi orientati in campo magnetico variabile. *Il Nuovo Cimento (1924-1942)*, v. 9, n. 2, p. 43–50, 1932.
- 114 PETRICH, W. et al. Stable, tightly confining magnetic trap for evaporative cooling of neutral atoms. *Physical Review Letters*, v. 74, n. 17, p. 3352–3355, 1995.
- 115 MEWES, M. O. et al. Bose-Einstein condensation in a tightly confining dc magnetic trap. *Physical Review Letters*, v. 77, n. 3, p. 416–419, 1996.
- 116 ESSLINGER, T.; BLOCH, I.; HÄNSCH, T. Bose-Einstein condensation in a quadrupole-Ioffe-configuration trap. *Physical Review A*, v. 58, n. 4, p. R2664–R2667, 1998.
- 117 SZCZEPKOWSKI, J. et al. Analysis and calibration of absorptive images of Bose-Einstein condensate at nonzero temperatures. *Review of Scientific Instruments*, v. 80, n. 5, p. 053103, 2009.
- 118 CASTIN, Y.; DUM, R. Bose-Einstein condensates in time dependent traps. *Physical Review Letters*, v. 77, n. 27, p. 5315–5319, 1996.
- 119 HENN, E. A. L. et al. Evaporation in atomic traps: a simple approach. *American Journal of Physics*, v. 75, n. 10, p. 907–910, 2007.
- 120 HESS, H. F. Evaporative cooling of magnetically trapped and compressed spin-polarized hydrogen. *Physical Review B*, v. 34, n. 5, p. 3476–3479, 1986.
- 121 DOYLE, J. M. et al. Hydrogen in the submillikelvin regime: sticking probability on superfluid  $^4\text{He}$ . *Physical Review Letters*, v. 67, n. 5, p. 603–606, 1991.
- 122 WALRAVEN, J. T. M. Atomic hydrogen in magnetostatic traps. In: OPPO, G. L. et al. (Ed.). *Quantum dynamics of simple system*. London: Institute of Physics Publ., 1996. (SUSSP proceeding, v. 44).
- 123 FRITSCH, A. R. et al. Nonlinear dependence observed in quadrupolar collective excitation of a trapped BEC. *Journal of Low Temperature Physics*, v. 180, n. 1, p. 144–152, 2015.

- 124 JIN, D. S. et al. Temperature-dependent damping and frequency shifts in collective excitations of a dilute Bose-Einstein condensate. *Physical Review Letters*, v. 78, n. 5, p. 764–767, 1997.
- 125 SEMAN, J. A. et al. Turbulence in a trapped Bose-Einstein condensate. *Journal of Physics: conference series*, v. 264, n. 1, p. 012004, 2011.
- 126 BAHRAMI, A. *Investigation of the momentum distribution of an excited Bose-Einstein condensate: coupling to the normal modes*. 2014. 80 p. Dissertação (Mestrado) — Instituto de Física de São Carlos, Universidade de São Paulo, São Carlos, 2014.
- 127 KOLMOGOROV, A. N. The local structure of turbulence in incompressible viscous fluid for very large Reynolds numbers. *Proceedings of the Royal Society of London A: mathematical, physical and engineering sciences*, v. 434, n. 1890, p. 9–13, 1991.
- 128 BLAŽKOVÁ, M. et al. Generation of turbulence by vibrating forks and other structures in superfluid  $^4\text{He}$ . *Physical Review B*, v. 79, n. 5, p. 054522, 2009.
- 129 CARACANHAS, M. A. *Vortices and impurities in atomic superfluids: self-similar expansion and Tkachenko polaron*. 2014. 121 p. Tese (Doutorado) — Instituto de Física de São Carlos, Universidade de São Paulo, São Carlos, 2014.
- 130 BAHRAMI, A. et al. Investigation of the momentum distribution of an excited BEC by free expansion: coupling with collective modes. *Journal of Low Temperature Physics*, v. 180, n. 1, p. 126–132, 2015.
- 131 LEGGETT, A. J. Bose-Einstein condensation in the alkali gases: some fundamental concepts. *Reviews of Modern Physics*, v. 73, n. 2, p. 307–356, 2001.
- 132 BLOCH, I.; DALIBARD, J.; NASCIMBÈNE, S. Quantum simulations with ultracold quantum gases. *Nature Physics*, v. 8, n. 4, p. 267–276, 2012.
- 133 IMPENS, F.; BORDÉ, C. J. Generalized *ABCD* propagation for interacting atomic clouds. *Physical Review A*, v. 79, n. 4, p. 043613, 2009.
- 134 RIOU, J. F. et al. Theoretical tools for atom-laser-beam propagation. *Physical Review A*, v. 77, n. 3, p. 033630, 2008.
- 135 RIOU, J. F. et al. Beam quality of a nonideal atom laser. *Physical Review Letters*, v. 96, n. 7, p. 070404, 2006.

- 136 COUVERT, A. et al. A quasi-monomode guided atom laser from an all-optical Bose-Einstein condensate. *Europhysics Letters*, v. 83, n. 5, p. 50001, 2008.
- 137 BILLY, J. et al. Direct observation of Anderson localization of matter waves in a controlled disorder. *Nature*, v. 453, n. 7197, p. 891–894, 2008.
- 138 DONNELLY, R. J. *Quantized Vortices in helium II*. (Cambridge studies in low temperature physics). Cambridge: Cambridge University Press, 1991.
- 139 CARACANHAS, M. et al. Self-similar expansion of the density profile in a turbulent Bose-Einstein condensate. *Journal of Low Temperature Physics*, v. 166, n. 1, p. 49–58, 2012.
- 140 SIEGMAN, A. E. *Lasers*. California: University Science Books, 1986. 1283 p.
- 141 GOODMAN, J. W. *Speckle phenomena in optics: theory and applications*. Colorado: Roberts and Company Publishers, 2010. 387 p.
- 142 CARTER, W. H. Electromagnetic field of a gaussian beam with an elliptical cross section. *Journal of the Optical Society of America*, v. 62, n. 10, p. 1195–1201, 1972.
- 143 NAZARENKO, S. *Wave turbulence*. Heidelberg: Springer-Verlag Berlin Heidelberg, 2011. v. 825. 279 p. (Lecture notes in physics, v. 825).
- 144 CARACANHAS, M. et al. Self-similar expansion of a turbulent Bose-Einstein condensate: A generalized hydrodynamic model. *Journal of Low Temperature Physics*, v. 170, n. 3, p. 133–142, 2013.
- 145 DALL, R. G. et al. Observation of atomic speckle and Hanbury Brown-Twiss correlations in guided matter waves. *Nature Communications*, v. 2, n. 291, p. 1–5, 2011.
- 146 HARUTINIAN, J. A. S. *Study of excitations in a Bose-Einstein condensate*. 2011. 189 p. Tese (Doutorado) — Instituto de Física de São Carlos, Universidade de São Paulo, São Carlos, 2011.
- 147 CUEVAS, F. J. P. *Aspects of hybrid confinement for a Bose-Einstein condensate: global pressure and compressibility*. 2014. 115 p. Tese (Doutorado) — Instituto de Física de São Carlos, Universidade de São Paulo, São Carlos, 2014.
- 148 LEANHARDT, A. E. et al. Imprinting vortices in a Bose-Einstein condensate using topological phases. *Physical Review Letters*, v. 89, n. 19, p. 190403, 2002.

- 
- 149 MÖTTÖNEN, M. et al. Splitting of a doubly quantized vortex through intertwining in Bose-Einstein condensates. *Physical Review A*, v. 68, n. 2, p. 023611, 2003.
- 150 ALLEN, A. J. et al. Twisted unwinding of multi-charged quantum vortex and generation of turbulence in atomic Bose-Einstein condensates. 2015. Available from: <<http://arxiv.org/abs/1505.00616>>. Accessible at: 09 Mar. 2016.
- 151 SANTOS, A. C.; BAGNATO, V. S.; SANTOS, F. E. A. Spontaneous generation of quantum turbulence through the decay of a giant vortex in a two-dimensional superfluid. 2014. Available from: <<http://arxiv.org/abs/1405.0992>>. Accessible at: 09 Mar. 2016.
- 152 CIDRIM, A. et al. Controlled polarization of two-dimensional quantum turbulence in atomic Bose-Einstein condensates. 2015. Available from: <<http://arxiv.org/abs/1507.03135>>. Accessible at: 09 Mar. 2016.



# APPENDIX



# APPENDIX A – Calculating

$$g^{(2)}(\Delta r)$$

Here we will describe the main ideas of the process to compute the second-order correlation function,  $g^{(2)}$ . For an atomic density distribution,  $g^{(2)}$  is also called density-density correlation function and is defined by Equation 6.1. We compute this quantity from an absorption image of the atomic cloud that, as we discussed in Section 3.6, gives the information of the atomic density distribution,  $n(r)$ .

The atomic cloud picture is a built of discrete pixel and each pixel has the information of the cloud optical density,  $OD(x, y)$ . Figure (30) illustrates the atomic density distribution and two  $OD(x, y)$  pixels that are used to calculate the  $g^{(2)}$  function. The pixel  $A$  is at the position  $(i, j)$  and the pixel  $B$  is at  $(i + \Delta i, j + \Delta j)$ . With this figure in mind, we can write the  $g^{(2)}$  function as:

$$g^{(2)}(\Delta ij) = \frac{\langle OD(i, j) OD(i + \Delta i, j + \Delta j) \rangle_{\Delta ij}}{\langle OD(i, j) \rangle_{\Delta ij} \langle OD(i + \Delta i, j + \Delta j) \rangle_{\Delta ij}} \quad (\text{A.1})$$

where  $\Delta ij = \sqrt{\Delta i^2 + \Delta j^2}$  is the distance between the points  $A$  and  $B$ , and  $\langle X \rangle_{\Delta ij}$  is the mean value of  $X$  that has the same value of  $\Delta ij$  (i.e. for a fixed distance, we sum the values of  $X$  and divided by the number of occurrences).

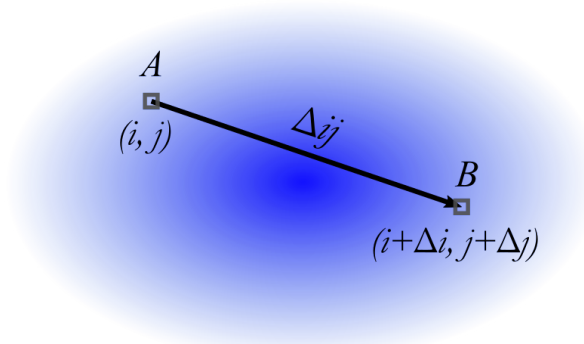


Figure 30 – Illustrative drawing on the density-density correlation function calculation.  $A$  and  $B$  are two pixels of the cloud optical density (blue), at a position  $(i, j)$  and  $(i + \Delta i, j + \Delta j)$ , respectively.

Source: By the author.

Thus, the main steps to calculate  $g^{(2)}$  evaluation are: For a fixed distance, we calculate the quantities inside the mean operator between all two-pixel pairs of the cloud. Then, we compute the mean values and obtain the  $g^{(2)}$  correlation value for that distance. We repeat this procedure for all available pixel-pixel distances in the cloud. And, finally it results in the  $g^{(2)}$  values as a function of the density-density distance (i.e. the second-order correlation function for the atomic density distribution).

We have to point out that: the bulk density for the atomic distribution is not uniform (in our case can be a Gaussian profile or a Thomas-Fermi profile, depending on the sample that we are investigating, see Section 3.6). Thus, we have to take care that this density variation is not taken into account in  $g^{(2)}$  function. In this way, we perform the method described above in small regions (that we call *zones*, which typically we used  $25 \times 25$  pixels) inside the cloud. After having the  $g^{(2)}$  for all this zones, we calculate the correlation function of the full cloud by doing a mean of this  $g^{(2)}$  functions.

Another important remark is: it is necessary to avoid points where the density has deep variations when compared one to each other. This deep variations typically come from image noise or detection noise, and they are not related to density fluctuations. In such a way, we define a threshold density fluctuation values for the cloud, which gives the lowest value of density that are related to density fluctuation. Value of density lower than the threshold are discarded during the  $g^2$  calculation, because they come from that noise. We call this threshold value as *odthresh* and typically is 5% of the OD depth.

To perform the numerical calculation of the  $g^{(2)}$ , Equation (A.1), we developed a MATLAB script. In what follows, we are providing this script.

```

1  %%% Script to calculate the density-density correlation function
2  %%%
3  %%% CREATED BY PEDRO TAVARES — LAST VERSION: 04/11/2015
4  %%%
5  %%%
6
7  clear;
8  % opening the picture
9  [fname,pathfile] = uigetfile({'*.tif;*.tiff;*.png;', 'All Image Files'...
    ; '.*', 'All Files'});
10 path = strcat(pathfile, fname);
11

```

```

12 tic,
13
14 % Constants
15 h=6.626e-34;           % Planck constant [J.s]
16 mRb = 1.44316e-25;    % 87Rb mass [kg]
17 kB = 1.38065e-23;    % Boltzmann cte [J/K]
18 sigma = 2.9064*10^(-13); % Scattering cross section for 87Rb [mm^2]
19 fr = 186.3; wr = 2*pi*fr;% radial trap frequency [Hz] and [rad/s]
20
21 % Image parameters
22 fcal = 2.499;         % calibration [um/pixel]
23 tof = 25e-3;         % time-of-flight [s]
24 tol=5e-6;           % tolerance
25
26
27 % Taking some useful characteristics of the cloud
28 I = imread(path);
29 I = I(:, :, 1);
30 msz = min(size(I));
31
32 figure(1)
33 I = imcrop(I); pk = max( max(I) );
34 close figure 1
35
36 I1 = pk - I; I1 = imclearborder( I1 ); level = graythresh(I1);
37 level=0.30;
38 bI1 = bwareaopen( im2bw( I1, level ), 50 );
39 s = regionprops(bI1, I1, 'Orientation','WeightedCentroid','Centroid',...
40     ...
41     'MajorAxisLength','MinorAxisLength');
42 % cloud center-of-mass and radius
43 cm = s.WeightedCentroid;
44 xcm = round(cm(1));
45 ycm = round(cm(2));
46 sz(1) = round(s.MajorAxisLength);
47 sz(2) = round(s.MinorAxisLength);
48 rd = sz./2;
49 cloudsizex = sz(1);
50 cloudsizex = sz(2);
51 od = -log( double(I)/double(pk) ); % Optical density
52
53 %%%%%%%%%%%%%%%%%%%%%%%%%%%%%%%%%%%%%%%%%%%%%%%%%%%%%%%%%%%%%%%%%%%%%%%%%
54 %% STARTING THE CODE FOR EVALUATE THE %%
55 %% DENSITY-DENSITY CORRELATION FUNCTION %%
56 %%%%%%%%%%%%%%%%%%%%%%%%%%%%%%%%%%%%%%%%%%%%%%%%%%%%%%%%%%%%%%%%%%%%%%%%%
57 Nzone = 25; % #Pixel in each zone
58 varisizex = Nzone; % length in x and y of each ZONE
59 varisizey = Nzone;
60 numberofcropx = round(cloudsizex/varisizex); % number of zones
61 numberofcropsy = round(cloudsizey/varisizey);
62
63 % evaluate all possible r in the zone
64 ri=zeros((Nzone+1)^2,1); % to prelocate ri values.
65 k=0;
66 for i=0:Nzone
67     for j=0:Nzone
68         k=k+1;

```

```

69         ri(k,1)=sqrt(i^2+j^2);
70     end
71 end
72 ri=unique(ri); % arrange the vector dr in crescent way and without ...
    repetitions
73 sizeri=size(ri); % this gives the numbem of differents dr that nn was...
    evaluated
74
75 odmin = min(min(od));
76 odmax = max(max(od));
77 odthresh = 0.05*(odmax-odmin); %To avoid points where the density ...
    have deep variations compared to each other
78
79 max_crop_region = numberofcropsx*numberofcropsy;
80 gn = zeros(sizeri(1),max_crop_region);
81 r = zeros(sizeri(1),max_crop_region);
82 crop_region = 0; % region counter
83 for cy = 1:1:numberofcropsy;
84     for cx = 1:1:numberofcropsx;
85         xcrop = (xcm - round(cloudsizex/2) - varisizex ) + cx*varisizex; ...
            %started 'position x' for each zone
86         ycrop = (ycm - round(cloudsizey/2) - varisizey ) + cy*varisizey; ...
            %started 'position y' for each zone
87
88         %%%%%%%%% Evaluating the g2 for each region %%%
89         %% nn -> is the product of OD(r) and OD(r+dr)
90         %% dr -> is the dr between the 2 points r and r+dr
91         %% odij -> is the OD(r) used for evaluate nn
92         %% odmn -> is the OD(r+dr) used for evaluate nn
93 nn = zeros((varisizex+1)^2 * (varisizey+1)^2, 1);% defined for ...
    preallocating array (this makes the code faster)
94 dr = zeros((varisizex+1)^2 * (varisizey+1)^2, 1);
95 odij = zeros((varisizex+1)^2 * (varisizey+1)^2, 1);
96 odmn = zeros((varisizex+1)^2 * (varisizey+1)^2, 1);
97 kp=0; % counter of the #of products, used for vector index.
98
99 for i=(ycrop):(ycrop + varisizey)
100     for j=(xcrop):(xcrop + varisizex)
101         for m=(i):(ycrop + varisizey)
102             for n=(j):(xcrop + varisizex)
103                 if( (od(i,j)>odthresh) && (od(m,n)>odthresh) )
104                     kp = kp+1;
105                     dr(kp,1) = sqrt((i-m)^2+(j-n)^2);
106                     nn(kp,1) = (od(i,j)*od(m,n));
107                     odij(kp,1) = od(i,j);
108                     odmn(kp,1) = od(m,n);
109                 end
110             end
111         end
112     end
113 end
114 crop_region = crop_region + 1;
115
116 for k=1:sizeri(1)
117     index=find(dr==ri(k) & odij>odthresh & odmn>odthresh & nn>0);
118     n1=numel(index);
119     if( n1>0 )
120         odijmean= sum(odij(index,1))./n1;

```

```

121     odmnmean= sum(odmn(index,1))./n1;
122     nnmean = sum(nn(index,1))./n1;
123     gn(k,crop_region)= nnmean./(odijmean.*odmnmean);%this preallocate ...
           the 'g2 function for each ZONE' in a function of dr.
124     r(k,crop_region)=ri(k);
125     end
126 end
127
128 %%%%%%%%% drawing the region of the crop %%%%%%%%%
129 figure(2);
130 imagesc(od);
131 axis equal tight;
132 rectangle('position',[(xcm - round(cloudsizex/2)) (ycm - round(...
           cloudsizex/2)) numberofcropsx*varisizex numberofcropsy*varisizey],...
           'EdgeColor','black','LineWidth',2,'LineStyle','-');
133 rectangle('position',[xcrop ycrop varisizex varisizey],'EdgeColor','...
           red','LineWidth',2,'LineStyle','-');
134 f=getframe(gca);
135 [X, map] = frame2im(f);
136
137     end
138 end
139
140 % Mean of gn for only gn>0.
141 index2 = (gn>0);
142 n2=sum(index2,2); %this gives the numer of elements with same ...
           distance
143 gnaux = gn.*index2;
144 g = sum(gnaux,2)./n2;
145
146 %%%%%%%%%%%
147 %%%%%%%%%%% PLOTTING THE RESULTS %%%%%%%%%%%
148 figure(4)
149 hold on
150 graph = plot(ri,g')
151 set(graph,'LineWidth',1.5);
152 title('Second-order correlation function','FontSize',13);
153 set(gca,'FontSize',12,'LineWidth',1.5);
154 xlabel('\fontsize{13}\it distance');ylabel('\fontsize{13}\it g_2');
155
156 %% SAVE FILES
157 fprintf('\n\t SAVING RESULTS IN .dat FILES...\n')
158 parameter = input('Parameter: ');
159 % saving the results in a .dat
160 aux = [ri g];
161 fname = strcat(strcat(fname,strcat('Nzone',num2str(parameter))), 'px'...
           );
162 caminho = strcat(fname, '.dat');
163 [n_linhas n_colunas] = size(aux);
164 fid = fopen (caminho,'wt');
165 for i=1:n_linhas
166     for j=1:n_colunas
167         fprintf(fid,'%f ',aux(i,j));
168     end
169     fprintf(fid,'\n');
170 end
171 fclose (fid);

```



# APPENDIX B – Effects of a projection onto correlation length

In Section 6.3 we argue that the measurement of the correlation length is not affected by the projection (as the case of an absorption image, that is a 2D-projection of a 3D density distribution). In this appendix, we compare the second-order correlation function of a 2D optical speckle and its projection in one dimension, to support our claim.

The speckle beam is simulated in the same way as done in Chapter 6. Figure 31(a) presents the simulated speckle beam cross-section and Figure 31(b) shows the projection profile of this speckle beam in one dimension. We can see that in the speckle beam the fluctuations are deeper than in the projection profile. Thus, the fluctuations amplitude are smoothed in the beam projection.

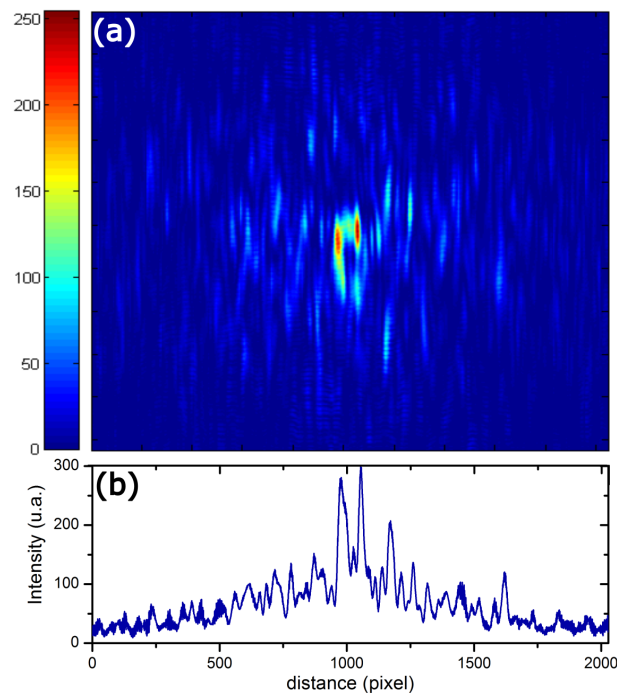


Figure 31 – Comparison between a 2D speckle beam and its projection in one dimension. (a) Simulated speckle beam cross-section profile. (b) 1D projection profile of the speckle beam

Source: By the author.

We calculated the second-order correlation function for these two cases, following a similar procedure as described in Appendix A. The resulting curves are presented in Figure 32. It is notable that the amplitude of the correlation function is reduced,  $g_{1D}^{(2)}(0) < g_{2D}^{(2)}(0)$ . However, the correlation length extracted from both  $g^{(2)}$  are the same. For the 2D case we obtain a correlation length equal to  $\ell_{2D} = 15.8(8)\lambda$ , and  $\ell_{1D} = 18(3)\lambda$  for the 1D case.

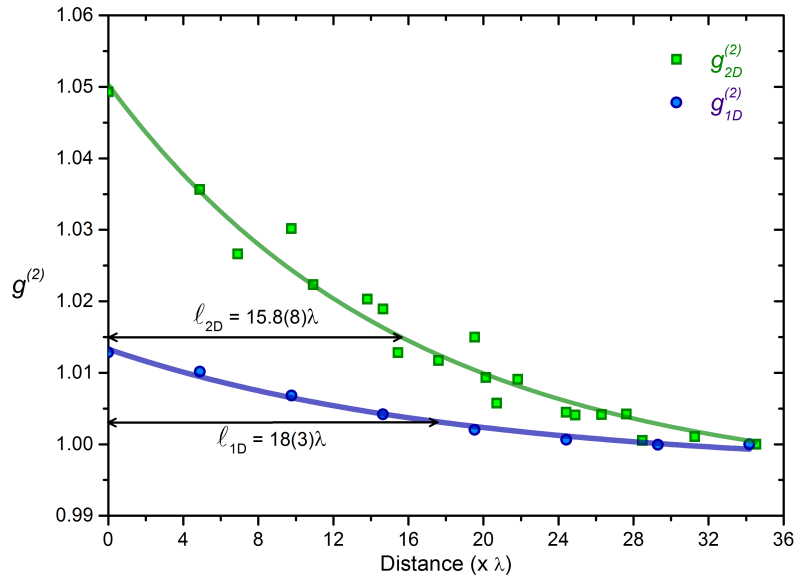


Figure 32 – Comparison between  $g_{2D}^{(2)}(\Delta r)$  and  $g_{1D}^{(2)}(\Delta r)$ . Second-order correlation function for a 2D speckle beam,  $g_{2D}^{(2)}(\Delta r)$  (green squares), and for its projection in one dimension,  $g_{1D}^{(2)}(\Delta r)$  (blue circles).

Source: By the author.

Therefore, we conclude that despite the fact of the fluctuations amplitude of the projected speckle are smaller than the amplitude of the initial speckle, the correlation length measured remains unaffected.